Development of a Gamma-Ray Beam Profile Monitor for the High-Intensity Gamma-Ray Source

A Thesis Submitted to the College of
Graduate Studies and Research
in the Partial Fulfillment of the Requirements
for the Degree of Master of Science
in the
Department of Physics and Engineering Physics
University of Saskatchewan
Saskatoon

by
Thomas Z. Regier

Saskatoon, Saskatchewan
Canada

Abstract

Beam profile monitors provide position and flux distribution information to facilitate the configuration of an experimental apparatus and are an important component of any accelerator facilities beam diagnostic system. Nuclear physics experiments typically involve the incidence of high energy particles or gamma-rays on some target material and the detection of the products of the ensuing interactions. Therefore, knowing the profile of the incident radiation beam is desirable. To address the need for a profile monitor for the High-Intensity Gamma-Ray Source, development of a CCD-based gamma-ray beam profiler was undertaken.

The profiler consisted of plastic scintillator, a lens system and a Starlight Express MX5 CCD camera, all contained within a light tight box. The scintillation pattern, created by the interaction between the incident gamma-rays and the scintillator, could be focused onto the CCD. Simulations were used to determine the amount of power that would be absorbed for different beam energies and scintillator thicknesses. The use of a converter material, placed directly against the scintillator to improve power deposition, was also investigated.

The system was tested in order to find the camera noise characteristics, the optical resolution and magnification and the systems responsivity to power absorption in the scintillator. Using a ^{137}Cs source, preliminary beam profiles were obtained. By combining the results of the testing and simulation, predictions of the required length of exposure were made. It was determined that a beam with a flux of $10^6\gamma$/s and a diameter of 2.5 cm could be profiled, using 6.0 mm of plastic scintillator and 0.6 mm of iron converter, to within 5% error per 0.64 mm x 0.91 mm resolving unit, in less than 1 minute.

Acknowledgements

I greatly appreciated the guidance of my co-supervisors, Dr. Norm Kolb and Dr. Ru Igarashi. They were always willing to share their experience and expertise and, perhaps most importantly, time. I am also greatful for the encouragement they have given me.

I am most greatful to the Natural Sciences and Engineering Research Council (NSERC) for supplying much of the funding for this project.

I would like to thank Dr. Henry Caplan for his helpful suggestions. This project would have turned out much differently if it weren't for his keen insight.

I received a great deal of support from all of the staff at the University of Sasakatchewan. I would like to specifically thank Angelika Ortlepp, Stan Shadick, Brian Zulkoskey, Blair Chomyshen and Perry Balon for their assistance.

A big thanks goes out to all of the graduate students who have shared an office with me. Thanks for the assistance, good conversations and for putting up with me.

I would like to extend a special thanks to my family and friends who have always supported my education, no matter how long I wanted to stay in school. Thanks, Mom and Dad!

Finally, I would like to thank my wonderful wife, Andrea. Thanks for always believing in me.

Contents

List of Figures

List of Tables

List of Abbreviations

ADC	Analogue-to-Digital Converter
BGO	Bismuth Germanate
CCD	Charge Coupled Device
CERN	Center for Experimental Nuclear Physics Research
CFITSIO	C Flexible Image Transport System Input and Output
DFELL	Duke Free Electron Laser Laboratory
EPD	Entrance Pupil Diameter
FITS	Flexible Image Transport System
FPN	Fixed Pattern Noise
GCCD	Gnome Charge Coupled Device
HIGS	High-Intensity Gamma-Ray Source
LED	Light Emitting Diode
LSB	Least Significant Bit
MCP	Multi-Channel Plate
MOS	Metal Oxide Semiconductor
NaI	Sodium Iodide Detector
NASA	National Aeronautics and Space Administration
NIM	Nuclear Instrumentation Module
PC	Personal Computer
PCI	Peripheral Component Interconnect
PMT	Photo-Multiplier Tube
PRNU	Photo-Response Non-Uniformity
TOF	Time of Flight
TUNL	Triangle Universities Nuclear Laboratory
UV	Ultraviolet

1 Introduction

1.1 Gamma-Ray Beam Profiling

Beam profile monitors are an important component in any nuclear physics experimental facility's beam diagnostic system. They provide a means by which the position and flux distribution of a beam can be measured to allow for the proper alignment of the target and detector system. Beam profiles, measured periodically during an experiment, can detect any changes in the flux distribution and position that could affect the experiment. They also provide feedback to the beam operators to aid in the setup of the beam. Indeed, the extra level of diagnostic information afforded by a profile monitor makes them a key part of any beam diagnostic system.

For a profile monitor to be effective it needs to satisfy certain requirements. A sub-millimeter resolution is needed to ensure the proper level of precision in the beam position measurement and to identify small regions of flux discontinuity. To identify changes in the beam profile with respect to time, the monitor has to be able to produce results in an acceptable time period. Also, for the monitor to be used during an experimental run, it has to be non-destructive to the beam. This implies that it has to be placed in the beam permanently without causing significant flux degradation. A device that can fulfill these demands will be a truly beneficial diagnostic component.

There are several different methods that can be employed for the profiling of a beam. The design depends on the type of radiation of interest (i.e. electrons, heavy ions, gamma-rays) the relevant energy range and the beam flux. Charged particle beams can be profiled destructively using a phosphorescent screen and a video camera or a wire chamber. A non-destructive method that makes use of transition radiation is described in Ref. [Wis01]. Gamma-ray beam profile monitoring has traditionally been performed using wire chambers or multi-wire proportional counters [Ahm02] and X-ray film. However, the literature describing the profiling of gamma-ray beams, in particular non-destructive profiling, is sparse.

1.2 The High Intensity Gamma-Ray Source (HIGS)

In the 1990's, collaboration between the Duke Free Electron Laser Laboratory (DFELL) and the Triangle Universities Nuclear Laboratory (TUNL) resulted in the creation of the High-Intensity Gamma-Ray Source (HIGS). At the HIGS facility, highly polarized and monochromatic gamma-rays are produced for research related to photonuclear interactions [Car94].

A 280 MeV linear accelerator is used to inject two electron bunches into a storage ring where they can be accelerated up to 1.1 GeV (see Fig.1). The first electron bunch passes through a set of wigglers which create laser light in the visible to ultraviolet (UV) range. This light travels to the end of the optical cavity and is reflected back toward the second electron bunch. Compton scattering, a photon interaction that will be discussed in Sec. 2.1.2, of the UV laser light off the second electron bunch creates gamma-rays with tunable energies

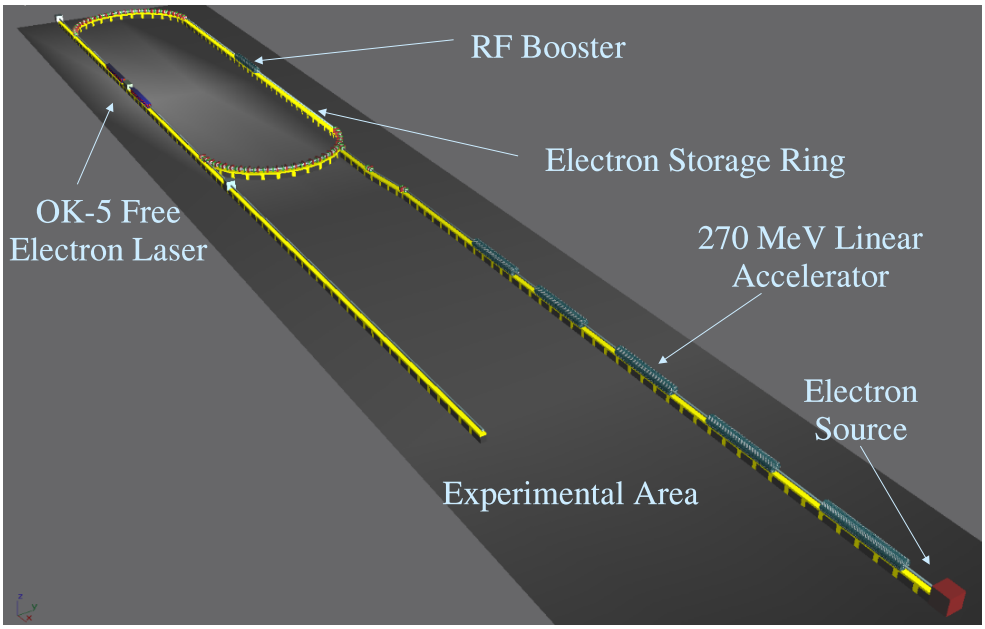

Figure 1: Layout of the HIGS facility.

between 2 and 225 MeV over a potential flux range of 10^5 to 10^{10} γ/s.[1] These gamma-rays exit the optical cavity and travel to the experimental vault where they are used.

The gamma-ray beam diagnostic equipment currently used at HIGS is made up of four components: a paddle counter, an on-axis sodium iodide (NaI), an off-axis NaI and X-ray film. The paddle counter measures electron production rates along the beam axis and is used as a calibrated flux monitor. The on-axis NaI can be used to measure flux directly when the beam flux is low, and measures transmission rates through an absorber for higher gamma-ray fluxes. The off-axis NaI is used to measure Compton scattering rates which can be used to calculate beam flux. X-ray film, placed in the beam, provides a means of determining the beam position. The configuration of these devices is shown in Fig. 2.

Beam profiles are currently produced by exposing X-ray film to the gamma-ray beam. The intensity of gamma-rays as a function of position is recorded on the film. The problem with this technique is that it involves entering the experimental vault to place and retrieve the film which causes delays related to starting and stopping gamma-ray production. More lengthly delays are introduced because the film has to be transported to a local hospital to be developed. Another problem is that the relationship between the exposure length and the gamma-ray intensity is not linear. In other words, the relative brightness of the beam

[1]The values for the gamma-ray energy and flux ranges given are values expected following a scheduled upgrade.

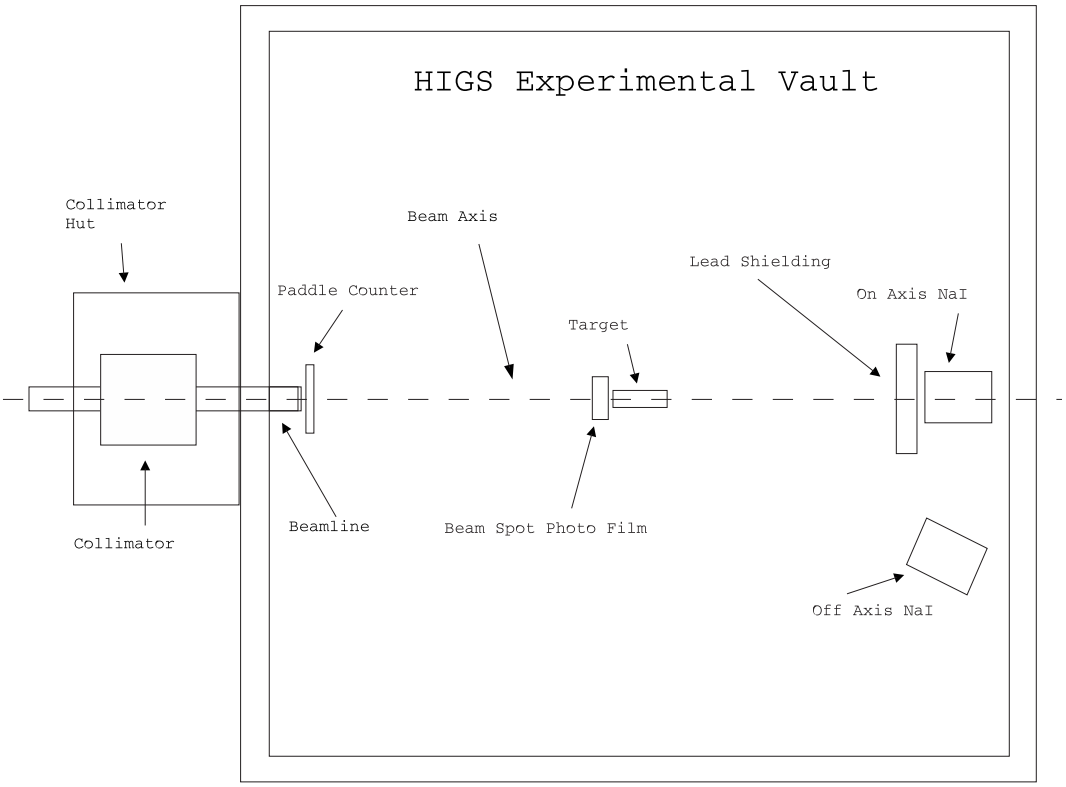

Figure 2: Beam diagnostic hardware presently used in the HIGS experimental vault (not to scale).

spot photo cannot be used to indicate the gamma-ray intensity.

1.3 Motivation

Future experiments performed at HIGS would benefit from the added beam diagnostic information afforded by a beam profile monitor. This monitor should be able to provide high position and flux resolution without being difficult or time consuming to operate. For maximum benefit the monitor should be non-destructive, permitting operation and experimentation simultaneously.

To achieve a good level of precision in the beam position measurement a resolution of less than a millimeter is required. This will ensure that the collimators and detector systems can be positioned accurately with respect to the beam axis. To be able to discern spatial changes in the flux distribution, the monitor needs to provide a measurement with, at most, 5% error in each resolving element. This will permit the observation of specific regions of different flux within the beam spot.

One key design requirement for the monitor is that it should be easy to use. This implies that the acquisition of a profile doesn't require any preparation time or human involvement.

Thus, the required data acquisition and control systems should be automated and easily interfaced with the existing systems.

The monitor should be able to produce beam profiles across the entire operational energy and flux ranges of HIGS. Currently, HIGS is capable of producing a gamma-ray flux of between 10^5 to 10^7 γ/s at energies between 2 and $\sim$30 MeV. However, the projected flux and energy ranges, following upgrades and fine tuning, are 10^5 to 10^{10} γ/s at energies between 2 and 225 MeV, so these values should be used to define the operational range of the profiler.

The following thesis documents the design, development, construction and preliminary testing of a gamma-ray beam profile for use at HIGS. Attention will be paid to the fundamental theories involved in gamma-ray detection and the theories behind scintillation, the charge coupled device and optical design. The development of two types of monitor, the scanning profiler and the CCD profiler, will be discussed, with the latter receiving the bulk of the attention. Source testing of each component in the CCD based profiler and the results of this testing will be documented.

2 Theoretical Background

2.1 The Interaction of Photons

The three processes through which photons interact with materials are the photoelectric effect, Compton scattering and pair production. Other processes, like nuclear dissociation reactions, are possible but not very common for the gamma-ray energies that are expected at HIGS. Each of the three processes occur through separate mechanisms, at different rates depending on energy, and result in varying amounts of energy being transferred to the electrons in the medium. The theory behind the three main photon interactions as well as the theory on the subsequent electron interactions is provided to generate a clear picture of how photons can be detected. A discussion of the theory as it relates to particle interaction simulation will also be included to give credence to the simulation results used in this project.

2.1.1 The Photoelectric Effect

The photoelectric effect involves the absorption of a photon by an atomic electron and the subsequent ejection of the electron from the atom:

$$\gamma + atom \rightarrow atom^{+} + e^{-}. \tag{1}$$

A calculation of the photoelectric cross section using a Born approximation results in

$$\sigma_{photo} = 4\alpha^4\sqrt{2}Z^5\phi_0(\frac{m_e c^2}{h\nu})^{\frac{7}{2}}, \tag{2}$$

where $\alpha = \frac{1}{137}$ is the fine structure constant, $\phi_0 = 8\pi r_e^2/3 = 6.651\times10^{-25}cm^2$, $m_e = 0.511\frac{MeV}{c^2}$ is the electron mass, $h\nu$ is the incident photon energy, Z is the atomic number of the medium, $r_e = 2.818 \times 10^{15}m$ is the classical electron radius and c is the speed of light [Leo94]. Note the fifth order dependence on the atomic number of the interaction medium and the $-\frac{7}{2}$ order dependence on the incident photon energy. A plot of the photoelectric cross section as calculated by Eq. 2 is shown in Fig. 3.

Distinctive edges appear in the cross section where the binding energy of the atomic electron is near the photon energy (see Fig. 3). The cross section suddenly changes at these photon energies because the atomic electrons in the respective shell are no longer available for interactions with photons at lower energies.

A photon that interacts with a medium via the photoelectric effect is absorbed. Therefore there will be a total transfer of the photon's energy to the electron. This is a beneficial property for the purposes of detection and measurement. However, the cross section for this process drops off quickly with increasing photon energy and is especially low for a medium with a small atomic number.

2.1.2 Compton Scattering

Compton scattering is the process in which photons are scattered by free electrons:

$$\gamma + e^{-} \rightarrow \gamma\prime + e^{-}\prime. \tag{3}$$

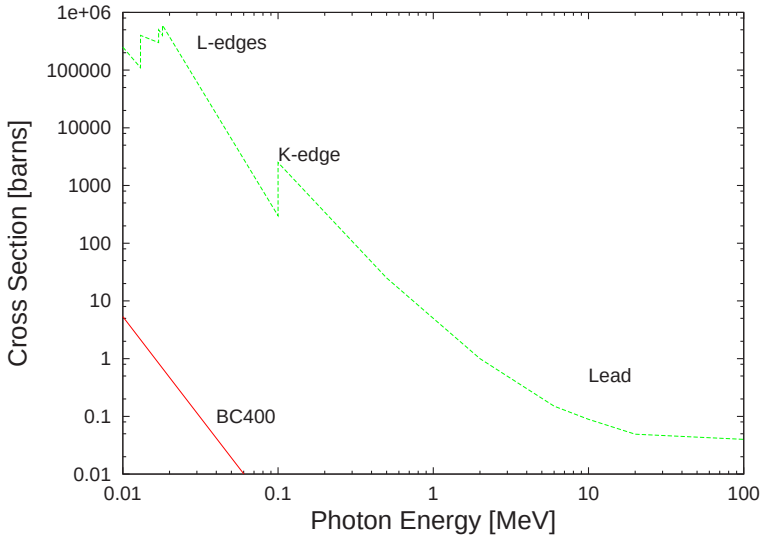

Figure 3: Photoelectric cross sections for lead (dotted line) and BC 400 plastic scintillator (solid line). Note that 1 barn = 10^{-24} cm^2.

Although the electrons in matter are bound, if the binding energy is small in comparison to the photon energy, they can be considered quasi-free. This allows the kinematics of the process to be found easily from conservation of energy and momentum.

The differential cross section for Compton scattering from a single free electron is given by the Klein-Nishina formula [Leo94],

$$\frac{d\sigma}{d\Omega} = \frac{r_e^2}{2}\frac{1}{[1+\kappa(1-\cos(\theta))]^2}\left(1+\cos^2(\theta)+\frac{\kappa^2(1-\cos(\theta))^2}{1+\kappa(1-\cos(\theta))}\right), \tag{4}$$

where r_e is the classical electron radius, κ is the incident photon energy over the electron rest energy, θ is scattering angle of the photon and $d\Omega$ is the solid angle. Integrating this equation over all solid angles and multiplying by the atomic number of the medium, Z, yields the total cross section for Compton scattering:

$$\sigma_{Compton} = 2\pi Z r_e^2\left\{\frac{1+\kappa}{\kappa^2}\left(\frac{2(1+\kappa)}{1+2\kappa}-\frac{1}{\kappa}ln(1+2\kappa)\right)+\frac{1}{2\kappa}ln(1+2\kappa)-\frac{1+3\kappa}{(1+2\kappa)^2}\right\}. \tag{5}$$

The cross section has a linear Z dependence and drops with increasing photon energy as shown in Fig. 4.

The amount of energy that is deposited in a medium by a photon that interacts via Compton scattering is dependent on the scattering angle, θ, and the thickness of the medium. Energy transferred to an electron divided by the electron rest energy, E_{e^-}, in a single interaction, can be described in terms of θ as

$$E_{e^-} = \kappa\left(1-\frac{1}{1+\kappa(1-\cos(\theta))}\right). \tag{6}$$

After the initial interaction there still exists the probability for the photon to interact again and deposit more energy.

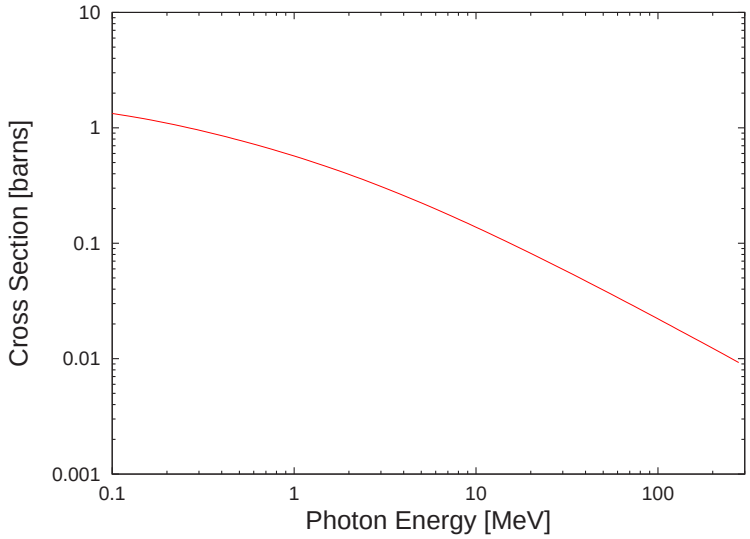

Figure 4: Compton scattering cross section for BC 400 scintillator

2.1.3 Pair Production

The process by which photons in matter transform into electron-positron pairs is called pair production:

$$\gamma \rightarrow e^+ + e^-. \tag{7}$$

To conserve energy this process can only occur for photons with an energy greater than $2m_ec^2$. Furthermore, the presence of a nucleus is required to conserve momentum.

Cross sections for this process depends on the electric field felt by the photon as it nears an atom. Atomic electrons affect this field by screening the incident photon from the Coulomb field of the nucleus. The screening parameter, ξ, is defined as

$$\xi = \frac{100 m_e c^2 h\nu}{E_+ E_- Z^{\frac{1}{3}}}, \tag{8}$$

where E_+ is the total energy of the outgoing positron and E_- is the total energy of the outgoing electron [Leo94]. Complete screening is indicated by $\xi \simeq 0$ and no screening is indicated by $\xi \gg 1$.

Using a Born approximation, the differential cross section is given as [Leo94],

$$\begin{aligned} d\sigma_{pair} &= 4Z^2 r_e^2 \alpha \frac{dE_+}{(h\nu)^3} \\ &\times \left\{ (E_+^2 + E_-^2) \left[\frac{\phi_1(\xi)}{4} - \frac{1}{3}\ln(Z) - f(Z) \right] + \frac{2}{3} E_+ E_- \left[\frac{\phi_2(\xi)}{4} - \frac{1}{3}\ln(Z) - f(Z) \right] \right\}, \end{aligned} \tag{9}$$

where $\phi_1(\xi)$ and $\phi_2(\xi)$ are screening functions approximated by the empirical formula

$$\begin{aligned} \phi_1(\xi) &= 20.863 - 2\ln[1 + (0.55846\xi)^2] - 4[1 - 0.6\exp(-0.9\xi) - 0.4\exp(-1.5\xi)], \\ \phi_2(\xi) &= \phi_1(\xi) - \frac{2}{3}(1 + 6.5\xi + 6\xi^2)^{-1}. \end{aligned} \tag{10}$$

A small correction to the Born approximation

$$f(Z) \simeq a^2 \left[(1+a^2)^{-}1 + 0.0206 - 0.0369a^2 + 0.0083a^4 - 0.002a^6 \right], \tag{11}$$

where $a = \alpha Z$, takes the Coulomb interaction between the positron, electron and nucleus into account. Integration of Eq. 9 can be performed numerically to yield the total cross section for pair production as shown in Fig. 5. The magnitude of the cross section is dependent, approximately, on Z^2. The cross section remains constant for higher photon energies.

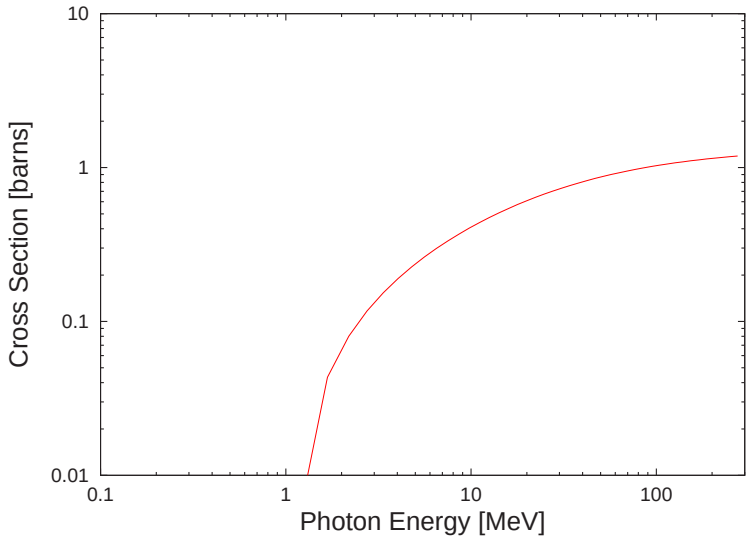

Figure 5: Pair production cross section in BC 400 scintillator.

The creation of an electron-positron pair inside a medium can lead to a wide range of energy being deposited in the medium. $2m_ec^2$ is needed to create the pair and the remainder, $h\nu - 2m_ec^2$, goes into their kinetic energy. The pair can now lose energy through ionization of the medium, annihilation, or be converted to a photon through bremsstrahlung interaction with the Coulomb field of a nucleus.

2.1.4 Electron Interactions

All three of the photon interaction methods previously discussed result in the photon's energy being either wholly or partly transferred to one or more electrons. Therefore, to find the energy deposited by gamma-rays in a medium, electron interaction formulae are required. Electrons traveling in a medium can lose energy either by collisions with particles in the medium or by radiation of photons, commonly known as bremsstrahlung, so these two processes will be explored.

The relationship between the incident photon energy, $h\nu$, and the kinetic energy of the resulting electrons, E_{e^-}, in units of m_ec^2, is different for each interaction. In the case of Compton scattering E_{e^-} was given by Eq. 6 which ranges from 0 to $E_{e^-} = \kappa / \left(1 + \frac{1}{2\kappa}\right)$ at

the Compton edge. For pair production E_{e^-} is approximately $h\nu - 2m_ec^2$. E_{e^-} for the photoelectric effect is $h\nu$ minus the binding energy of the electron, which is of the order of tens of eV.

Electron collisional losses are calculated using a variation of the Bethe-Bloch formula [2] that is modified for electrons. The energy loss per distance traveled for an electron is

$$-\frac{dE}{dx} = 2\pi N_a r_e^2 m_e c^2 \rho \frac{Z}{A}\frac{1}{\beta^2}\left[ln\frac{E_{e^-}^2(E_{e^-}+2)}{2(I/m_ec^2)^2} + F(E_{e^-}) - \delta - 2\frac{C}{Z}\right], \tag{12}$$

where N_a is Avogadro's number, A is the atomic weight, ρ is the target density, C is a shell correction, δ is a density correction, I is the mean excitation potential and β is the relativistic velocity, $\frac{v}{c}$, of the incident electron [Leo94]. The function $F(E_{e^-})$ is given by

$$F(E_{e^-}) = 1 - \beta^2 + \frac{\frac{E_{e^-}^2}{8} - (2r_e+1)ln2}{(E_{e^-}+1)^2} \tag{13}$$

for electrons and

$$F(E_{e^-}) = 2ln2 - \frac{\beta^2}{12}\left(23 + \frac{14}{E_{e^-}+2} + \frac{10}{(E_{e^-}+2)^2} + \frac{4}{(E_{e^-}+2)^3}\right) \tag{14}$$

for positrons [Leo94].

Radiative losses are calculated by integrating the bremsstrahlung cross section times the emitted photon energy over the allowable emission energies:

$$-\frac{dE}{dx} = N\int_0^{\nu_o} h\nu \frac{d\sigma_{brem}}{d\nu}(E_o,\nu)d\nu. \tag{15}$$

Bremsstrahlung is, theoretically, just the inverse process of pair production: in pair production photons turn into electrons and in bremsstrahlung, electrons give off photons. The formula used to find the bremsstrahlung cross section is dependent on the initial total energy of the electron, E_o, and the final total energy of the electron, E, and is expressed as

$$\begin{aligned} d\sigma_{brem} &= 4Z^2 r_e^2 \alpha \frac{d\nu}{(\nu)^3} \\ &\times \left\{(1+\frac{E}{E_o}^2)\left[\frac{\phi_1(\xi)}{4} - \frac{1}{3}\ln(Z) - f(Z)\right] - \frac{2}{3}\frac{E}{E_o}\left[\frac{\phi_2(\xi)}{4} - \frac{1}{3}\ln(Z) - f(Z)\right]\right\} \end{aligned} \tag{16}$$

which is nearly the pair production cross section found in Eq. 9. The remaining quantities are as described in Sec. 2.1.3.

[2] The Bethe-Bloch formula is a quantum mechanical calculation for the energy loss of heavy particles through inelastic collisions and elastic scattering.

2.1.5 Interaction Simulation

To make use of the theory developed thus far, a Monte-Carlo simulation can be employed to model the behaviour of large numbers of photons as they interact. The particular simulation program used in this project was GEANT 3 [CER03], which was developed at CERN, specifically for high energy physics. It is capable of tracking individual particles through complex geometries, simulating their interactions and recording information on the particles' parameters. It has a very useful role in this project because it can reliably simulate the energy absorbed in a material of arbitrary geometry under bombardment by gamma-rays.

In GEANT, it is the responsibility of the user to assemble the appropriate Fortran program segments and utilities into an executable program and to provide the data describing the experimental environment. The process involved in a GEANT simulation consists of initialization, event processing and termination.

When a GEANT 3 simulation is complied and run, the initialization phase prepares the simulation. It begins by generating data structures on the materials and particles used in the simulation. Then the geometry description is read and data structures corresponding to the different medium parameters are generated. Any user defined histograms are set up and energy loss and cross section tables are computed and stored.

In the event processing phase, each particle is individually tracked through the simulation volume. Cross section data are used to generate the probabilities of a particle interacting, through all possible processes, at each step of the particle. The Monte-Carlo method is then used to determine if an interaction takes place, and if so, which one. When an interaction occurs, the information on any secondary particles created is stored until the primary particle has exited the simulation, then the secondaries are processed. At the end of each event the relevant data structures are output.

The termination phase begins when all particles have been handled. It consists of closing the simulation and outputting any statistical information on the process.

2.2 Scintillation

Scintillation is the process by which certain materials emit small flashes of light when struck by a subatomic particle or radiation. Detecting the location and intensity of this light provides a method for measuring a beam profile. To facilitate the use of a scintillator in the design of a beam profiling instrument the physical process involved and the efficiency with which these processes convert incident radiation to light were investigated.

2.2.1 The Scintillation Process

There are two types of scintillator, inorganic and organic, that have fundamentally different mechanisms responsible for their light emitting characteristic. Inorganic scintillators are usually crystals with added impurities and include NaI(Tl), CsI(Tl), LiI(Eu) and BGO while organics are most often polymerized solids and include anthracene and naphtalene.

The mechanism involved in inorganic scintillation begins when the incident ionizing radiation excites an electron from the valence band of the solid to the conduction band. When the electron jumps back into the valence band an energy equivalent to the band gap, usually 5 to 10 eV, is released as a photon. It is also possible for the incident radiation to promote a valence electron to an energy level just below the conduction band called the exciton band. An electron in this state is still electro-statically bound to the hole that it left in the valence band. This electron-hole pair is fairly stable and can migrate throughout the crystal lattice until it encounters an impurity in the crystal structure. At this point the hole left in the valence band can ionize the impurity atom. When a subsequent electron arrives at the impurity it can be trapped by the ion causing the emission of de-excitation radiation.

The scintillation mechanism involved in organic scintillators is a multistage fluorescent process (see Fig. 6). A primary fluorescence agent is responsible for absorbing energy from ionizing radiation by promoting electrons to higher energy levels. It then releases this energy as the electrons return to their ground states. The presence of other fluorescent materials, called fluors, are required because the photons only travel short distances before they are absorbed, making the detector opaque to photons with the wavelength emitted by the primary fluorescent agent. The flours absorb the energy emitted by the primary fluorescent agent and emit it as photons with a wavelength that can exit the scintillator. A resonant dipole-dipole interaction called Foerster energy transfer is responsible for the transfer of energy between the primary fluorescent agent and the flour [Gro00].

Either type of scintillator could be used in a beam profiling capacity but an organic scintillator called BC 400 was chosen for this project. Inorganic crystals would have provided the highest photon interaction cross section because of their high atomic number. However, they can be difficult to work with because many of them are hygroscopic and require a protective enclosure to prevent contact with the moisture in the air. Organics, on the other hand, are not hygroscopic and can be dissolved into plastic making them very easy to work with. Organics are also generally less expensive than inorganics.

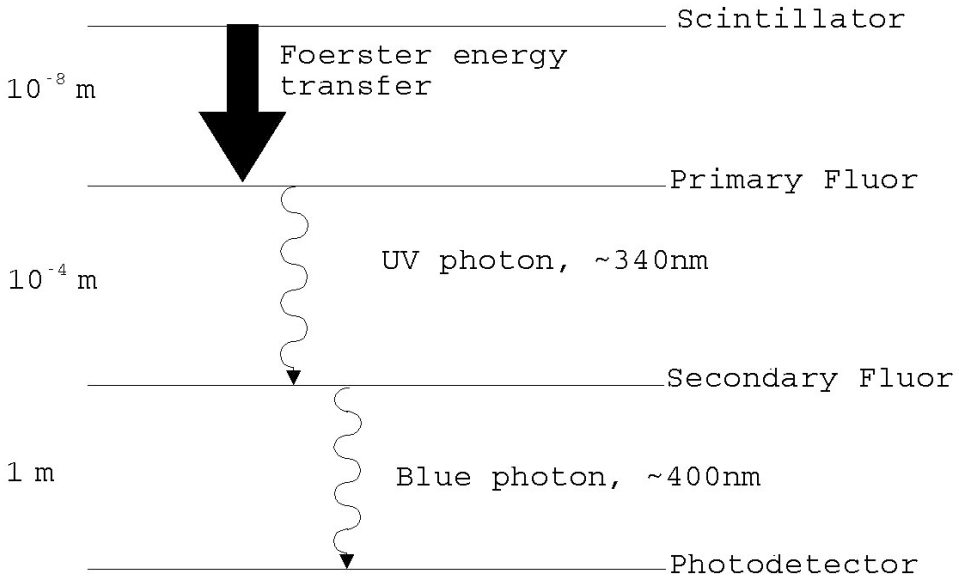

Figure 6: Sketch of the scintillation process for a three component plastic. The approximate absorption lengths are shown on the left [Gro00].

2.2.2 Absolute Scintillation Efficiency

Absolute scintillation efficiency, η, refers to the ratio of visible light energy emitted by a scintillator to the energy deposited in the scintillator by incident radiation. This is an important parameter because it can be used, in conjunction with energy deposition predictions from a GEANT simulation, to model the intensity of light given off by a scintillator that is placed in a gamma-ray beam.

A complex method for theoretically calculating the absolute scintillation efficiency of a given material is given by Birks [Bir64]. For the design purposes encountered in this project, however, it is sufficient to use efficiency values given by the manufacturer. It is customary for a manufacturer to specify the efficiency of a scintillator as a percentage of the absolute efficiency of an organic scintillator called anthracene which has an absolute efficiency of 0.04 [Bir64].

BC 400 plastic scintillator has a relative efficiency of 65%, giving it an absolute scintillation efficiency of 0.03. This parameter will be used to relate the GEANT simulation results for power deposited in the scintillator to power emitted by the scintillator. Table 1 shows some properties of BC 400. Other scintillators manufactured by Bicron are shown for comparison.

Type of Scintillator	BC 400	BC 404	BC 408	BC 412	BC 416
Light Output, % Anthracene	65	68	64	60	38
Light Attenuation Length, cm	160	140	210	210	210
Wavelength of Max. Emission, nm	423	408	425	434	434
No. of H Atoms per cm^3, $\times 10^{22}$	5.23	5.21	5.23	5.23	5.25
No. of C Atoms per cm^3, $\times 10^{22}$	4.74	4.74	4.74	4.74	4.73
Ratio of H:C Atoms	1.103	1.100	1.104	1.104	1.110
No. of Electrons per cm^3, $\times 10^{23}$	3.37	3.37	3.37	3.37	3.37
Principal uses/applications	general purpose	fast counting	TOF counters, large area	large area	large area, economy

Table 1: Properties of some organic scintillators [Bic00].

2.3 The Charge-Coupled Device

A CCD is an array of solid state capacitors that accumulate photoelectrons created by illumination, and store and transport charge. The high sensitivity and resolution of these devices combined with their low cost and simple operation make them ideal for measuring the intensity and spacial distribution of scintillation. A discussion of the basic principles involved in CCD operation will be undertaken in order to ensure that a CCD can meet the detection criteria for this application. This discussion will also be valuable when choosing a particular CCD for beam monitoring. Finally, a model for the behaviour of a CCD will be developed.

2.3.1 Basic Operation

CCDs are constructed from an array of metal-oxide-semiconductor (MOS) capacitors. These arrays consist of a doped semiconductor, insulating oxide layer and individual gate electrodes configured as shown in Fig. 7. By manipulating the voltage to the gate electrodes in the array it is possible to store and transport charge through the semiconductor.

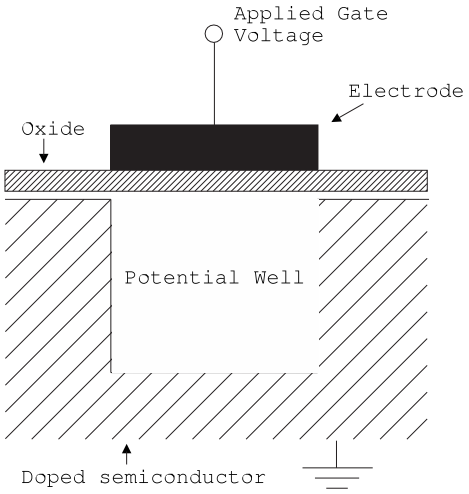

Figure 7: An individual metal-oxide-semiconductor capacitor.

When a voltage is applied to the gate of a MOS capacitor a depletion region is created in the semiconductor below the gate. This depletion region can be thought of as a potential well, or pixel, and provides a location to store charge. In a CCD camera, photons of visible wavelength, with a power density, P_{rad}, incident on an array of MOS capacitors, create n_e electron-hole pairs in the semiconductor via the photoelectric effect (see Sec. 2) at a rate dependent on the quantum efficiency, $R(\lambda)$, and photo-sensitive area, A_d, of the well. These pairs are separated by the electric field in the depletion region and the resulting charge is stored in the potential wells.

To measure the charge stored in each element of the array the voltage on the gates is

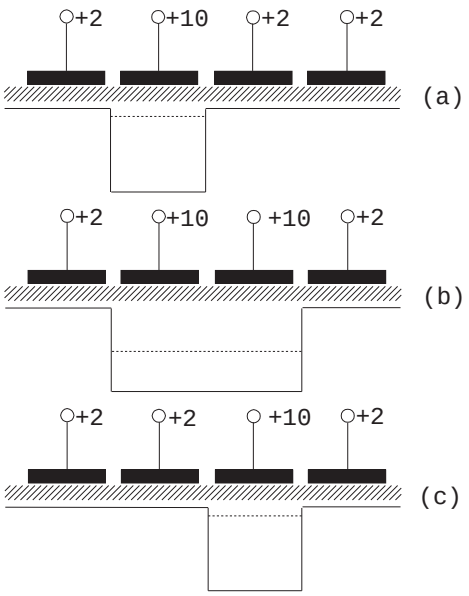

Figure 8: Charge coupling in a CCD array. (a) The charge is accumulated under in one MOS capacitor. (b) The gate voltage of the adjacent capacitor goes high enabling the charge to occupy both potential wells. (c) The initial MOS capacitor gate voltage goes low resulting in the charge being shifted to the neighboring MOS capacitor.

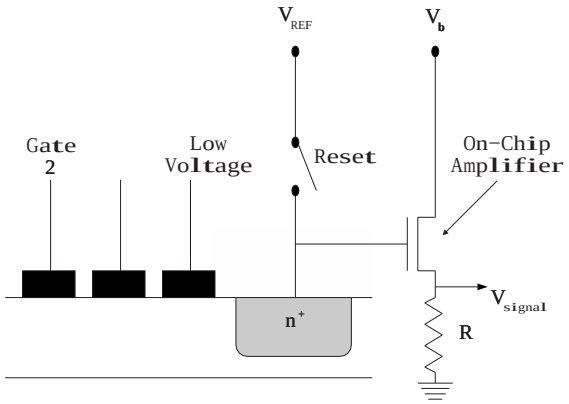

Figure 9: CCD output structure.

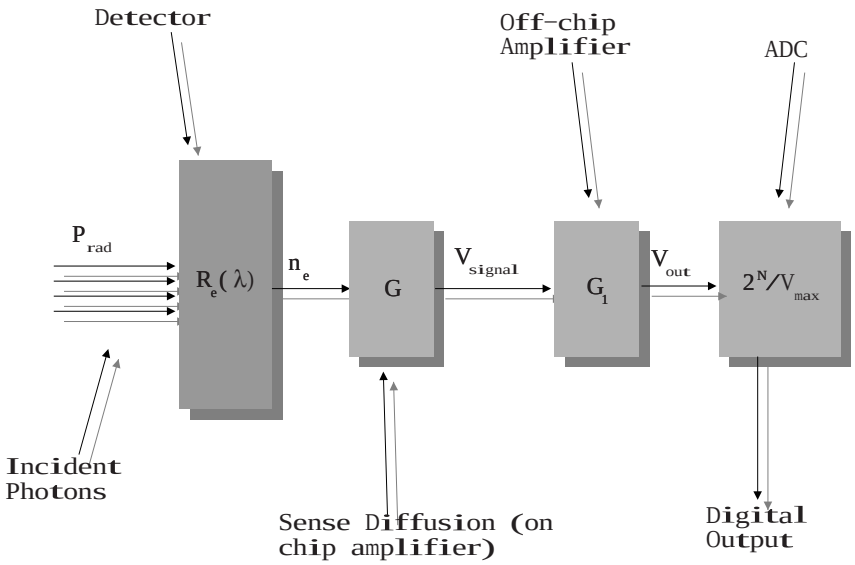

Figure 10: Signal transfer diagram for the acquisition process in a CCD.

manipulated in order to sweep the charge to an output sensor. Fig. 8 conceptually shows how this charge movement takes place.

At one end of the MOS array, a sense diffusion (a strongly biased diode that acts as a capacitor) collects the charge. When a reset pulse is sent, a reference voltage minus the collected charge is applied to the gate of a source-following amplifier, as shown in Fig. 9, which applies a gain, G. Thus the voltage measured at V_{signal} is proportional to the charge collected by the sense diffusion. The signal voltage is then passed through an off-chip amplifier which applies another gain, G_1, before the signal is digitized. The process is outlined schematically in Fig. 10 through the use of a signal transfer diagram.

2.3.2 Binning

If a sensor is operating under low-light conditions its sensitivity can be increased through a process called binning. Binning is simply the process of shifting the charge from more than one sensor element into the sense diffusion. It increases the signal output and the dynamic range of the sensor at the expense of spatial resolution [Hol98]. Binning is controlled by the camera control system.

Not all cameras are capable of binning. If the sense diffusion is not large enough to accommodate extra charge it will saturate. Also, some cameras do not come with software that is capable of implementing binning. Because of the low light levels expected in this project, choosing a camera that was capable of binning was important.

2.3.3 Responsivity

To study the feasibility of using a CCD sensor in a beam profiling capacity, the sensors output as a function of the incident photon flux, or responsivity, must be examined. Knowing the responsivity will aid in the production of a general system model by relating the camera output to the incident flux density.

Assume that a CCD with an active area A_d is placed a distance r from a light source with an area of A_s. The radiant power at the sensor, P_{CCD}, in units of W, can be described in terms of the source's spectral radiant emittance, $M_e(\lambda)$, using [Hol98]

$$P_{CCD} = \left(\frac{A_d A_s}{r^2} \int_{\lambda_1}^{\lambda_2} \frac{M_e(\lambda)}{\pi} \, d\lambda \right). \tag{17}$$

$M_e(\lambda)$ describes the radiant power emitted by a source into a sphere per unit area of the source, as a function of wavelength, and is expressed in units of $\frac{W}{m^3}$. The number of photoelectrons generated in the camera, n_p, is then given by

$$n_p = t_{INT} \frac{1}{e} \left(\frac{A_d A_s}{r^2} \int_{\lambda_1}^{\lambda_2} \frac{M_e(\lambda)}{\pi} R_e(\lambda) \, d\lambda \right), \tag{18}$$

where $R_e(\lambda)$ is the spectral responsivity in units of $\frac{A}{W}$, e is the charge of an electron, t_{INT} is the integration time or exposure length and λ_1 and λ_2 are the minimum and maximum wavelengths of light that are emitted. The resulting signal voltage of the array is

$$V_{signal} = \frac{G}{C} e n_p, \tag{19}$$

where G is the gain of the on-chip amplifier and C is the capacitance of the sense diffusion. The quantity $\frac{G}{C}e$ is known as the gain conversion of the sensor. Inserting the expression for n_p gives the signal voltage as

$$V_{signal} = \frac{G}{C} t_{INT} \frac{A_s A_d}{r^2} \int_{\lambda_1}^{\lambda_2} \frac{M_e(\lambda)}{\pi} R_e(\lambda) \, d\lambda. \tag{20}$$

The signal voltage of a CCD can also be described in terms of the radiant power at the sensor, integration time and the detector's average responsivity, R_{AVE}, using

$$V_{signal} = R_{AVE} P_{CCD} t_{INT}. \tag{21}$$

By combining Eq. 20 and Eq. 21, R_{AVE} can be isolated and found to be

$$R_{AVE} = \frac{G}{C} \frac{\int_{\lambda_1}^{\lambda_2} M_e(\lambda) R_e(\lambda) \, d\lambda}{\int_{\lambda_1}^{\lambda_2} M_e(\lambda) \, d\lambda}. \tag{22}$$

This relationship can be greatly simplified if it is assumed that the light source emits a very narrow band of wavelengths centered around λ_o. Then the integrals vanish and the responsivity can be approximated by

$$R_{AVE} \simeq \frac{G}{C} \frac{M_e(\lambda_o) R_e(\lambda_o) \Delta\lambda}{M_e(\lambda_o) \Delta\lambda} = \frac{G}{C} R_e(\lambda_o). \tag{23}$$

This is the analog responsivity given in terms of the gain of the system and the spectral responsivity of the detector. However, the output of a CCD is digitized so the output voltage is given as a number of counts, N_C, which depends on the number of bits and the full scale voltage, V_{max}, of the converter. For an analog to digital converter (ADC) with N bits the number of counts is given by

$$N_C = int\left[G_1 V_{signal}\frac{2^N}{V_{max}}\right], \tag{24}$$

where the prefix, int, indicates that N_C is a truncated integer value and V_{max} is the product of the output gain conversion, the off-chip amplifier gain, G_1, and the charge of the number of electrons needed to fill the camera, N_{full}:

$$V_{max} = G_1\frac{G}{C}eN_{full}. \tag{25}$$

Using Eq. 21, Eq. 24 and Eq. 25, the number of counts registered by the CCD can be expressed as

$$N_C = int\left[R_{AVE}\frac{1}{e}\frac{2^N}{N_{full}}\frac{C}{G}P_{CCD}t_{INT}\right] = int\left[R_{CCD}P_{CCD}t_{INT}\right]. \tag{26}$$

where R_{CCD} denotes the digital responsivity of the sensor in units of counts per joule. Solving the equality above for R_{CCD} yields

$$R_{CCD} \simeq \frac{2^N}{N_{full}}\frac{1}{e}R_e(\lambda_o), \tag{27}$$

where the expression in Eq. 23 has been used for R_{AVE}. The quantum efficiency, $R_q(\lambda)$, is related to the spectral response through

$$R_e = \frac{e\lambda}{hc}R_q(\lambda), \tag{28}$$

so the responsivity becomes

$$R_{CCD} \simeq \frac{2^N}{N_{full}}\frac{\lambda_o}{hc}R_q(\lambda_o), \tag{29}$$

where h is Planck's constant.

It is often more useful to express the responsivity in terms of the number of photoelectrons that are generated for every joule of energy incident on the sensor. From Eq. 29, it is easy to see that

$$r_{CCD} \simeq \frac{\lambda_o}{hc}R_q(\lambda_o), \tag{30}$$

and the number of photoelectrons accumulated by the sensor in an exposure is

$$n_p = r_{CCD}P_{CCD}t_{INT}. \tag{31}$$

To measure the responsivity, the total number of counts or photoelectrons registered by a camera can be plotted versus t_{INT} while the sensor is exposed to a constant radiant power, P_{CCD}. An ideal plot is sketched in Fig. 11. From Eq. 26 it can be seen that the slope of this relationship will be the responsivity times the power, so if the radiant power incident on the CCD is known, the responsivity can be readily attained.

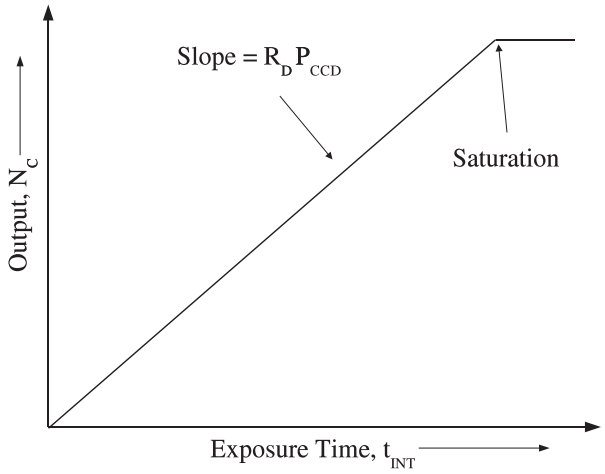

Figure 11: The ideal output versus the exposure time for a uniformly illuminated CCD.

2.3.4 Noise

Noise is introduced into an image captured by a CCD camera at several stages of the acquisition process. This is illustrated in the CCD noise transfer diagram in Fig. 12. This diagram differs from the signal transfer diagram in Fig. 10 in that the sense-node capacitor and the on-chip amplifier gain have been represented separately to allow for the introduction of the reset noise between the two components. Random noise, also called shot noise, n_{shot}, is generated as a result of the statistical nature of photo-detection. A noise floor, or a minimum signal, n_{floor}, arises from noise in the amplifiers, reset circuitry and the analog-to-digital converter. There is also pattern noise, $n_{pattern}$, or noise that results due to the nonuniform characteristics of the pixels in the CCD. The standard deviation of these noise sources gives the system noise,

$$n_{noise} = \sqrt{n_{shot}^2 + n_{floor}^2 + n_{pattern}^2}, \tag{32}$$

in units of root mean squared (rms) electrons. This value can be used to find the uncertainty in the number of counts registered by the camera.

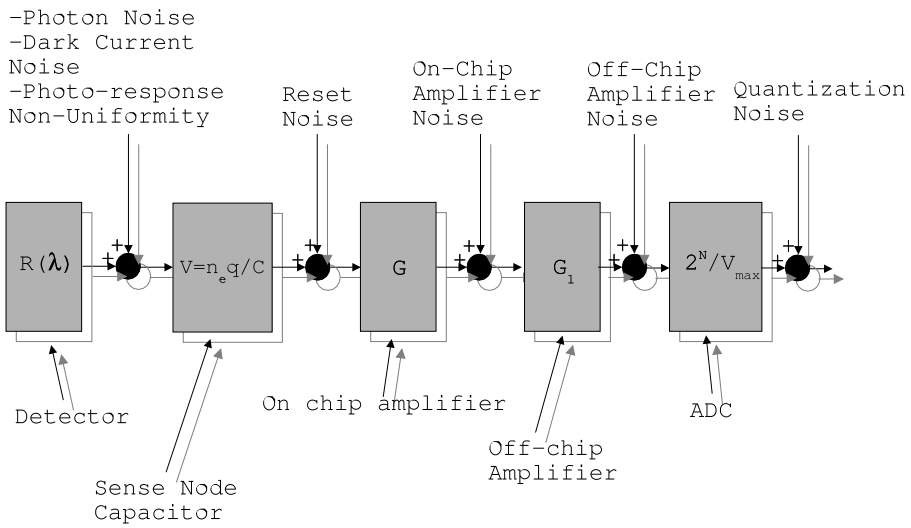

Figure 12: Noise transfer diagram for a CCD.

Photon noise, n_{photon}, and dark current noise, n_{dark}, make up the shot noise in the system. Photon noise is the noise introduced into the signal due to the statistical fluctuation of photon flux and the random nature of photo-generation of electrons. The noise generated is given by Poisson statistics where the variance of the distribution is equal to the mean value. For n_p photoelectrons, given by Eq. 18, the photon noise is given by

$$n_{photon} = \sqrt{n_p}. \tag{33}$$

Dark current, I_{dark}, is a term that describes the rate of charge collection in the camera, during an exposure, that is not attributed to the illumination of the sensor. This current is created by the thermal generation of electrons in the depletion region, bulk substrate material and surface material as well as diffusion of electrons in the bulk material of the sensor. The dark current can be measured by plotting the total CCD output for various exposure times while the CCD is not illuminated. This should result in a graph similar to that in Fig. 13 with the slope of the increasing portion representing the dark current value with units of $\frac{counts}{s}$. For low integration times, the dark current is overshadowed by other noise sources in the system, but for long integration times, typically seen when the illumination level is low, the dark current can make a significant contribution.

Dark current can be removed from the image by subtracting a dark exposure from the image of interest. However, statistical fluctuations in the dark current still contribute to the error in the number of counts. The processes that generate dark current electrons are random and thus have a noise component that is described by Poisson statistics. Therefore, n_{dark}, is the square root of the dark current for a given exposure time, t_{INT}, converted from units of counts to units of electrons:

$$n_{dark} = \sqrt{I_{dark} t_{INT} \frac{N_{full}}{2^N}}. \tag{34}$$

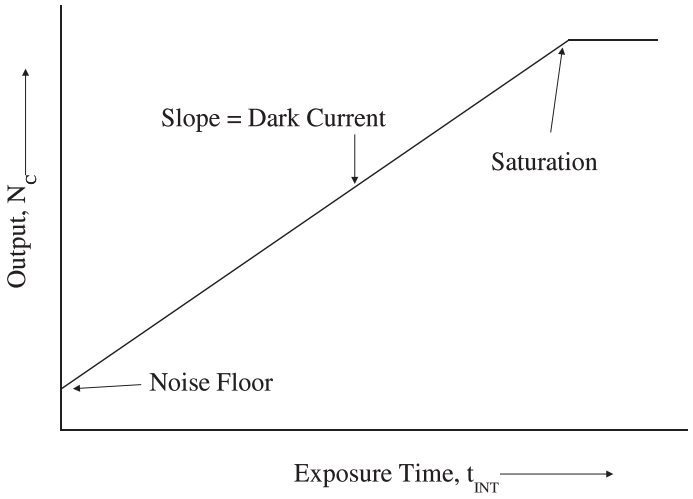

Figure 13: Graph showing the output of a CCD for varying exposure times while the sensor is not illuminated.

The shot noise in the system is calculated by adding n_{photon} and n_{dark} in quadrature:

$$n_{shot} = \sqrt{n_{photon}^2 + n_{dark}^2}. \tag{35}$$

The noise floor, n_{floor}, consists of reset noise, amplifier noise and quantization noise. Reset noise is introduced into the signal when the accumulated charge, or photoelectrons, are sensed. The equivalent circuit for the removal and measurement of charge from a CCD pixel is essentially the same as for the discharging of a capacitor through a resistor (see Fig. 14). The noise current, i_{reset}, from such a circuit is given by

$$i_{reset} = \sqrt{\frac{4kT}{R}\Delta f}, \tag{36}$$

where k is the Boltzmann constant, T is the temperature, R is the resistance and Δf is the noise equivalent bandwidth [Hol98]. In the circuit in Fig. 14, the noise equivalent bandwidth is given by $RC/4$, where C is the capacitance in the circuit, so the noise current becomes

$$i_{reset} = \sqrt{kTC}. \tag{37}$$

When expressed in terms of equivalent electrons the noise is given by

$$n_{reset} = \frac{\sqrt{kTC}}{e}. \tag{38}$$

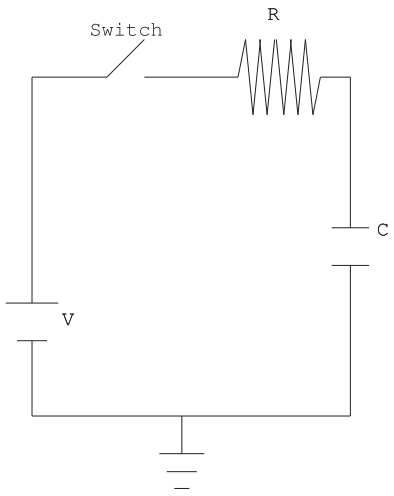

Figure 14: The equivalent read circuit for a typical CCD.

Both the on-chip and off-chip amplifiers add noise to the signal due to voltage and current noise in the amplifier as well as thermal noise in the resistors in the amplifier circuit. The amount of noise added to the signal depends on what type of amplifier is used, the associated circuitry and the noise bandwidth Δf.

For the on-chip amplifier, the noise is given by the

$$n_{on-chip} = \frac{C_{on-chip}}{Gq} V_{on-chip-noise} \sqrt{\Delta f} \tag{39}$$

where $V_{on-chip-noise}$ is the noise voltage generated by the amplifier, given in units of $\frac{V}{\sqrt{Hz}}$, $C_{on-chip}$ is the coupling capacitance and G is the gain of the stage. In the case of the off-chip amplifier,

$$n_{off-chip} = \frac{C_{off-chip}}{GG_1 q} V_{off-chip-noise} \sqrt{\Delta f}. \tag{40}$$

The final step of the acquisition process is the quantization of the output voltage. When the signal is passed through the analog-to-digital converter, uncertainty is introduced due to the discrete levels of output allowed. The noise voltage can be expressed in terms of the voltage represented by the least significant bit, V_{LSB}, in the ADC using

$$V_{quant} = \frac{V_{LSB}}{\sqrt{12}}, \tag{41}$$

where the $\frac{1}{\sqrt{12}}$ factor is introduced by the conversion to rms voltage [Kno00]. The number of electrons that this voltage represents is

$$n_{quant} = \frac{N_{well}}{2^N\sqrt{12}}. \tag{42}$$

The reset noise, amplifier noise and the quantization noise make up the noise floor of the system:

$$n_{floor} = \sqrt{n_{on-chip}^2 + n_{off-chip}^2 + n_{reset}^2 + n_{quant}^2}. \tag{43}$$

The magnitude of the noise floor is easily measured using the same procedure that is used to find the dark current. A plot of the number of counts in an image versus the exposure time, as in Fig. 13, will intercept the y axis at the noise floor. The measured noise floor will have units of counts, but can be converted to the equivalent number of electrons using the full well capacity and the number of bits in the ADC.

Pattern noise, $n_{pattern}$, includes noise components stemming from the photo-response non-uniformity (PRNU) between sensor elements and fixed pattern noise (FPN). It's called pattern noise because it has an effect on the spacial distribution of counts registered by the camera. The PRNU of a sensor array refers to the differences in the responsivity of each pixel. Due to limitations in the semiconductor manufacturing process each pixel element in an array has a slightly different response to uniform illumination. The result is an uncertainty in the number of electrons, in any given bin in the sensor, that is proportional to the number of photoelectrons in that bin. In most scientific grade CCDs this non-uniformity is kept to a minimum but still must be accounted for in the data analysis.

The effects of PRNU can be removed by dividing a flat frame out of the image. The term flat frame refers to an image that is taken while the sensor is uniformly illuminated, with dark frame subtraction, then normalized to 1. By taking the standard deviation of values in a flat frame, σ, and dividing it by the average value, μ, and multiplying that by the number of photoelectrons, n_p, the noise contributions from PRNU can be determined:

$$n_{PRNU} = U_{PRNU} n_p, \tag{44}$$

where [Hol98]

$$U_{PRNU} = \frac{\sigma}{\mu}. \tag{45}$$

FPN refers to the noise introduced by the spacial variation in the dark current. Like PRNU, it is also caused by manufacturing limitations. Differences in the doping concentrations, pixel dimensions, contamination levels and circuit parameters, from pixel to pixel, introduce FPN.

FPN can be measured using the same technique used to measure the PRNU except that dark frames are used instead of flat frames. The magnitude of the FPN is

$$n_{FPN} = U_{FPN} n_{dark}, \tag{46}$$

where U_{FPN} is found as in Eq. 45.

Adding the PRNU and FPN noise in quadrature gives the pattern noise in the camera system:

$$n_{pattern} = \sqrt{n_{PRNU}^2 + n_{FPN}^2}. \tag{47}$$

Adding all the noise sources in quadrature gives the uncertainty in the number of photo-electrons generated for any single potential well in the sensor. To determine the uncertainty in the number of counts in a bin, or δN, n_{noise} can be multiplied by the maximum possible number of counts and divided by the electron capacity of one bin,

$$\delta N = n_{noise} \frac{2^N}{N_{full}}, \tag{48}$$

where care is taken to account for the binning in N_{full}.

2.4 Optics

To create an optical system that is suitable for use in beam profiling, several theoretical considerations must be taken into account. The magnification of the system is of utmost importance and must be calculated to ensure that the image can fit on the CCD sensor. The low illumination levels involved stipulate the importance of determining the aperture and thus the light gathering area of the lens. Additionally, the magnitude of the reflections from each lens must be taken into account. This section will discuss the relevant theories involved in designing a lens system and determining its characteristics.

2.4.1 Lens System Design

An optical system can be specified in terms of the object of interest and the required image through

$$\left[\ IMAGE\ \right] = \left[\ SYSTEM\ \right]\left[\ OBJECT\ \right]. \tag{49}$$

The use of the paraxial ray approximation [Kle70] permits the description of the system through a 2x2 matrix and the image and object through vectors:

$$\begin{bmatrix} \alpha' \\ x' \end{bmatrix} = \begin{bmatrix} a & b \\ c & d \end{bmatrix} \begin{bmatrix} \alpha \\ x \end{bmatrix}. \tag{50}$$

Here the incident light ray is described by a two element array containing the object size, x, and the ray's angle, α, to the optical axis. The system matrix collectively describes the effects of any number of lenses that make up the lens system. Multiplication of the incident ray array and the system matrix provide an array containing the image size and exiting ray angle, x' and α'. Figure 15 shows this relationship graphically.

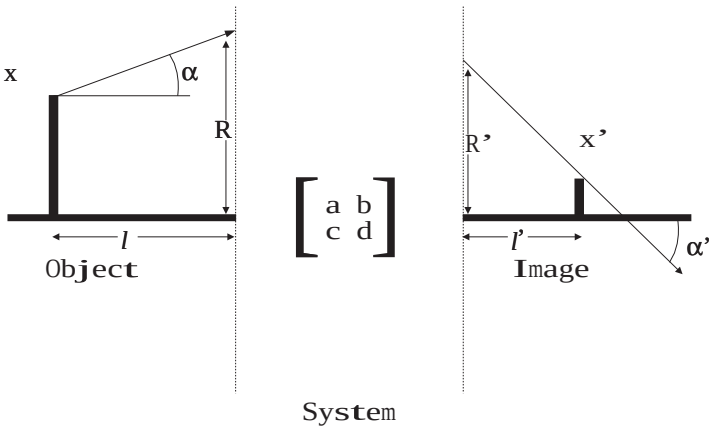

Figure 15: Graphical representation of the system matrix.

The values of the system matrix are restricted by imaging conditions which stipulate that the determinant must be unity and that the magnification of the system, β, is the ratio of the image and object sizes [Bro64]. These restrictions can be expressed as

$$ad - bc = 1 \tag{51}$$

and

$$\beta = \frac{x'}{x}. \tag{52}$$

Substituting these into Eq. 50 gives $c = 0$, $d = \beta$ and $a = \frac{1}{\beta}$, resulting in

$$\begin{bmatrix} \alpha' \\ x' \end{bmatrix} = \begin{bmatrix} \frac{1}{\beta} & b \\ 0 & \beta \end{bmatrix} \begin{bmatrix} \alpha \\ x \end{bmatrix}. \tag{53}$$

The remaining paraxial constant, b, is directly related to the focal length, f, of the system by [Bro64]

$$b = \frac{1}{f}. \tag{54}$$

Once the system matrix is defined for a certain magnification as well as image and object properties, it can be factored into lenses. Each lens in a system can be represented by three matrices that describe the refraction of the light as it enters and exits the lens and the translation as it passes through the lens. For a lens with radii of curvature r_1 and r_2, thickness t and index of refraction μ' this matrix is given by

$$\begin{bmatrix} LENS \end{bmatrix} = \begin{bmatrix} 1 & (\mu' - \mu)\frac{1}{r_2} \\ 0 & 1 \end{bmatrix} \begin{bmatrix} 1 & 0 \\ \frac{t}{\mu'} & 1 \end{bmatrix} \begin{bmatrix} 1 & (\mu' - \mu)\frac{1}{r_1} \\ 0 & 1 \end{bmatrix}. \tag{55}$$

Here r_1 is the radius of curvature of the lens closest to the object, r_2 is closest to the image and μ is the index of refraction of air. Between each lens is a translational component of the system which can be expressed as

$$\begin{bmatrix} TRAN \end{bmatrix} = \begin{bmatrix} 1 & 0 \\ \frac{T}{\mu} & 1 \end{bmatrix}, \tag{56}$$

where T is the distance between lens surfaces. For a given N lens system, there will always be $N-1$ translations involved.[3] The system matrix in Eq. 53 can be produced by multiplying all of the lens and translation matrices together starting from the image side. For example, a three lens system would contain

$$\begin{bmatrix} SYSTEM \end{bmatrix} = \begin{bmatrix} LENS_3 \end{bmatrix} \begin{bmatrix} TRAN_2 \end{bmatrix} \begin{bmatrix} LENS_2 \end{bmatrix} \begin{bmatrix} TRAN_1 \end{bmatrix} \begin{bmatrix} LENS_1 \end{bmatrix}. \tag{57}$$

[3]Note that the translations between the object and the first surface of the lens system, and the last surface of the lens and the image are already included in the definition of the system matrix.

Using this technique, a lens system can be designed based on the required magnification and geometrical criteria. If there are specific lenses available, Eq. 57 can be used to find appropriate translation matrices and thus proper lens separation. This method can also be used to specify the radii of curvature and the thicknesses of the required lenses.

2.4.2 Aperture

The low light levels involved in scintillation imply that special attention must be paid to the light gathering area of the lens. In an ideal lens system, all of the light collected by the lens closest to the object can be focused onto the CDD, but in more practical designs some of that light will miss the remaining elements in the system as in Fig. 16. In these systems each lens element defines an aperture which is simply an area that light can pass through. The limiting aperture in the system is the aperture that dictates the light gathering area of the entire system. The diameter of this area is called the entrance pupil diameter (EPD).

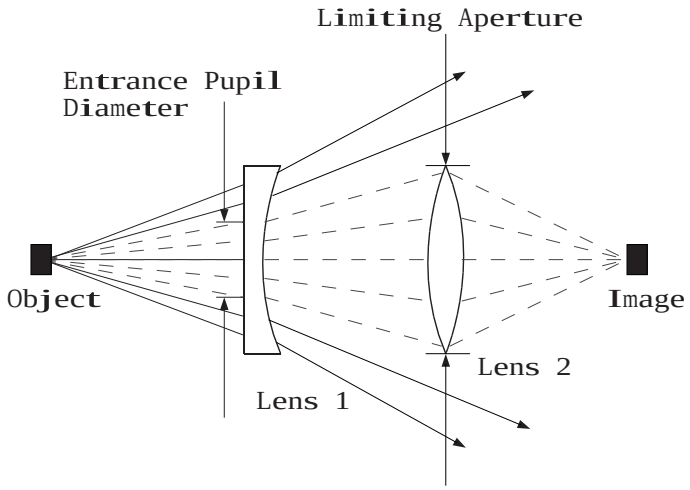

Figure 16: Two lens system showing the relationship between limiting aperture and the EPD. Only the light rays indicated by the dashed lines will form the image.

Finding the limiting aperture of a multi-lens system involves imaging each aperture in object space. Object space refers to the volume on the object's side of the lenses. To clarify this procedure examine Fig. 17. The image of L_3 is created by L_1 and L_2 and the image of L_2 is created by L_1. The image that makes the smallest angle with the optical axis at the object plane is the image of limiting aperture. In Fig. 17, θ_{L3} is less than θ_{L2} so L_3 is clearly the limiting aperture.

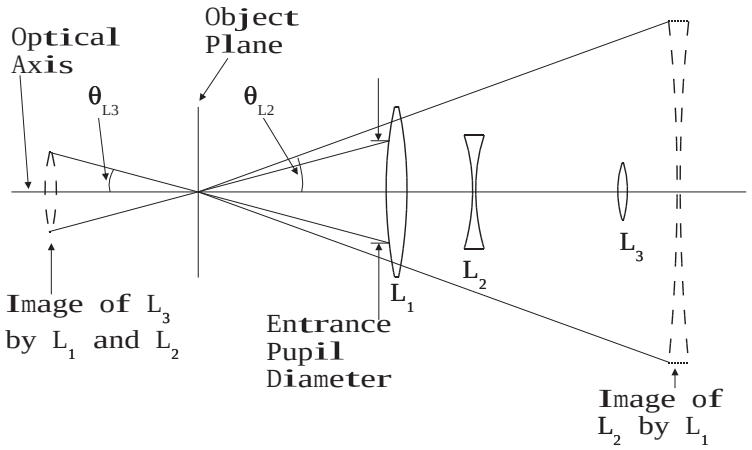

Figure 17: Determining the limiting aperture and EPD of a multi-lens system.

2.4.3 Reflection

Knowing the EPD is crucial to determining the light gathering power of the lens but an analysis of how much of the incident light actually makes it to the sensor is also important. Reflections at each lens surface will inevitably reduce the intensity of the light as it travels through the system due to mismatched index of refraction between the lenses and the air. This reduction in signal strength is easily calculated.

In electromagnetic theory, the ability to transmit energy from a source, through a medium, to a load is affected by the impedance of each component. Therefore, reflectivity coefficient, R, can be given as

$$R = \left(\frac{Z_t - Z_i}{Z_t + Z_i} \right)^2, \tag{58}$$

where Z_i and Z_t represent the impedances of the media containing the incident and transmitted energy. In optics the impedance of a medium is the medium's index of refraction so the relationship becomes

$$R = \left(\frac{\mu_t - \mu_i}{\mu_t + \mu_i} \right)^2. \tag{59}$$

From Eq. 59 it is clear that the closer the indicies of refraction the smaller the reflection.

In a multi-lens system, the total reflection coefficient, R_{lens}, can be expressed as a sum. For a system with M surfaces,

$$R_{lens} = MR + \sum_{i=1}^{M} (M - i) R^{i+1}, \tag{60}$$

and the transmission coefficient is simply

$$T_{lens} = 1 - R_{lens}. \tag{61}$$

3 Development

3.1 Scanning Beam Profiler

At the onset of the project, a scanning profiler that employed a scintillator and photomultiplier tube (PMT) was considered. This design featured two scintillators, positioned in an 'L' shape, connected to a photomultiplier tube via a light guide (Fig. 18). This would be mounted to a drive table that could be extended at a 45^o angle to the vertical, enabling each one of the scintillators to be scanned through the beam individually. A stepper motor would be used to control the position of the scintillator arms.

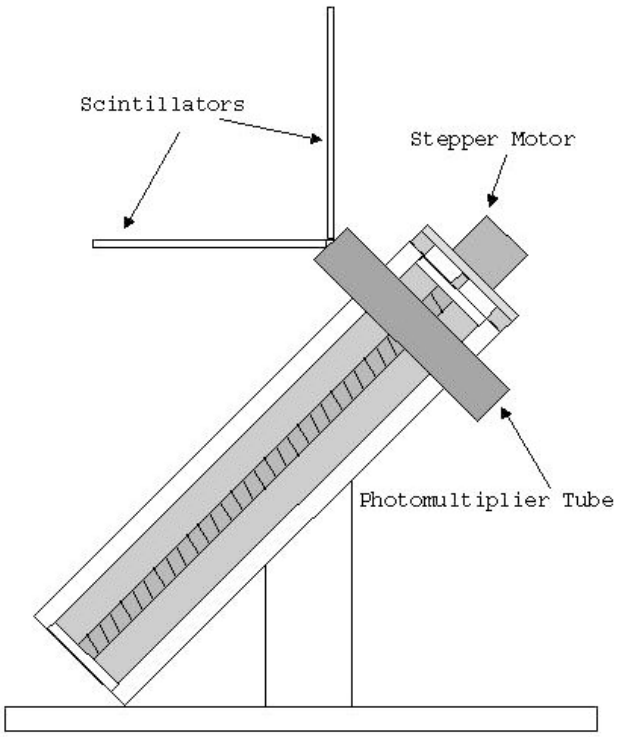

Figure 18: Conceptual drawing of scanning beam profiler.

The positive aspects of this design were its low cost, use of well understood technology and ease of fabrication. The data acquisition and control systems were already in place both in Saskatoon and at HIGS and most of the materials such as the stepper motors and photomultiplier tubes could be obtained from inventory. A drawback to the design was that it's resolution was limited by the thickness of the scintillator arms. Also, scan times could be quite long and the beam couldn't be used for experimentation during the profile scan.

3.1.1 Prototype

A simple prototype was constructed so that testing could be performed to examine the design's feasibility. Figure 19 shows a scale drawing of the prototype.

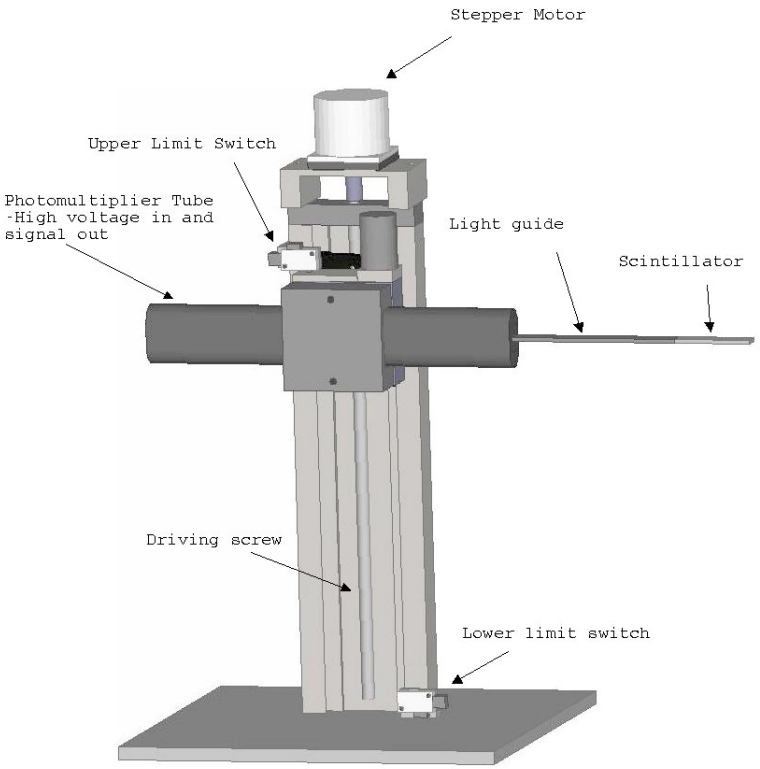

Figure 19: 3D design drawing of prototype scanning beam monitor (scale = 1:$8\frac{1}{3}$).

For simplicity, the prototype was designed with only one scintillator arm. This configuration still allowed for testing of the scintillator, converter, PMT, motor control system and data acquisition system. The design involved using existing parts, where available, and designing new pieces where needed.

An existing drive table, found in inventory, was placed upright on a base. A stepper motor was mounted at the top of the table and attached to the drive screw. The photomultiplier was attached to the front of the sliding part of the table. Limit switches were placed at either end of the movement range to ensure that the motor stopped before contacting the ends of the table frame.

The stepper motor used took two hundred steps per revolution and was attached to a driving screw with seven threads per centimeter resulting in position resolution of approximately seven micrometers per step. Motor control was provided by a Joerger SMC-R Dual Channel Stepping Motor Controller and Driver.

NE102A (or BC 400) was initially chosen as the scintillator because it was already properly fitted to a light guide and PMT. The properties of this scintillator are shown in Table 1. It was in the shape of a parallelepiped with dimensions of 6 cm in width, 0.8 cm in height and 1.2 cm in thickness. The PMT used was a Hamamatsu R1450. This tube has a spectral response range from 300 to 650 nanometers and a peak sensitivity at 420 nanometers [Cor01]. It was attached to a seven-stage PMT base which provided connections for power and signal.

Design was aided by the use of a computer drafting program called VariCAD [var03]. The drive table, PMT, stepper motor and limit switches were measured and drawn into the program. The remaining parts were designed on the computer and printed as design drawings for machinists.

3.1.2 Testing

Testing of the first prototype was carried out to examine the design's feasibility. The apparatus used for testing is shown in Fig. 20.

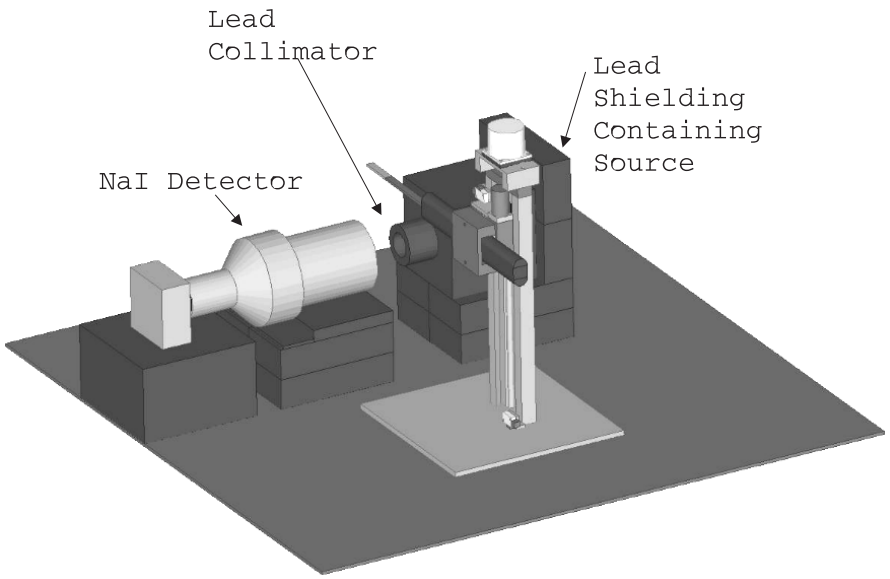

Figure 20: Experimental setup of scanning profile monitor.

The experimental setup included the profile monitor, a NaI detector for calibration, a ^{22}Na gamma-ray source, and a ^{106}Ru electron source. Signal processing and data acquisition electronics were connected as shown in Fig. 21.

The ^{22}Na source was placed in the collimator, 3 cm back from the scintillation arm of the monitor. The stepper motor was set to move down in 4 mm increments and the arm was positioned 20 mm above the top of the collimator. A measurement of the counts over

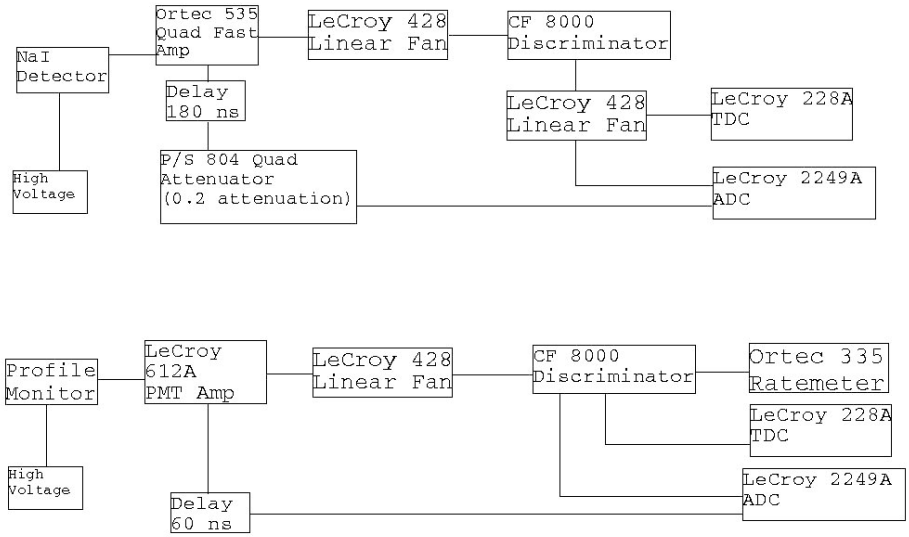

Figure 21: The electronics diagram for preliminary testing of the scanning beam profile monitor. The Ortec 335 Ratemeter was replaced by an Ortec 772 Counter for profiling.

two minutes was taken at each step as the monitor was moved past the collimator opening. The room background was measured for 30 minutes.

3.1.3 Results

The stepper motor and the control system worked well. Movement of the monitor could be controlled from the data acquisition computer and the monitor position could be found by keeping track of the number of steps the motor took. Both limit switches also performed their function properly. The data acquisition system operated properly for all of the tests performed.

A profile of the ^{22}Na source is shown in Fig.22. The background in the room was measured to be 18 counts/s and the maximum source rate was found to be 74 counts/s. Count rates were not totally symmetrical around the center of the collimator, but slightly higher toward the bottom. There could be a number of reasons for this but more testing would have to be done to determine if it is caused by the geometry of the test configuration or detector.

Although the results from the prototype testing proved that the concept was feasible, the scanning beam profile monitor was abandoned. Preliminary investigations into the operation of CCD cameras indicated that the design limitations of the scanning monitor, such as the resolution being limited by scintillator size and the long scan times, could be overcome with a CCD based system.

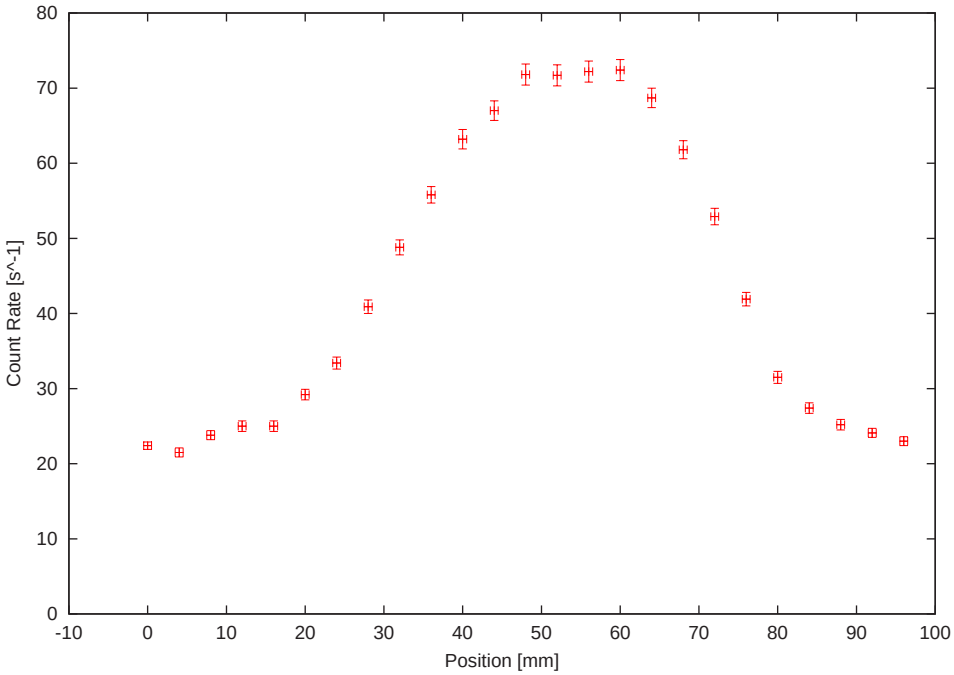

Figure 22: Profile of ^{22}Na source.

3.2 CCD Beam Profiler

The second design featured a CCD and lens system focused onto a large piece of scintillator. The scintillator would be placed in the gamma-ray beam and the CCD and lens system would sit at some angle to the beam axis as shown in Fig. 23. An image of the scintillation pattern would be focused onto the CCD sensor by the lens system. The entire apparatus would have to be enclosed in a light tight box to prevent background illumination from over powering the light emitted by the scintillator and saturating the CCD.

This design was favoured because it was conceptually simpler and more effective than the previous design. Using a thin sheet of scintillator, that is permanently placed in the beam, allows experimentation to continue during profiling because there is very little degradation of the beam flux. Having no moving parts involved simplified the design and eliminated the need for a mechanical control system. The resolution capabilities of CCD's meant more accurate beam profiles would be possible.

There were also some drawbacks to the concept. The required lens system had to be designed and placed within a light tight enclosure meaning the apparatus would be larger than the scanning profiler. There was also a higher cost associated with this design, mainly because of the cost of the CCD camera. Compatibility between the camera control system and the data acquisition system was something that had to be worked out.

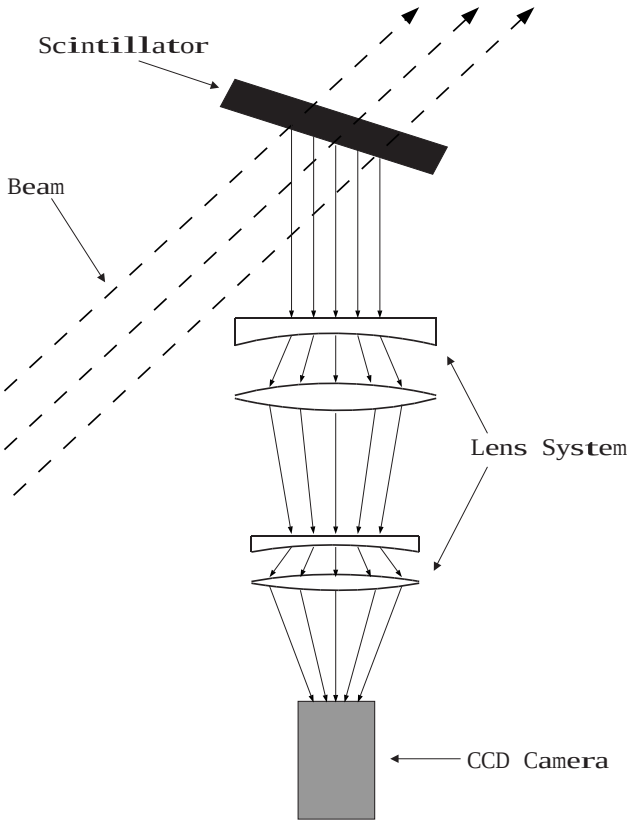

Figure 23: Conceptual drawing of CCD beam profile monitor. The light tight enclosure is not shown. Drawing is not to scale.

3.2.1 System Model

To determine if the beam profiling criteria could be met using the CCD-based design, a simple model of the profiling system was created. The specific purpose of this model was to determine if the intensity of light created by gamma-ray interaction with scintillator was sufficient to be measured with an affordable CCD. The components of this model include a power transmission calculation, an analysis of the responsivity of a CCD sensor and the system responsivity.

To model the power transmitted through the system, the light output power, P_{rad}, was related to the amount of energy deposited per second through the scintillator's absolute efficiency, η, using

$$P_{rad} = \eta P_{absorbed} \tag{62}$$

where $P_{absorbed}$ is the rate at which energy is being deposited in the scintillator by incident gamma-rays.[4] $P_{absorbed}$ can be found using GEANT simulations, as will be discussed in the

[4]The absolute scintillation efficiency of plastic scintillator is discussed in Section 2.2.2.

next section. Assuming that the power emitted by the scintillator is radiated uniformly, the amount of power transferred to the CCD sensor could be found using the EPD and transmission coefficient, T_{lens}, of the required optical system. For a scintillator placed a distance r from the first surface in the lens system, the expression for the power reaching the CCD is

$$P_{CCD} = \frac{\pi\left(\frac{EPD}{2}\right)^2}{4\pi r^2} T_{lens}\eta P_{absorbed} \tag{63}$$

$$= \frac{1}{16}\left(\frac{EPD}{r}\right)^2 T_{lens}\eta P_{absorbed}. \tag{64}$$

where the EPD and T_{lens} can be found for different lens systems as discussed in Sections 2.4.2 and 2.4.3.

In Sec. 2.3.3 it was shown that P_{CCD} could be related to the number of counts read by the CCD through

$$N_C = int[R_{CCD}P_{CCD}t_{INT}]. \tag{65}$$

Substituting the equation for P_{CCD} (Eq. 63) into the relationship above, yields the system model:

$$N_C = int\left[\frac{1}{16}\left(\frac{EPD}{r}\right)^2 R_{CCD}T_{lens}\eta P_{absorbed}t_{INT}\right]. \tag{66}$$

For a more convenient relationship, the responsivity of the sensor can be incorporated in an overall system responsivity, R_{SYS}, that relates $P_{absorbed}$ to the number of counts in the image. N_C is then expressed as

$$N_C = int\left[R_{SYS}P_{absorbed}t_{INT}\right], \tag{67}$$

with

$$R_{SYS} = \frac{P_{CCD}}{P_{absorbed}}R_{CCD} = \frac{1}{16}\left(\frac{EPD}{r}\right)^2 T_{lens}\eta R_{CCD}. \tag{68}$$

The system responsivity in units of electrons per GeV per bin can be extracted from R_{SYS} using

$$r_{SYS} = \frac{1}{J}\frac{N^{full}}{2^{N_{ADC}}}R_{SYS}. \tag{69}$$

Here, J is the number of bins that the image of the beam spot is being focused onto. This formulation of the responsivity will be valuable in the noise analysis.

The relationships in Eq. 67, Eq. 68 and Eq. 69 incorporate all of the variables in a CCD based beam profiling system and generate the expected output of that system. The system responsivity accounts for the responsivity of the CCD, the efficiency of the scintillator and the transmittance and light gathering capabilities of the lens system.

3.2.2 Simulation

At this point of the development, GEANT simulations were used to investigate what $P_{absorbed}$ could be expected. Simulations were used to produce $P_{absorbed}$ values for varying beam energies and scintillator thicknesses. The effects of placing a high Z material against the scintillator, to convert the gamma-rays to electrons before they reached the scintillator, was also investigated along with the beam degradation caused by the monitor. The results provided by these simulations were important in determining how the monitor would perform when placed in the beam.

The effect of the gamma-ray energy on the amount of power absorbed by the scintillator was observed by simulating gamma-rays with energies between 2 MeV and 225 MeV impinging a 6 millimeter thick piece of scintillator. The results of the simulation are shown in Fig. 24. The power deposition values were highest for the lowest gamma-ray energies but dropped sharply for energies around 10 MeV. A slight increase was noticed as the energies increased above 10 MeV.

The behaviour of this graph was what would be expected from an analysis of the cross section information provided in the theory section. A high power absorption, near 20 GeV/s, was seen at the lowest gamma-ray energy due to the relatively high photoelectric cross section. $P_{absorbed}$ drops to a minimum of around 8 GeV/s for beam energies between 10 and 30 MeV because the Compton and photoelectric cross sections continue to decrease. The slight increase of power absorption for the remainder of the graph, up to a maximum of just over 10 GeV/s, was a result of the increase in the pair production probability.

A GEANT simulation of the effect of varying the scintillator thickness on the power absorbed was performed for gamma-ray energies of 2, 10 and 100 MeV. Figure 25 shows the results. For all three gamma-ray energies there was an increase in the power absorbed as the scintillator became thicker. This behaviour was due to the fact that the number of interactions that occur are linearly related to the thickness of the scintillator. For the 2 MeV gamma-rays, this translated into a linear relationship between the amount of power absorbed by the scintillator and its thickness because the electrons generated through interaction did not have sufficient energy to traverse even a thin scintillator. The 10 and 100 MeV gamma-rays initially deposit less energy than the 2 MeV gamma-rays in the thin scintillator because the secondary particles they generate have enough energy to traverse the scintillator. But when the scintillator thickness is increased, the number of photon interactions increases and the amount of energy deposited by the secondaries that are generated also goes up.

The next GEANT simulations were completed to investigate the value of using a converter placed against the scintillator. A converter is simply a material with a high atomic number, and thus a high photon cross section, that is used to convert some of the gamma-rays in the incident beam into electrons. The energy in these electrons can then be more easily absorbed by the scintillator, resulting in an increase in $P_{absorbed}$, at the cost of increased beam degradation.

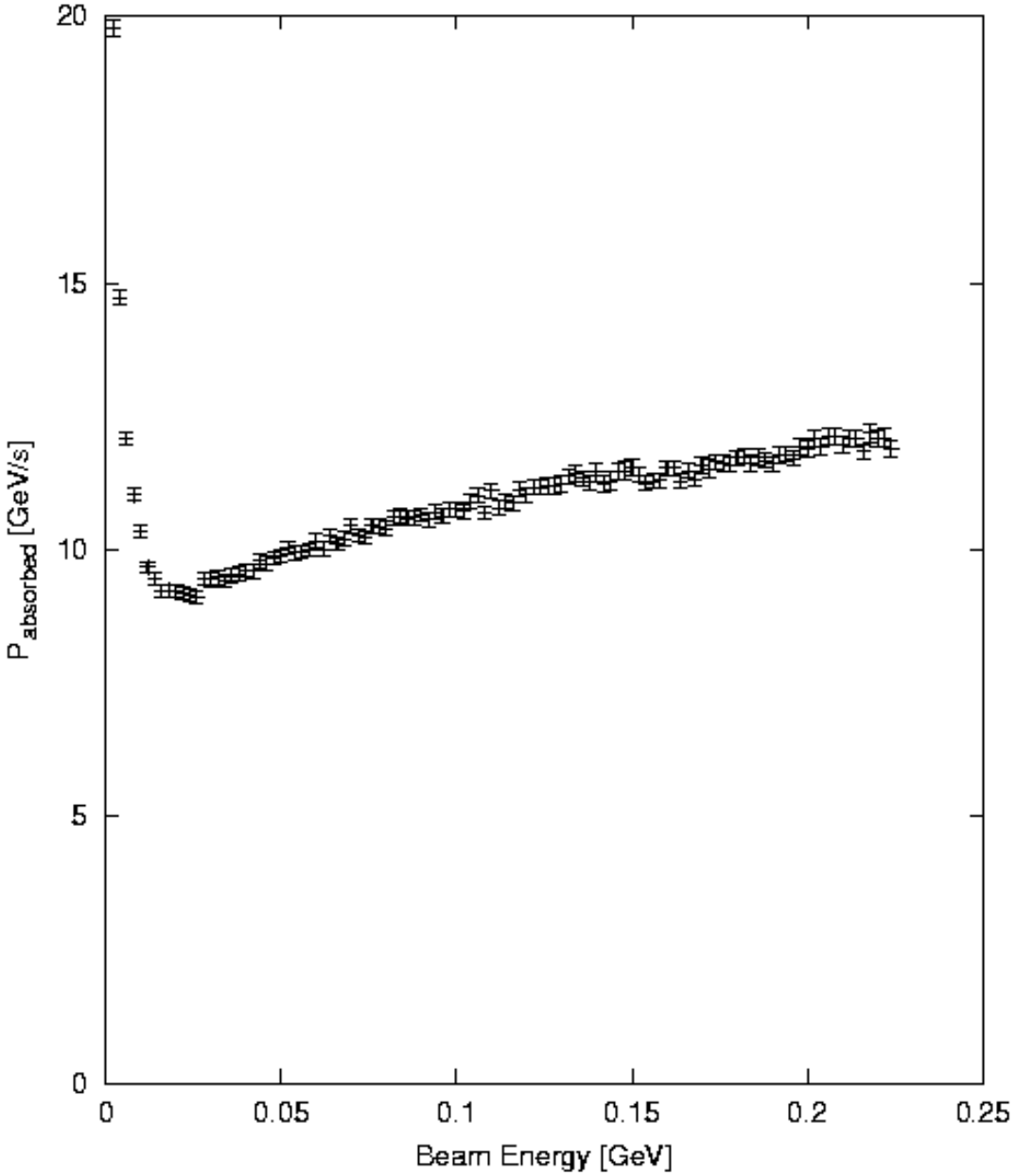

Figure 24: GEANT simulation of the power deposited in 6mm of plastic scintillator vs gamma-ray energy for a beam flux of $10^6\gamma/s$.

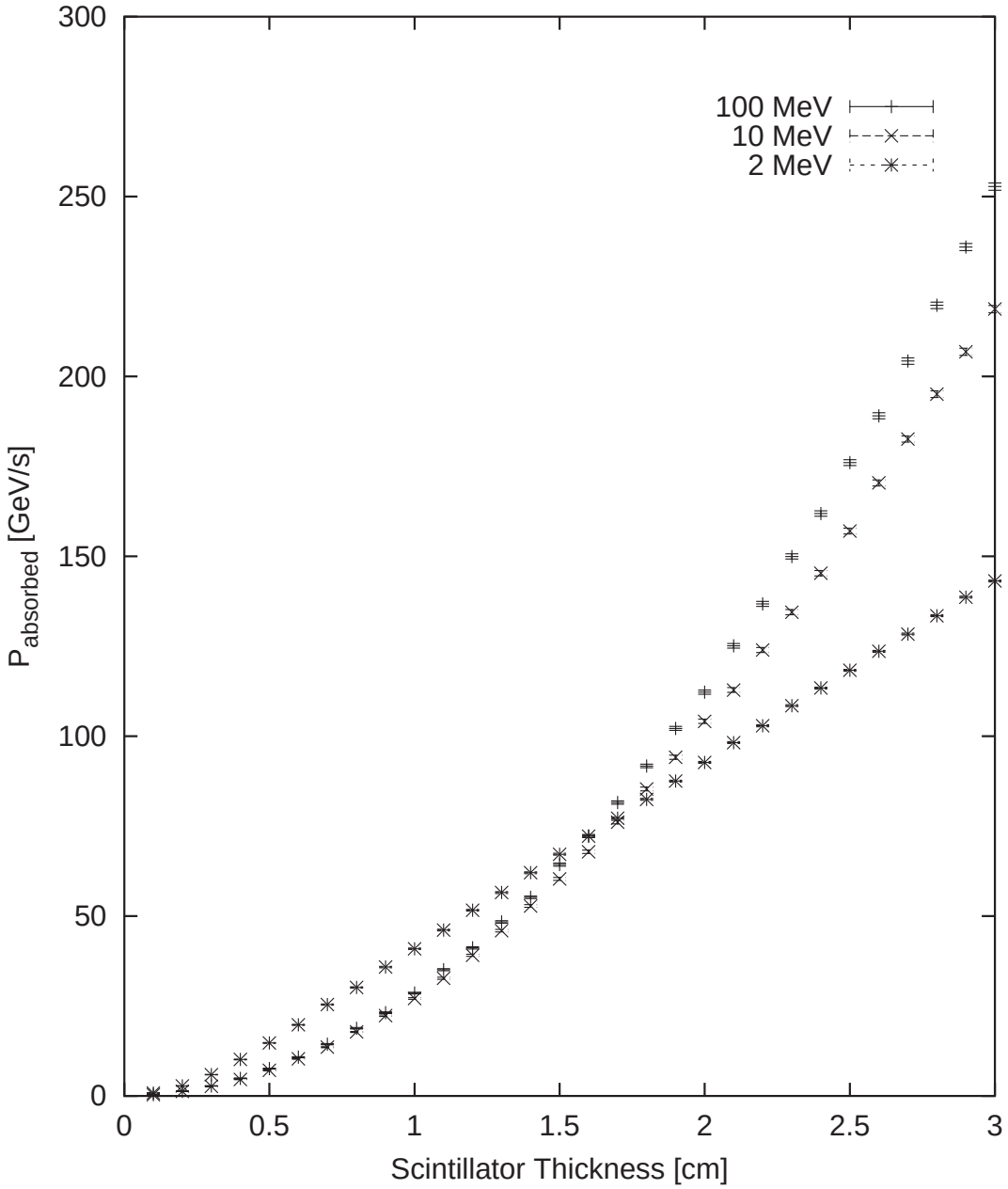

Figure 25: GEANT simulation of the power deposited in varying thicknesses of plastic scintillator by 2, 10 and 100 MeV gamma-ray beams with a flux of 10^6 γ/s.

The first converter simulation examined the relationship between the power absorbed by a 6 mm thick scintillator and the incident gamma-ray energy when 1 mm thick aluminum, iron and lead converters were used. The results of this simulation are shown in Fig. 26. As expected, the $P_{absorbed}$ values are highest for lead which has the largest Z.

The effects of the converter were easily seen by comparing Fig. 24 to Fig. 26. An increase in the power absorbed was observed over the entire gamma-ray energy range. For low energy gamma-rays, the increase is small because the low energy electrons generated in the converter have insufficient energy to make it out of the converter. These results were encouraging because they show that a converter can be used to increase the intensity of light that reaches the CCD thus reducing the demands on the system responsivity, R_{SYS}.

The next converter simulation was completed to investigate the effects of changing the converter thickness on the power absorbed by the scintillator. This was done by simulating a gamma-ray beam with a flux of 10^6 γ/s incident on various thicknesses of iron converters placed against 6 mm of plastic scintillator. Gamma-rays energies of 2, 10 and 100 MeV were used to produce the results shown in Fig. 27.

The results of this simulation showed that there is a maximum effective converter thickness that depends on the energy of the incident gamma-rays. This maximum thickness is related to the range of electrons in the converter medium. In Fig. 27 the 2 MeV gamma-rays introduce a fairly constant amount of power, around 2.5 GeV/s, into the scintillator, regardless of the converter thickness. This is due to the fact that only the electrons produced closest to the scintillator can escape the converter. All other interactions toward the front of the converter have no bearing on the amount of power absorbed and only serve to degrade the intensity of the beam.

The relationship between the maximum effective thickness and electron range was clearly seen in the 10 MeV power absorption line in Fig. 27. Initially, increasing the converter thickness increased the power absorption in the scintillator, but at about 4 mm the power absorption leveled off. At 10 MeV, incident gamma-rays interact through Compton scattering and pair production at a ratio of about four Compton events to one pair production event. The energies of the electrons created from these events could be estimated to be around an average of 5 MeV and their range can be found by looking at the energy range curve for iron (see Fig. 28).[5]

At 5 MeV the range is 3.325 g/cm^2, and dividing this by the density of iron, $\rho_{iron} = 7.874$ g/cm^3, gives an estimated range of 0.42 cm. This is roughly the thickness of converter that produces the maximum power absorption, indicating that increasing the thickness beyond the range of the electrons generated in the converter provides no benefit.

[5]The energies of the electrons generated by 10 MeV gamma-rays were estimated by considering that pair production produces two electrons with energies of (10 MeV$-$1.02 MeV)/2 $\simeq$ 4.5 MeV and Compton scattering generates electrons with a range of energies between 0 MeV and 8 MeV (Compton edge energy). The angular distribution of the Compton electrons dictates that the higher energy electrons will be deflected from the incident photon direction less than the lower energy electrons.

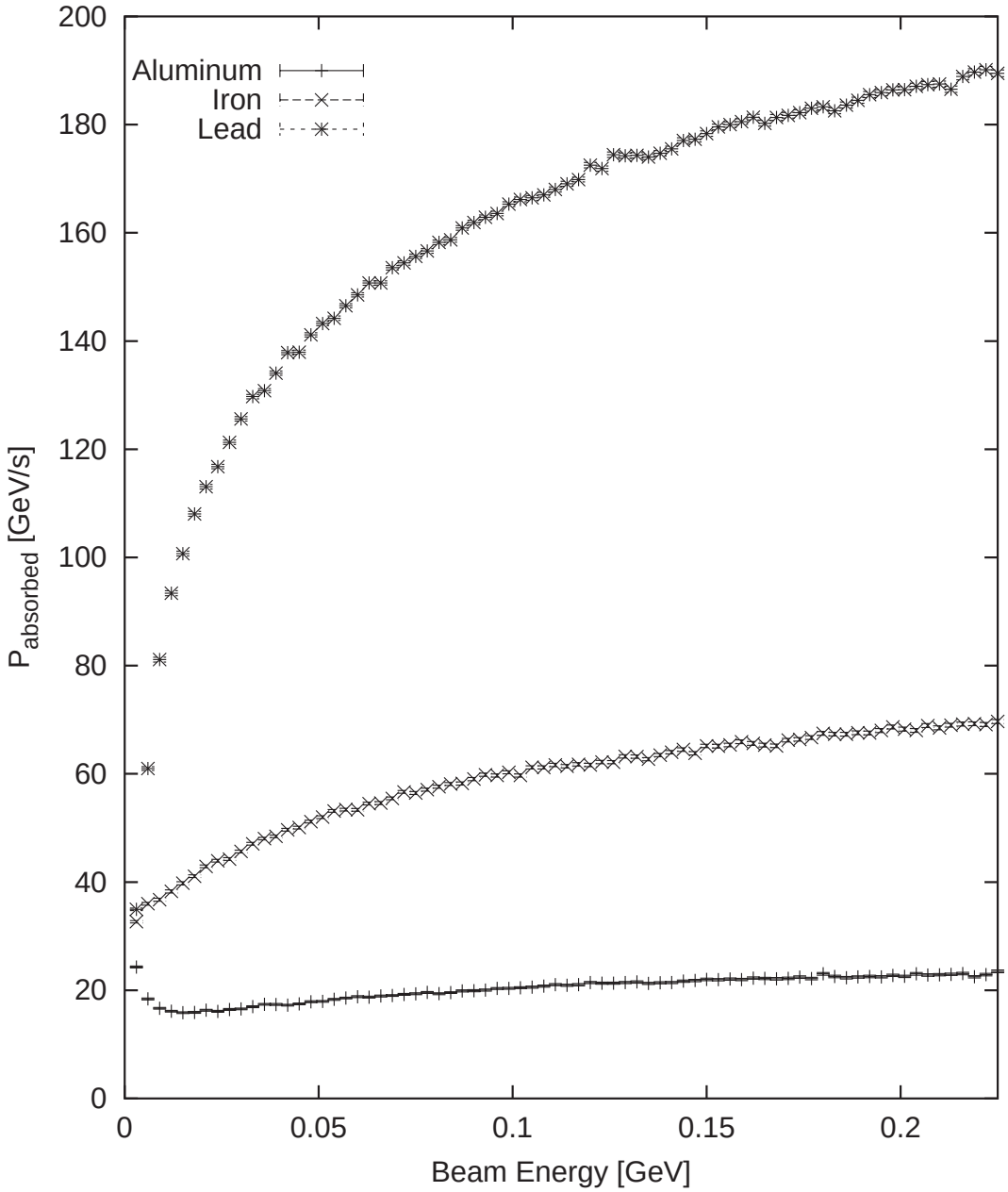

Figure 26: GEANT simulation of the power deposited by gamma-ray beams with a flux of 10^6 γ/s and varying energies in 6 mm of plastic scintillator using 0.6 mm thick iron, aluminum and lead converters.

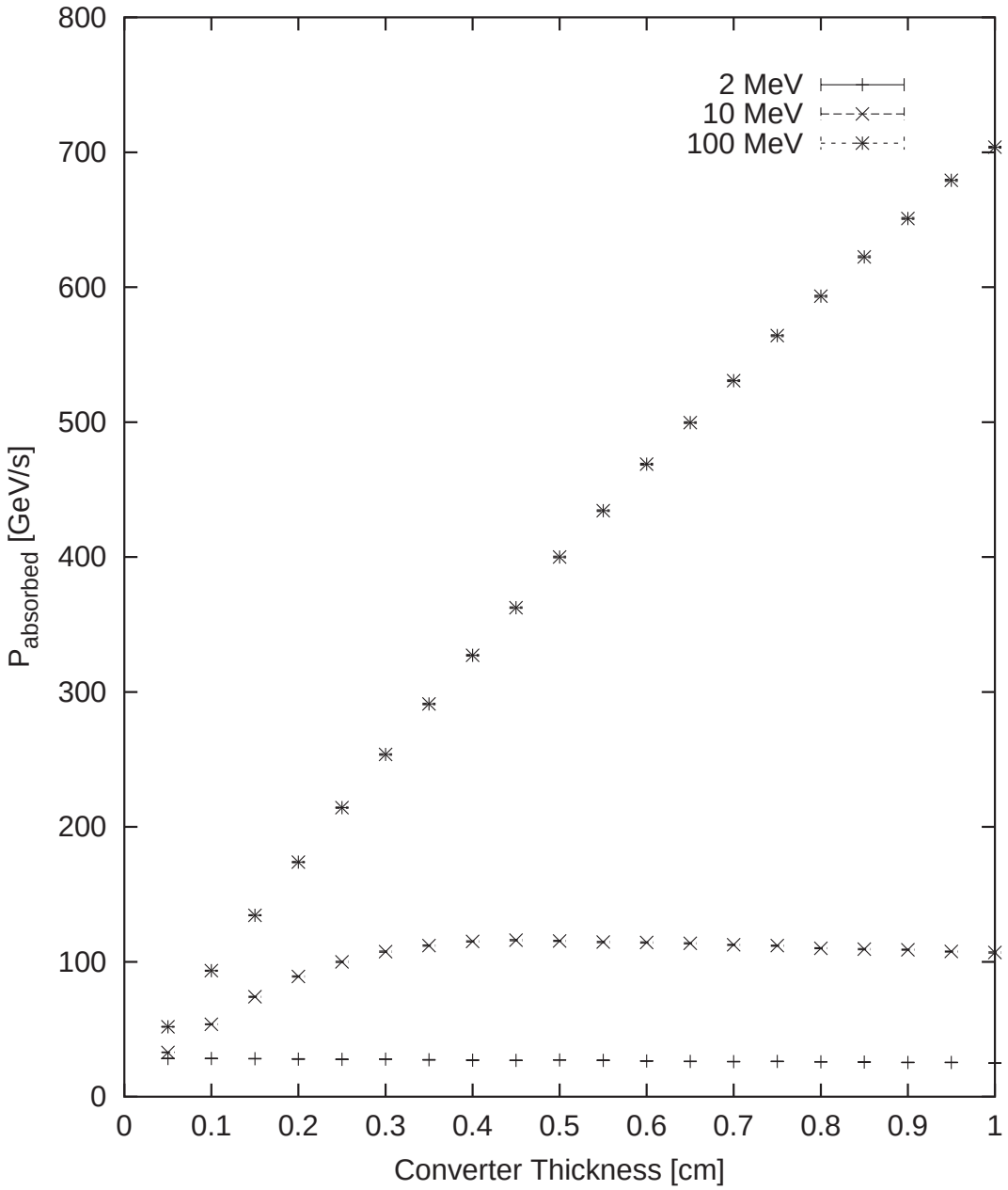

Figure 27: GEANT simulation results for the power deposited in 6 mm of plastic scintillator by 2, 10 and 100 MeV gamma-rays using various thicknesses of iron converter. The beam flux used in the simulation was $10^6\gamma$/s.

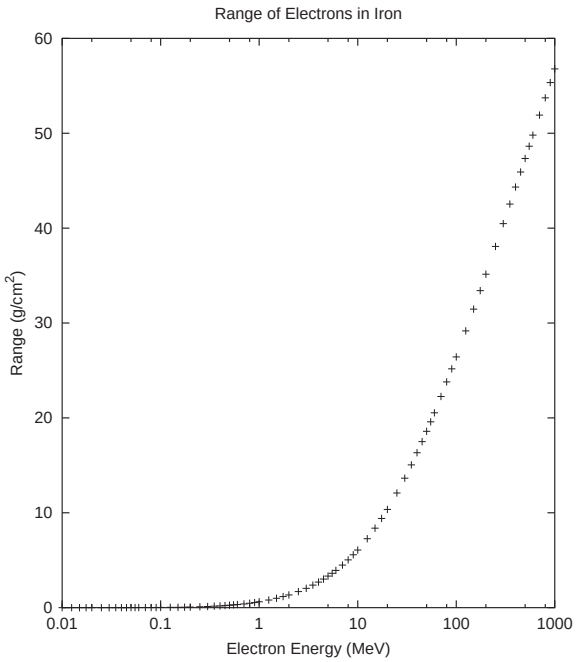

Figure 28: A plot of the range of electrons in iron.

Finally, a simulation showing the degradation of the beam as a result of the scintillator and converter was produced. This was an important simulation because it determined if the monitor would be non-destructive, and thus, be capable of providing profile measurements during an experimental run. In this simulation a target of the same diameter as the beam was placed 2.5 m from the scintillator and the change in flux incurred as a result of the monitor was observed. The beam degradation can then be described as the percentage of gamma-rays, incident on the monitor, that don't reach the target.

Figure 29 shows the effect of increasing beam energy on the beam degradation for a 6.0 mm plastic scintillator and 0.6 mm thick aluminum, iron and lead converters, as well as no converter. These plots are what would be expected from an examination of the effect of Z on the photo-absorption cross sections. The high Z of lead is apparent as increasing beam energy causes increasing beam degradation in proportion to the pair production cross section. Using an iron converter results in an almost constant degradation of around 3%, which falls slightly at higher energies, akin to the Compton cross section. The effect of aluminum is similar to that of iron, but with a bit more of a decrease also due to the decreasing Compton cross section for higher energies.

The beam degradation plots shown in Fig. 29 are shown only for scintillator and converter thicknesses of 6.0 mm and 0.6 mm, respectively. However, the relationship between the thickness and the beam degradation is completely linear, so extrapolation can be used to predict beam degradations for different thicknesses. The results of the beam degradation simulations, for the given thicknesses, show a predicted degradation of less than 7% for lead,

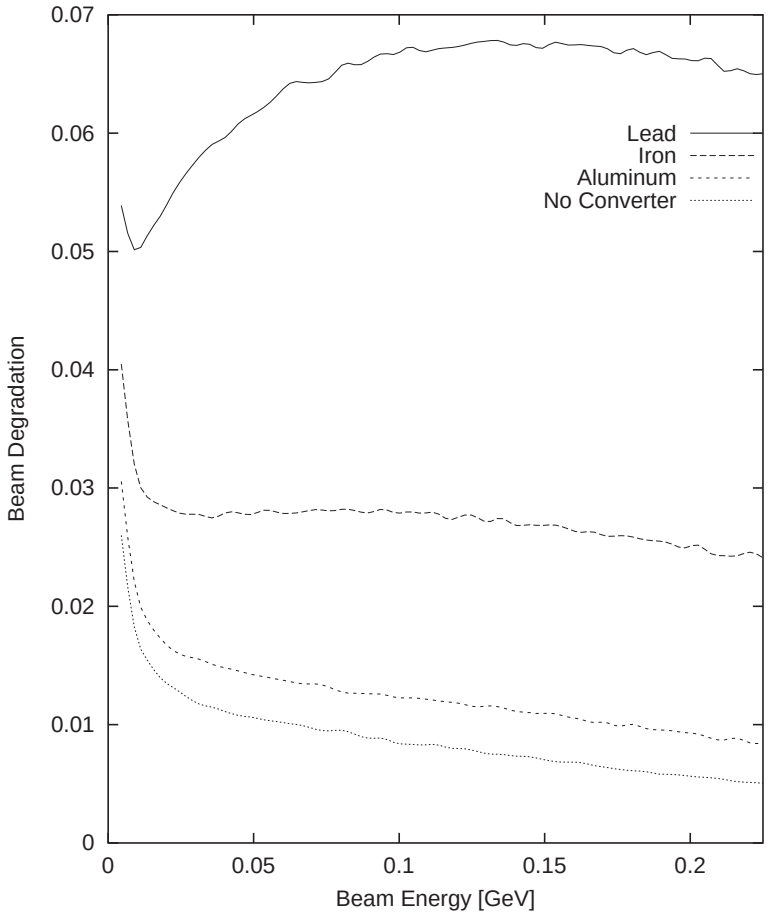

Figure 29: A plot of the beam degradation versus the incident gamma-ray energy when using a 6.0 mm thick plastic scintillator and 0.6 mm thick aluminum, iron and lead converters. The degradation in the case where no converter is used is also shown.

4% for iron, 3% for aluminum and 2% for no converter.

The results of the GEANT simulations showed the relationships between the power absorbed, the beam energy, scintillator thickness and converter thickness for a beam flux of 10^6 γ/s. The specific relationships that should be noted are the improvements in power absorption by the scintillator when used in conjunction with a converter and the correlation between the electron range and the maximum effective converter thickness. It should also be noted that the beam degradation can easily be kept to less than 3% or 4% as long as the scintillator and converter thickness are kept small. These relationships were instrumental in the design of the profiling system when combined with the system model, as described in Eq. 66, as they determine the required CCD sensitivity.

3.2.3 Concept Verification

Before the necessary funding could be secured for the purchase of a CCD camera, a clear example of the concept's validity needed to be shown. This was done by borrowing a CCD

camera from the astronomy lab at the University of Saskatchewan and testing its ability to image scintillation generated by plastic scintillator when exposed to radiation. In addition to validating the concept, experience related to the operation and behaviour of CCD cameras and optical systems was obtained.

The camera used for concept verification was the Meade Pictor 416XT, shown in Fig. 30. The 416XT features a Kodak KAF 0400 front-illuminated CCD with 768 by 512 pixels that are 9 by 9 μm^2 in size. A two-stage thermoelectric cooler was integrated into the 416XT and kept the sensor at around -5^o C. The dark current at this temperature was specified by the chip manufacturer to be 0.35 e^-/pixel/s and the quantum efficiency was 30%.

Figure 30: Photograph of the Meade Pictor 416XT. The box to the right of the camera is the autoguider assembly for controlling a telescope [mea03].

To deposit power into the scintillator a Ruthenium source was used. ^{106}Ru decays to the ground state of ^{106}Rh yielding 0.039 MeV electrons. ^{106}Rh is unstable and decays to ^{106}Pd giving off electrons with a maximum energy of 3.45 MeV. The electrons are created through the decay of a neutron inside the nucleus into a proton, electron and anti-neutrino,

$$n \rightarrow p + e^- + \bar{\nu}_e. \tag{70}$$

Thus their energy depends on the difference in binding energy between the parent and daughter nuclei. The excess energy is manifested as the kinetic energy of the proton, electron and anti-neutrino, but because the proton is much larger then the electron and anti-neutrino almost all of the energy is imparted to the lighter two particles. It is most probable that the neutrino and electron receive equal amounts of energy so the energy spectrum of the beta radiation is peaked at 1.77 MeV [Fir99].

The particular source used had an activity of 100 μCi on November 16, 1993. The half-life, $T_{\frac{1}{2}}$, of ^{106}Ru is 373.5 days and the experiment was carried out on July 2, 2002, so by using the radioactive decay law,

$$N(t) = N(0)exp(-\lambda t), \tag{71}$$

where λ is given by

$$\lambda = \frac{ln2}{T_{\frac{1}{2}}}, \tag{72}$$

a decay rate of 0.289 μCi was obtained. Converting this into Becquerel or disintegrations per second gives 10680 Bq. The amount of power emitted by the source into its immediate surrounding was calculated to be

$$P_{^{106}Ru} = \left(0.039\frac{MeV}{d} + 1.77\frac{MeV}{d}\right) 10680\frac{d}{s} = 19320\frac{MeV}{s}, \tag{73}$$

where d denotes disintegrations.

The source was contained in a small metallic cylinder with a diameter of 1.27 cm and a thickness of 0.63 cm, shown in Fig. 31. On one side of the cylinder a thin metallic sheet, resembling aluminum foil, separated the source from the environment and acted as an outrun window for the electrons. The range of the 0.039 MeV electrons emitted by the source is 1.45 $\times 10^{-3}$ cm in aluminum. Because this distance is less than the typical thickness of aluminum foil (3×10^{-3} cm) it is safe to assume that none of the low energy electrons escape the source container. The stopping power of aluminum for 1.77 MeV electrons is 4.06 MeV/cm so a reduction in energy of 0.01 MeV would occur as the electrons passed through the outrun window. A more likely value for the power output of the source, adjusted to account for the absorption of the source container, was then calculated to be

$$P_{^{106}Ru} = 1.76\frac{MeV}{d}10680\frac{d}{s} = 18797\frac{MeV}{s}. \tag{74}$$

Figure 31: ^{106}Ru source used for concept verification.

The source was placed directly against a 6.5 mm thick piece of plastic scintillator and a single convex lens was used to focus the image on the CCD (Fig. 32). Data acquisition and camera control was handled by an astronomy imaging package called MaxIm DL version 2.11 running on a Windows PC. The software was quite functional, allowing the user to set binning (see Sec. 2.3.2) and exposure time, and provided a readout of the temperature of

the CCD sensor. Images were saved as Flexible Image Transport System (FITS) files, a format that was developed by the National Aeronautics and Space Administration (NASA) to be a standard format for images and data structures in the astronomical community [Fac97].

Fig. 33 shows an image captured using the configuration described above. The camera was set to 2X2 binning and the exposure length was 120 seconds. These results demonstrated that the concept of monitoring beam profile using a CCD camera of this type was indeed valid.

3.2.4 Camera Selection

Choosing and purchasing the correct camera for the job were important steps in the project. There were a wide variety of companies that produced cameras of various quality and price and, in order to ensure that the proper camera was purchased, a comparison of several different products was performed.

At first, it seemed that a scientific grade CCD would be the best choice. There were some systems that offered single photon counting ability using an image intensifier coupled to a CCD. These cameras generally had extremely low dark currents due to excellent cooling and made use of fast electronics to allow for real time imaging. The quantum efficiencies of these cameras were extremely good, typically around 65% to 75%. All of the scientific grade cameras made use of 'grade 0' CCD sensors which were manufactured with the tightest quality assurance to prevent the occurrence of defective pixels.

Some of the prevalent suppliers of the scientific grade cameras included the Canadian Photonics Lab, Photonic Science Limited, Roper Scientific Photometric and the Cooke Imaging Corporation. A number of these companies were contacted and it was immediately apparent that the prices of the scientific grade cameras were too high. Intensified CCD systems were in the $50,000 to $70,000 range! Other, more moderately priced scientific grade cameras were priced around $30,000. These costs were clearly out of the range of expected project expenditures so attention was focused on the non-scientific grade imagers.

The next classification of cameras that were investigated were the industrial cameras. These are cameras developed for use in industry where the demand for sensitivity and performance is not as high as it is in research. Among the distributors of these types of camera are Cohu Inc., CCD Direct and Sony.

An investigation of the specifications of the industrial class cameras prompted caution. Rather than list the dark current of the camera the minimum illumination levels required were provided. This was unsatisfactory because the dark current was the parameter by which the system model results were to be compared. The costs of the industrial cameras investigated ranged between $3000 and $4000.

The last type of cameras that were considered were the astronomical class. CCD cameras have played a big role in amateur astronomy due to their sensitivity and relatively low cost,

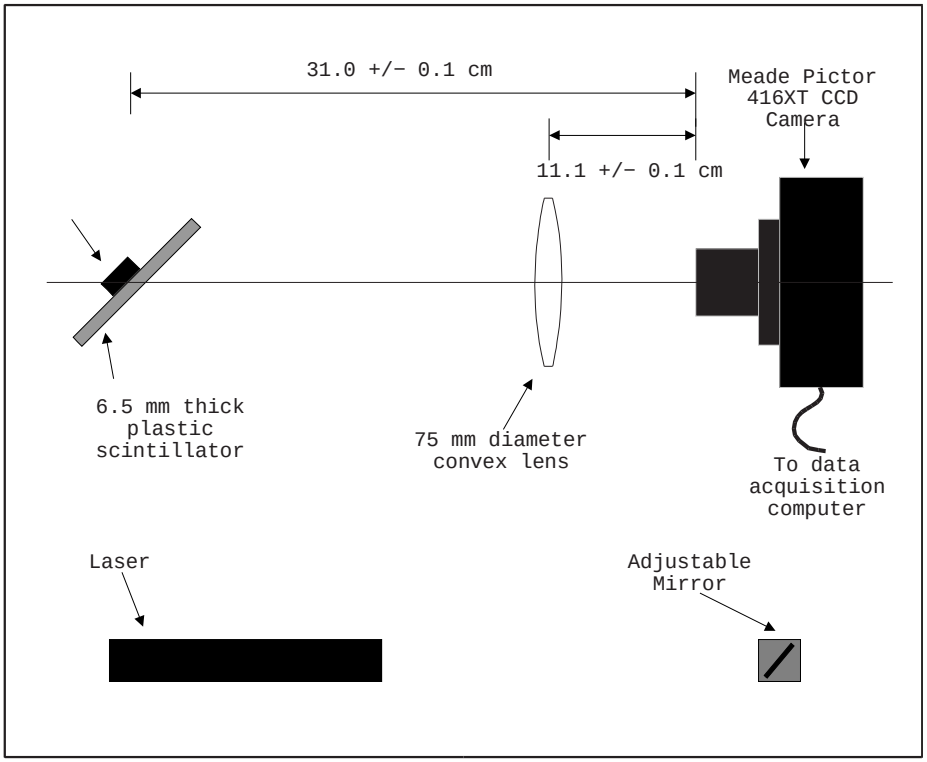

Figure 32: Experimental configuration used in concept verification. The laser was used to aid in camera alignment and focusing of the optical system.

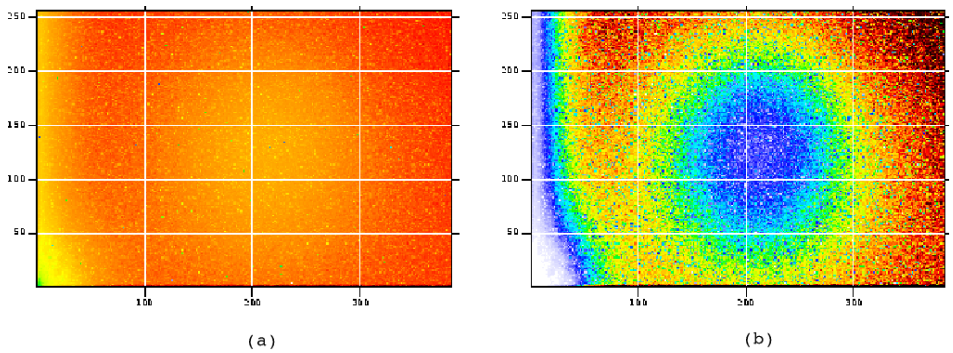

Figure 33: 120 second exposure of scintillator stimulated by ^{106}Ru source. Exposure (a) shows the image using a logarithmic colour scale and exposure (b) is processed with a histo-equalize algorithm that dramatizes the intensity variations.

and therefore, there has been a great amount of work put into their development. Some of the suppliers of astronomical CCD cameras are the Santa Barbara Instrument Group, Meade, Apogee and Starlight Express.

The concept verification, discussed in the previous section, was done using the Meade Pictor so it was already known that an astronomical CCD would suffice. The range of costs, encountered while investigating these cameras, was also encouraging. Although some of the high performance instruments were several thousand dollars, there were also products available that cost as low as $800. The performance levels of these cameras were quite good, even when compared to the scientific grade CCDs. Typical dark currents were around 1 e^-/pixel/s and quantum efficiencies were close to 40%.

The low cost of astronomical CCDs was due to that fact that they do not require a fast readout. Scientific CCDs are generally capable of reading several frames per second from the sensor. This puts a strain on the cooling requirements as constant operation generates much more heat in the sensor. A fast readout speed also requires much more expensive electronics. In the beam profiling application a fast readout was not needed, so the performance provided by astronomical CCD cameras was judged to be sufficient.

A breakdown of each of the CCD cameras investigated is shown in Table 2. The Starlight Express MX5 was the best choice when comparing the price and the dark current to the other cameras. Its weak point was its low number of pixels, which could limit the resolution of the beam profiling system and decrease the responsivity. However, the resolution requirement for the beam profiler was approximately 1 mm over a 65 mm beam diameter (only 65^2 pixels would cover requirements!) so the low number of pixels would not be a problem. The MX5 was selected as a suitable camera and ordered. Specifications on the camera and the CCD sensor can be found in Appendix C.

3.2.5 Data Acquisition and Camera Control System

To maximize the beam profiling systems' usefulness, the camera control and data acquisition system had to integrate completely with the hardware running the LUCID system in place at HIGS. This implied that the software controlling the camera had to be able to run under the Linux operating system. It also meant that there would have to be a low level command set for the CCD camera that could be executed by the LUCID data acquisition system.

The MX5 interfaces with a host PC through the universal serial bus (USB) as shown in Fig. 34. A Motorola 8051 embedded controller handles the high-speed command and data transfer between the electronics on the CCD and the PC. Power is supplied to the camera through a second connection to the USB controller.

The software that was provided with the camera was developed for the Windows operating system. To operate the camera under Linux, a kernel-level driver, complied for the specific Linux kernel version being run on the data acquisition PC, and a control application were needed.

Name	Type	Manufacturer	Pixels	Pixel Size (μm^2)	Dark Current (e^-/pixel/s)	Q.E. 425 nm (%)	Cost ($CDN)
SensiCam	S	Cooke Corp	307,200	98.01	0.1	40	35,985
Retiga Ex	S	QImaging	1,408,960	41.60	0.15	40	21,623
Series 300	S	Photometrics	262,144	576	0.55	70	18,000
CPL-18B	I	Canadian Photonics	199,500	—	—	—	7,500
ST-7XE	A	SBIG	390,150	81	1	20	4,043
4920	I	Cohu	437,664	70.19	—	—	3,330
M2C	I	CCD Direct	379,392	82.32	—	—	3,638
XCD-X700	I	Sony	786,432	39.06	—	—	3,142
MX5	A	Starlight Express	145,000	123.5	0.1	40	1,679
ST-5	A	SBIG	76,800	100	5	11	1,343

Table 2: Specifications and costs of several CCD cameras. The letters in the type column denote 'S'cientific, 'I'ndustrial and 'A'stronomical.

The necessary kernel drivers were provided by David Schmenk who has developed Linux software for a number of astronomy CCDs. They consisted of a high-level class driver that handled the general USB interface to the operating system and a low-level driver that handled the particular MX5 functions [Sch03]. These drivers were compiled and installed on a PC running Linux kernel 2.4.7-10.

A control application called Gnome CCD (GCCD), also written by David Schmenk, was installed to provide functional control of the camera through the Gnome graphical user interface [Sch03]. However, for control of the camera through the LUCID data acquisition system, a stand-alone command line interface was needed. By observing the source code for GCCD and the kernel drivers a suitable control application was written. This software, which was named simply 'Capture', was written to allow the user to specify the exposure time, output filename and number of pixels per bin on the command line. A dark frame and flat can also be specified, in which case the software will subtract the dark frame from the new exposure and then divide out the flat frame.

3.2.6 Optical Design

To develop the optical system, a process that utilized theory, simulation and experimentation was used. The specification of the optical system matrix was performed to provide a theoretical basis for the design. An optical simulation package called OpTaliX-LT was then used to generate possible configurations that would satisfy the theoretical constraints [Cor03]. To complete the design, suitable lenses were chosen and experimentation was used to get the best configuration.

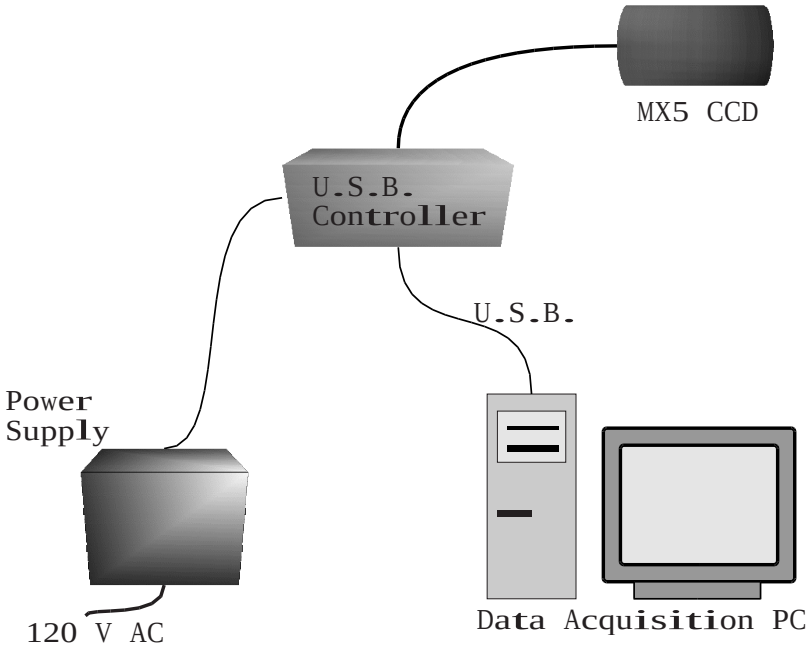

Figure 34: Data acquisition configuration.

The general form of the optical system matrix was given by Eq. 50. The required magnification,

$$\beta = \frac{h_{CCD}}{D_{beam}} = \frac{4.96 \text{ mm}}{64.0 \text{ mm}} = 0.0775, \tag{75}$$

was inserted producing

$$\begin{bmatrix} \alpha' \\ x' \end{bmatrix} = \begin{bmatrix} 12.9 & b \\ 0 & 0.0775 \end{bmatrix} \begin{bmatrix} \alpha \\ x \end{bmatrix}. \tag{76}$$

The paraxial constant, b, had to be expressed in terms of the geometry of the system using the relationship found in Eq. 54. Finding the incident ray angle, α, involved the size of the object, D_{beam}, and the EPD of the lens system as well as the distance between the first lens and the scintillator. Expressed mathematically, α became

$$\alpha = \tan^{-1}\left(\frac{\frac{EPD}{2} - \frac{D_{beam}}{2}}{l}\right), \tag{77}$$

where l was used to represent the distance between the scintillator and the first lens in the system. Similarly, the angle of the exiting ray was found to be

$$\alpha' = \tan^{-1}\left(\frac{R_{out} - \frac{h_{CCD}}{2}}{l'}\right) \tag{78}$$

where R_{out} is the radius of the final lens in the system and l' is the distance between this lens and the CCD sensor. The paraxial constant was then expressed as

$$b = \tan^{-1}\left(\frac{R_{out} - \frac{h_{CCD}}{2}}{l'}\right) - \left[(\tan^{-1}\left(\frac{\frac{EPD}{2} - \frac{D_{beam}}{2}}{l}\right)\right]\frac{1}{\beta} \tag{79}$$

and the system matrix became

$$[SYS] = \begin{bmatrix} 12.9 & \tan^{-1}\left(\frac{R_{out}-2.48mm}{l'}\right) - \left[\tan^{-1}\left(\frac{\frac{EPD}{2}-32.0mm}{l}\right)\right]12.9 \\ 0 & 0.0775 \end{bmatrix} \tag{80}$$

where the values for h_{CCD}, D_{beam} and β have been inserted. The values used to describe the system are illustrated in Fig. 35.

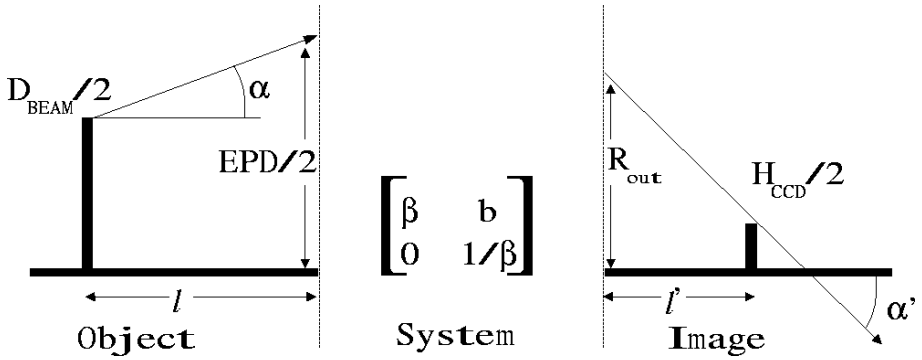

Figure 35: Diagram showing the optical system configuration.

The matrix relation in Eq. 80 describes the entire optics system, leaving the distances between the scintillator and first lens, l, the last lens and the CCD, l', and the EPD and radius of the last lens, R_{out}, as variables. Further development would now require that this system matrix be factored into lenses as in Eq. 57. This was done using the OpTaliX-LT software.

OpTaliX-LT allows the user to specify the radius of curvature, thickness, aperture, position and type of material of multiple lenses and then computes the magnification and image location for a given object. The EPD and focal lengths of the system are also computed. Alternatively, the magnification or EPD of the system can be specified and the location of any one of the object, image or lenses will be found to satisfy the constraints.

There were some general relationships that were quickly apparent from experimenting with OpTaliX-LT. Firstly, to provide the required magnification, within a reasonable overall length, several lenses would be needed. Secondly, the EPD of the system was limited by the magnification, complexity and size of the system.

A design, based on lenses available from an undergraduate physics lab at the University of Saskatchewan, was simulated by OpTaliX-LT. A graphical output from OpTaliX-LT is

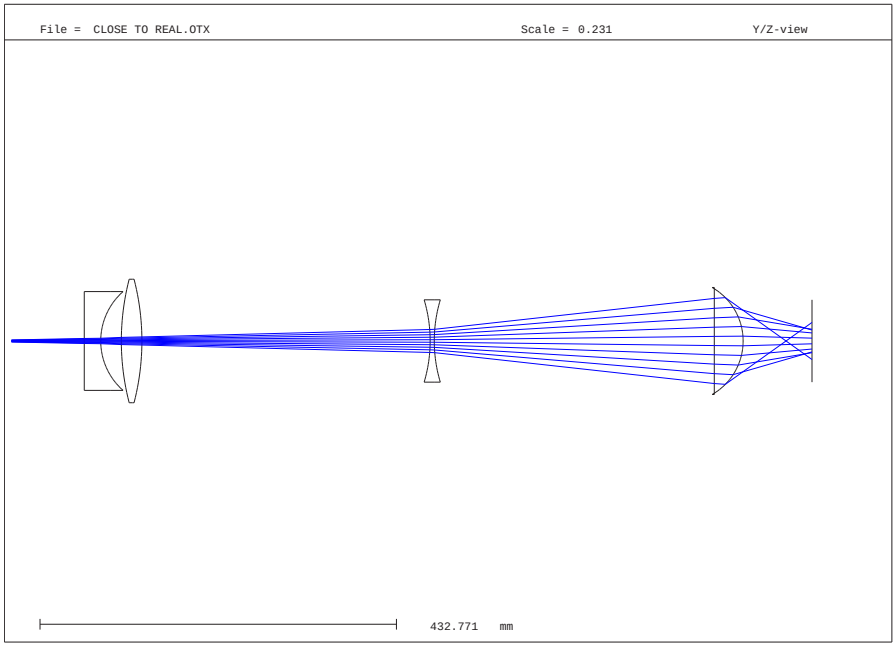

Figure 36: Lens configuration provided by OpTaliX-LT. The location of the object is 15 cm to the left of the first lens. The system has an overall length of 99 cm, an EPD of 1.75 cm and a magnification of -0.0775.

shown in Fig. 36 and Table 3 gives the specifications of the lenses and their spacing.

Now that a general configuration that satisfied the system constraints was available, experimentation was used to finalize the design. This was done in the lab using an optical rail, four lenses, a test pattern, a light emitting diode (LED) and the MX5 CCD camera. The lenses were positioned at the locations specified by the simulation and the LED was placed in the object location. In a dark room, the light from the LED was bright enough to be seen on the CCD sensor, and by manipulating the position of the lenses it could be focused into a tight spot. Final focusing was performed by imaging the LED with the CCD and observing the image quality. Then the test pattern was placed at the object location and the LED was positioned behind it to provide illumination. The test pattern was then imaged. Fig. 37 shows an image of the LED and an image of the test pattern and indicates that the optical system was configured properly.

3.2.7 Light-Tight Box Design

The final component of the apparatus that required design work was the light-tight box. A light-tight box was needed to encompass the scintillator, lenses and CCD in order to eliminate background illumination.

There were several factors that determined the overall size of the light tight enclosure. The box had to be large enough to contain the optical system and allow the gamma-ray beam to pass through at a 45^o angle. It also had to have enough space inside to allow for manipulation

Lens Number	Radius of Curvature (mm)	Distance from Object (mm)
Object	———	0
1	0.00 / 80	150
2	300 / -300	188
3	-175 / 175	550
4	0 / -75	890
Image	———	991

Table 3: Lens surface descriptions and locations as specified by OpTaliX-LT simulation software. The surfaces are specified by their radii (object side / image side).

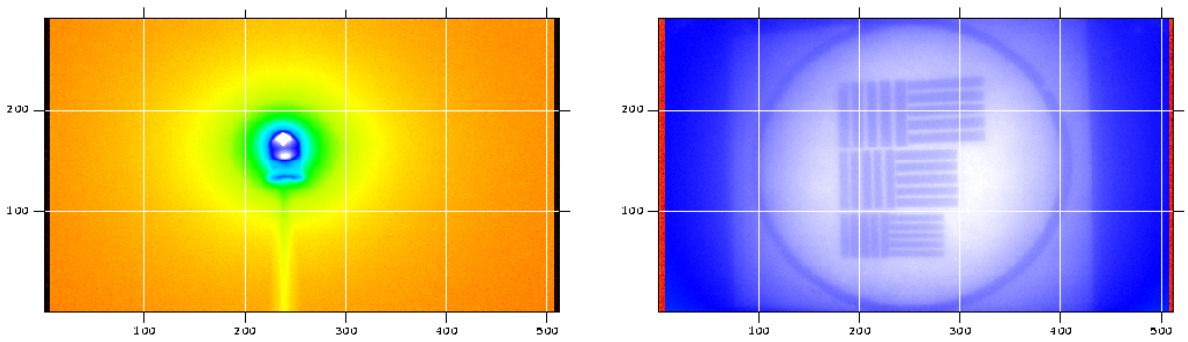

Figure 37: This image on the left is the LED and the test pattern is on the right. The actual test pattern is shown in Fig. 43.

of the lens system. Finally, the box dimensions had to be of sufficient size to accommodate possible small changes in the design. Dimensions of 45" x 8" x 12" for the length, width and height were chosen to satisfy these constraints.

A plan was developed using VariCAD. It consisted of a frame, made of 1/4" square aluminum bars, that rested on a 1/8" aluminum base. The sides and top of the box were 1/16" aluminum sheeting. In each side of the box, 15.75" x 5" holes were positioned to allow for the entrance and exit of the gamma-ray beam. A 1.57" diameter hole was designed into one end of the box to allow for placement of the CCD and a collar was added to hold the camera in place. The VariCAD design is shown in Fig. 38.

To ensure that the box would be light tight once it was constructed a number of steps were taken. Initially, the frame was designed so that the sides could be inlaid as in Fig. 39. Due to cost constraints, this idea was abandoned in favour of a simpler but less effective design using square aluminum bars. To minimize the possibility of light leaking into the box, the walls were designed to overlap where possible and a high density of screws were used. Aluminum foil was to be used to cover the gamma-ray beam entrance and exit holes. The total cost of the light-tight box was $1000 and was largely due to the labour involved

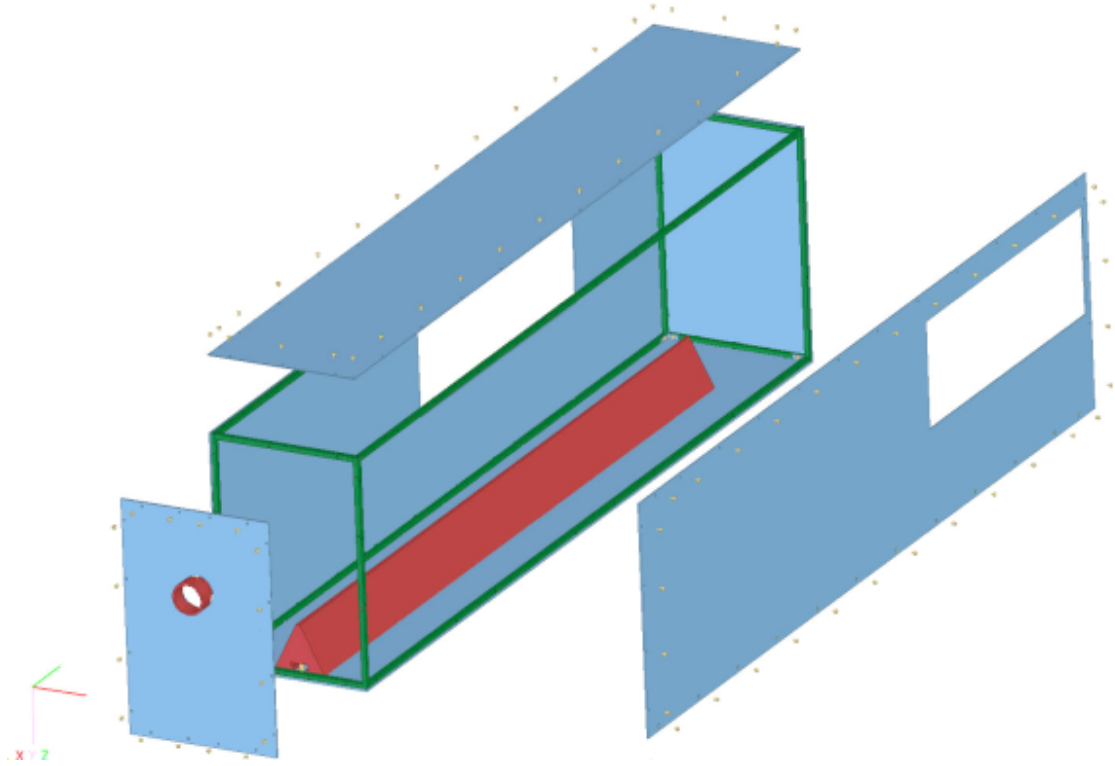

Figure 38: 3D drawing of the light tight box design.

in tapping all of the screw holes.

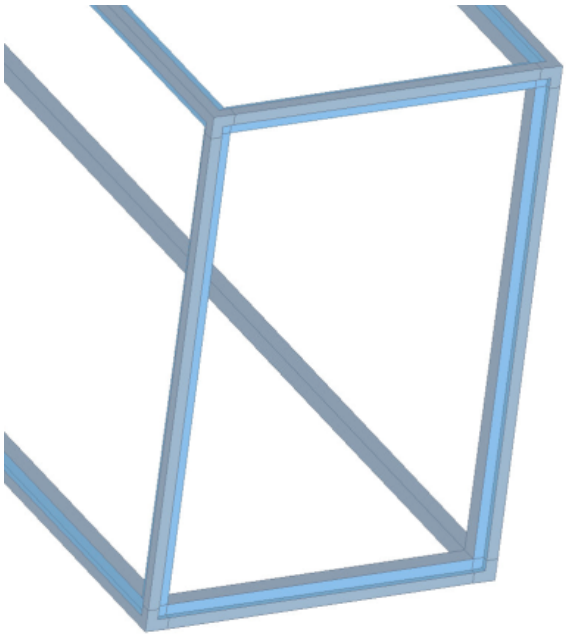

Figure 39: The original frame design for the box. An extra edge would prevent light from slipping through any cracks but it had to be left out due to high machining costs.

4 Testing

4.1 Light-Tight Box

Testing of the light-tight box was carried out to determine what effect the ambient room light had on the number of counts registered by the CCD during an exposure. This was done using a mobile, incandescent light source, and the CCD camera. The light source was placed in 18 different locations around the box and 5 second exposures were taken at each location. Two additional exposures were taken with the room lights on and off. Special attention was taken to illuminate all the edges and corners of the box as well as the aluminum foil covers.

The results of this test showed that the light tight box was far from 'light tight'. With the room lights on the camera registered a total of 3.70×10^8 counts versus 3.52×10^8 counts with the lights off, a difference of 1.83×10^6 counts or about 5%! The number of counts measured with the light source at different positions around the box varied from 3.53×10^8 counts to 3.91×10^8 counts indicating that there were specific places on the box that light was penetrating. With the light source placed directly in front of the aluminum covers the camera measured 3.53×10^8 counts.

To improve these results black electrical tape was used to cover all of the edges of the box. With the tape in place the total counts with the lights on and off only differed by 11024 counts. This corresponded to a 3×10^{-3}% difference and was considered acceptable.

4.2 CCD

In order to properly analyze the images taken with the CCD, the instrument's operational characteristics had to be determined. Testing was performed to measure the CCD's PRNU, FPN, dark current, responsivity, and time dependent behaviour.

4.2.1 PRNU and FPN

The PRNU of the sensor was measured by examining the variance and mean of the image data for exposures taken while the sensor was under uniform illumination. Finding the PRNU was important for determining the pattern noise contributions and ultimately for determining the uncertainty in the number of counts measured by the camera.

The condition of uniform illumination was created by placing semi-transparent, white plastic over the camera. A series of 100 images were taken and a Ftools program, called fimgstat, was used to examine the image statistics and extract the mean and standard deviation [Cen03]. The average PRNU, U_{PRNU}, was found to be 0.0168 ± 0.0002 using Eq. 45.

The FPN is the other component of pattern noise and needs to measured for proper error analysis. It was measured in the same manner as the PRNU except that the lens cap was placed on the camera to prevent light from reaching the sensor. U_{FPN} was found to be 0.00943 ± 0.0005.

The measured values for U_{PRNU} and U_{FPN} were quite small, indicating the pattern noise in the system will not be a limiting factor as far as the camera's sensitivity is concerned. Errors in U_{PRNU} and U_{FPN} were given as the standard deviation of the measured values.

4.2.2 Dark Current and Noise Floor

As mentioned in Sec. 2.3.4, the dark current of a CCD can be measured by taking exposures of varying time while the sensor is kept dark. The slope of the plot of the total number of electrons accumulated versus the exposure time is the CCD dark current in units of electrons per second. The y-intercept or this plot gives the minimum camera output or the noise floor in units of electrons.

The camera's lens cap was put in place to ensure no light could reach the sensor and exposures of increasing length were taken. Data acquisition was performed using a script and the Capture data acquisition software (see Sec. 3.2.5). 4x4 binning was used. Within the script, an analysis function, called fimgarith, was called to register the total number of electrons represented in the exposure [Cen03]. The number of electrons, n_d, was then placed in an output file with the exposure time in milliseconds[6]. Errors in the number of electrons were

[6]The number of electrons that corresponds to a given number of counts can be found by multiplying the number of counts by the full-well electron capacity of one bin, and then dividing by the maximum number of counts.

determined using

$$\delta n_d = \sqrt{n_e + U_{FPN}^2 n_e^2}. \tag{81}$$

Figure 40 shows the results of this experiment.

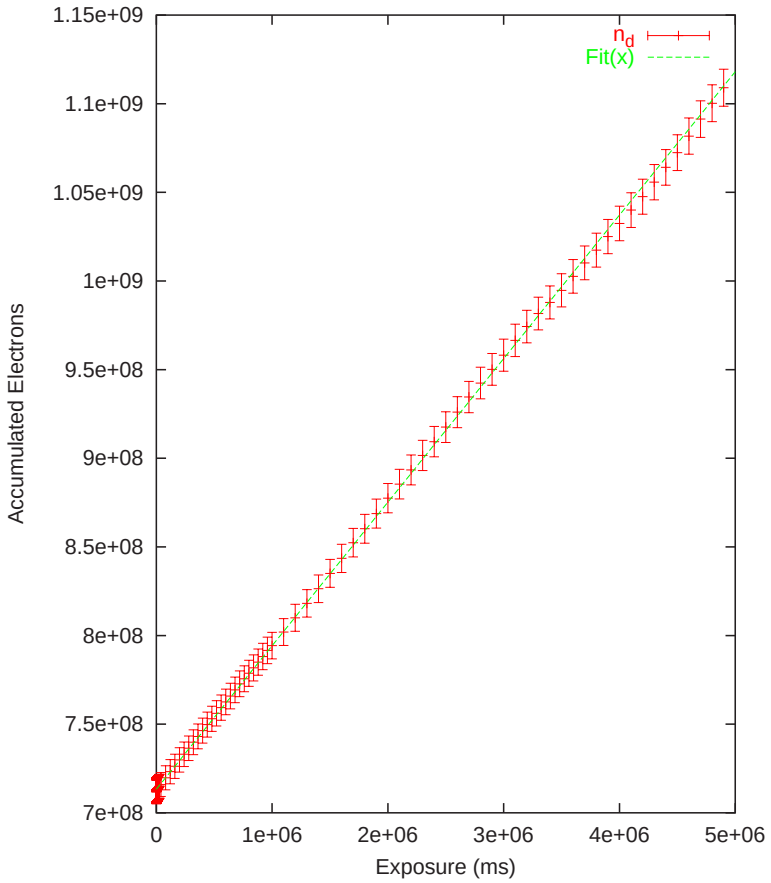

Figure 40: CCD output for varying exposure length under no illumination. The slope of this line represents the dark current of the camera and the y-intercept is the noise floor.

The data were fit to a straight line and the slope and y-intercept were extracted. The reduced χ^2 of the fit was computed to determine the goodness of the fit. The value of the dark current was measured to be $(80.96 \pm 0.04) \times 10^3$ electrons per second for the entire sensor. Dividing this by the number of bins in the image gives the dark current, i_{dark}, per bin in the sensor, which is the quantity needed to perform the error analysis:

$$i_{dark} = \frac{80.96\ e^-/s}{9000\ bins} = 9.000 \pm 0.004 \frac{e^-}{bin\ s}. \tag{82}$$

The y-intercept was found to be $(71257 \pm 3) \times 10^4$ electrons and represents the minimum

possible reading of the camera. The noise floor, n_{floor}, was determined by dividing this value by the number of bins, giving

$$n_{floor} = \frac{71257 \times 10^4\ e^-}{9000\ bins} = 79174 \pm 3\frac{e^-}{bin}. \tag{83}$$

The measured dark current and noise floor values were quite small but did not agree with the specifications. The measured dark current for 4x4 binning was $9.000 \pm 0.004\frac{e^-}{bin\ s}$ or $0.563 \pm 0.001\frac{e^-}{pixel\ s}$. The specified value was $0.1\frac{e^-}{pixel\ s}$; almost 6 times lower than the measured value! Despite the disagreement, the dark current still only contributed 2.80 counts per second or approximately $\frac{5}{1\times10^9}$ of the maximum possible counts. This means that to saturate the camera a dark exposure would have to be 56.1 hours long! The noise floor divided by the number of counts for saturation was 4.12×10^{-2}, or about 4% of the maximum.

4.2.3 Responsivity

The responsivity of the MX5, the rate at which it converts incident energy into photoelectrons, was measured using the technique described in Sec. 2.3.3. A plot of the number of accumulated photoelectrons versus the exposure time should yield a straight line with a slope equal to CCD's responsivity.

A LED was used to provide a constant radiant power on the sensor and exposures were taken of increasing time. The CCD was removed and an Ealing LIMS 920 photometer was put in its place to measure the radiant power density in units of $\frac{\mu W}{\mathrm{cm}^2}$. The power incident on the CCD was found by multiplying the output of the photometer by the area of the detector of 0.298 cm^2. Once again, data acquisition was performed using the Capture program and a shell script which allowed for remote operation and automation. Exposures were taken between 10 and 10000 ms at 10 ms intervals at a radiant power density of $0.020 \pm 0.002\frac{\mu W}{cm^2}$. The results are shown in Fig. 41.

Fitting the linear portion of the relationship produced a line with a slope of $2317370 \pm 785\ e^-/s$. Thus, the responsivity of the sensor was

$$r_{CCD} = \frac{2317370 e^-/s}{0.020\frac{\mu W}{cm^2}0.298 cm^2} = (3.88 \pm 0.02) \times 10^8 e^-/J. \tag{84}$$

This result provided a link between the number of photoelectrons counted in an exposure and the power incident on the sensor.

4.2.4 Time-Dependent Behaviour

Some care was taken to examine the CCD output as a function of the length of time since it was powered up. This analysis was done because of the close relationship between the sensor output and its temperature which was controlled by a thermoelectric cooler. The goal of this test was to determine the amount of time required for the sensor to reach an

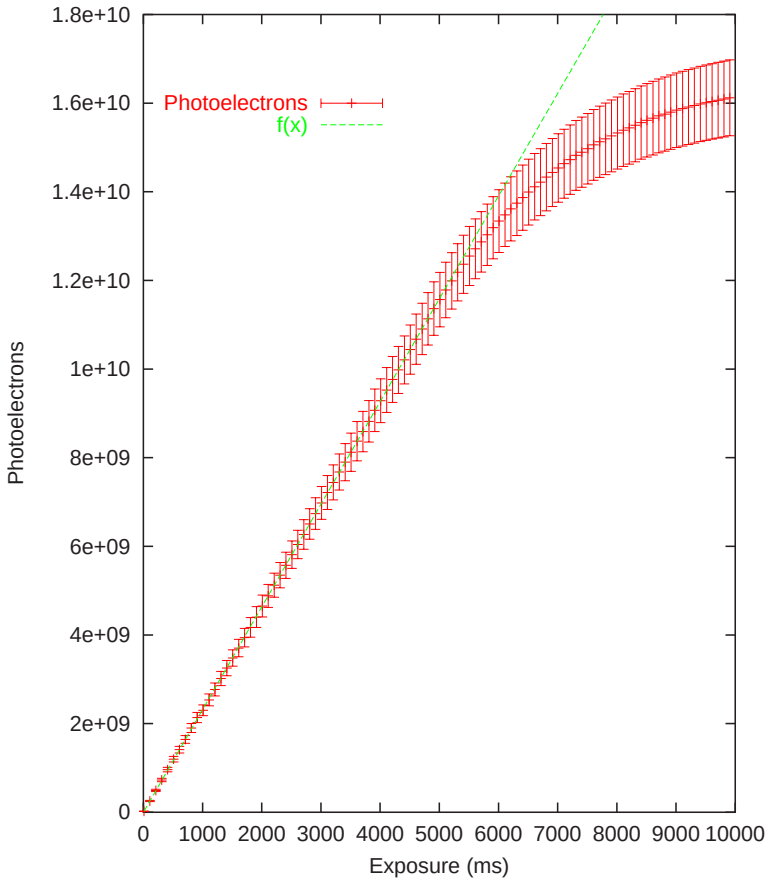

Figure 41: CCD output for varying exposure length under constant illumination. Slope of linear region represents the cameras responsivity multiplied by the radiant incidence on the sensor.

acceptable operating temperature and to see if there was some time after which the sensor's performance began to deteriorate.

The experimental configuration for this test was identical to the configuration used in the dark current measurement. A shell script was used to implement the Capture software which was set to take 3600 one second exposures. The script recorded the number of the exposure, the time since the script was run and the total counts in the exposure in an output file. The script was started 5 seconds after the camera was plugged in.

The data accumulated are shown in Fig. 42. It shows the CCD output reaching a minimum at around 200 seconds then slowly increasing and leveling off. This indicated that the thermoelectric cooling system has to be allowed to operate for around 100 to 200 seconds before beam profiles are acquired. Despite the increase in output for times greater than 200 seconds there doesn't seem to be any problem with operating the camera indefinitely because the increase is only 0.2% over 900 seconds.

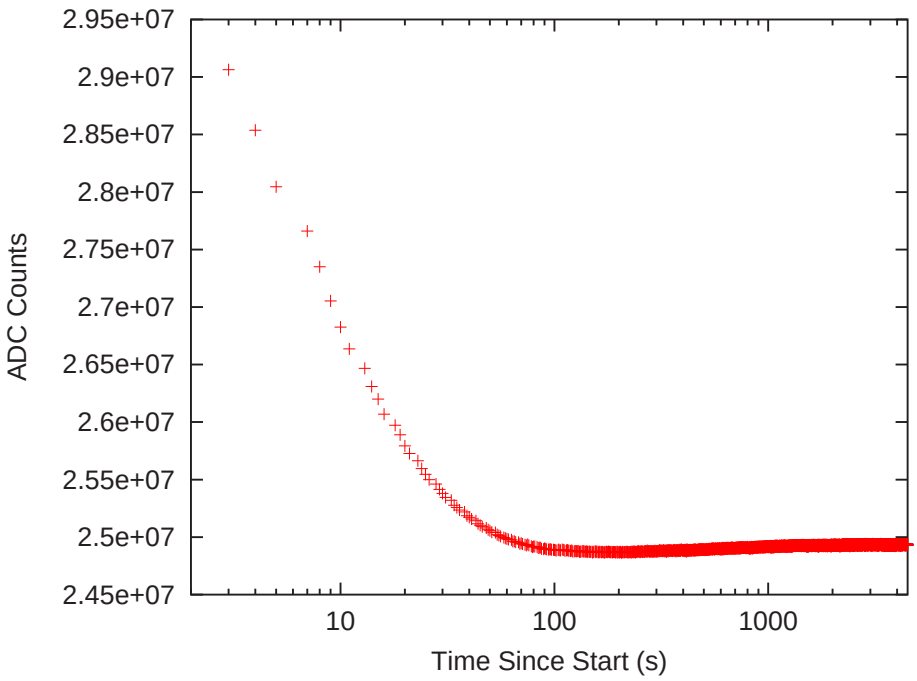

Figure 42: Plot of the total CCD output versus the time since startup. Note that the time scale is logarithmic.

4.3 Optics

The optical system was tested to measure the spacial resolution and magnification. These properties needed to be known to facilitate data analysis. The measurements were taken by imaging an optical test pattern and comparing the image to the actual object. Profiles of the image were also constructed to test the systems ability to resolve detail.

4.3.1 Resolution

In Sec. 3.2.6 the procedure used to focus the optical system was described. Using the image of the test pattern obtained at that time (see Fig. 37), the resolution of the optical system was found by measuring the distance between several key points on the actual test pattern and dividing them by the number of bins between the same two points on the image. Figure 43 shows the test pattern and image used and the location of the measurements made. The measurement data, along with the resolution data, are displayed in Table 4.

There were two complications encountered in the measurement of the resolution of the optical system. The first was that each potential well in the MX5 is 9.8 μm wide and 12.6 μm in height, rather than square, but is represented by a square bin in the image, implying that separate resolutions for the horizontal and vertical components were needed. The second was that the scintillator was placed at an angle with the right side closer to the lenses than the left which introduced a gradient into both the horizontal and vertical resolutions. These two problems required special attention.

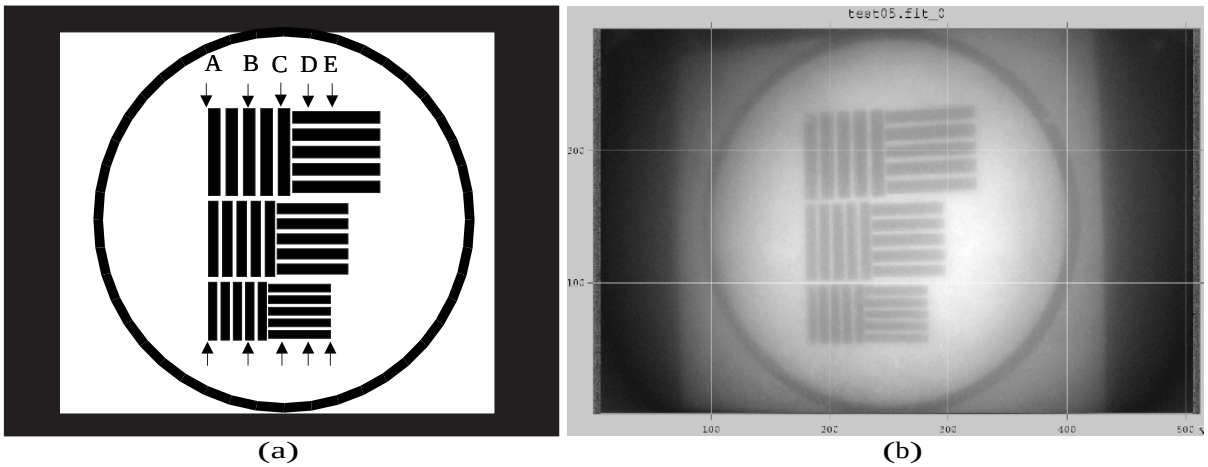

Figure 43: The test pattern used in the optical parameter testing. The object is shown in (a) and the image is shown in (b). The letters A to E and the arrows in (a) were added after the image was created to indicate where measurements were made.

	Position ± 0.005 cm	Object ± 0.005 cm	Image ± 1 pixel	Resolution cm/pixel	±
A	2.500	4.030	173	0.0233	0.0002
B	3.235	4.030	176	0.0229	0.0002
C	3.745	3.990	176	0.0227	0.0002
D	4.260	3.950	176	0.0224	0.0002
E	4.645	3.950	177	0.0223	0.0002

Table 4: Measurement of the test pattern dimensions, on both the object and image, as indicated in Fig. 43. The positions are measured from the solid black area on the left of the pattern.

The reason that the scintillator was placed with its normal axis at an angle to the optical axis was to ensure that a test source could be placed symmetrically with respect to the scintillator (as to provide evenly distributed gamma flux), without the unshielded radiation being directed at the CCD. The effects of this configuration were apparent from the resolutions seen in Table 4, with decreasing resolution occurring from measurement A to E.

A function that described the vertical resolution, $R_V(x)$, at any horizontal location, x, in the plane of the test pattern was constructed from the measurement data. By plotting the calculated resolution against the location of the measurement, as in Fig. 44, a linear function

$$R_V(x) = \frac{4.74 \times 10^{-4}}{pixel} x + 0.0227 \frac{cm}{pixel} \tag{85}$$

was generated. Here, positions are measured from measurement C. Using the ratio of horizontal and vertical pixel dimensions, the relationship was modified to give the horizontal

resolution

$$R_H(x) = \frac{9.8\mu m}{12.6\mu m} R_V(x) = \frac{3.69 \times 10^{-4}}{pixel} x + 0.0177 \frac{cm}{pixel}. \quad (86)$$

A simple qualitative test of the systems ability to resolve detail was performed by looking at cross sections of the vertical bars in the image of the test pattern. By examining the relative height of the troughs and peaks in the cross sections, and knowing the spacing between the bars, the level of detail attainable can be measured.

Cross sections were created using the Ftools package. Figure 45 a, b and c correspond to the top, middle and bottom groups of bars. In the top group the bars were 2.20 mm wide with 1.00 mm of white space between them, the middle bars were 1.90 mm wide with 0.75 mm spaces and the bottom bars were 1.60 mm wide with 0.50 mm spaces. A rough measurement of the peak to trough intensity difference gave a magnitude of 1650 for the top group, 1600 for the middle group and 1100 for the bottom group.

The results of the resolution tests showed a gradient resolution that was different for the horizontal and vertical directions, but also showed that the system will be capable of imaging at sub-millimeter resolutions.

4.3.2 Magnification

To measure the actual magnification provided by the system, the test pattern and its image, as shown in Fig. 43, were employed once again. The value of the magnification was calculated as the ratio of the CCD sensor height and the size of the object that fit, vertically, onto the sensor.

When the test pattern was designed, a circle with roughly the same diameter as the maximum expected beam diameter was added to aid in measuring the magnification. By looking at the image it is clear that almost all of this circle fits onto the image. A measurement of the extent of the the test pattern that fit, vertically, onto the sensor was 65.6 $\pm$ 0.1 mm. Dividing the height of the sensor, 4.96 mm, by this value gave the magnification of the system:

$$\beta = \frac{4.96mm}{65.6 \pm 0.1mm} = 0.0756 \pm 0.0001. \quad (87)$$

This value is close to the design value of 0.0775 that was calculated in Sec. 3.2.6.

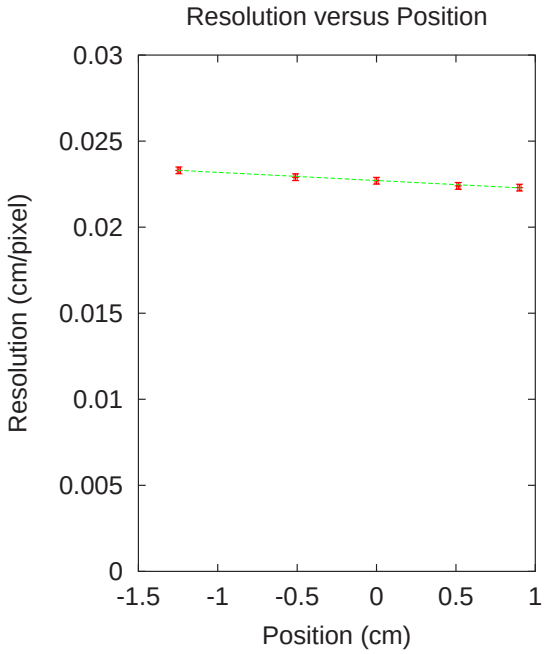

Figure 44: The relationship between horizontal position along the plane of the test pattern and the resolution of the image. The straight line is the linear fit of the data. The slope of the function was $(-4.74 \pm 0.24) \times 10^{-4}/pixel$ and the y-intercept was $(2.27 \pm 0.01) \times 10^{-2} \frac{cm}{pixel}$.

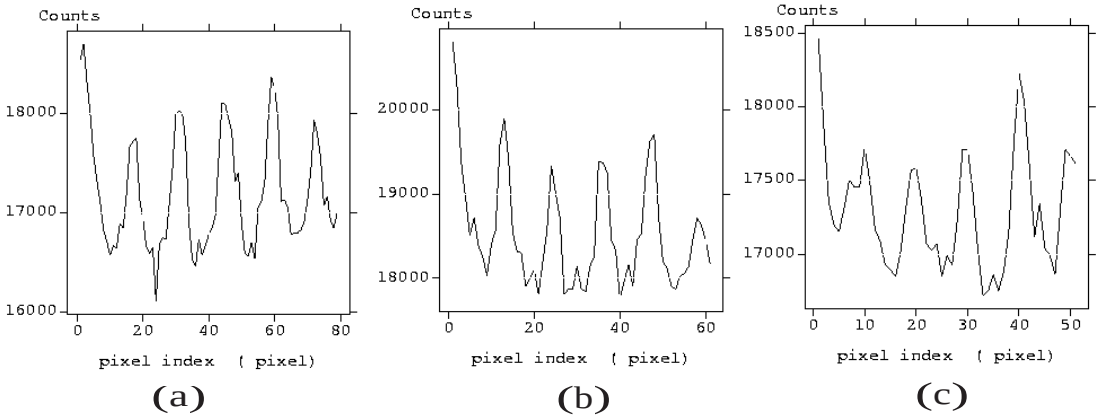

Figure 45: Cross sections of the three groups of vertical bars in the image of the test pattern. (a) is the top, (b) the middle and (c) the bottom set. The peaks represent the white areas and the troughs are the black bars.

4.4 Source Testing

Testing the CCD-based beam profile monitor with a radioactive source was the final objective of this project. Ideally, the system would have been tested at HIGS, but since the facility was unavailable for much of the duration of this project, source testing had to suffice. The main goals of this test were to examine the performance of the data acquisition system, to solidify and test a data analysis scheme and to measure the system responsivity.

4.4.1 Source

The source used to test the beam profile monitor was a 24.5 mCi ^{137}Cs source normally used for undergraduate Compton scattering experiments. It was selected because of it was the most active gamma-ray source available. A measurement of the source intensity and emission spectrum were taken with a sodium iodide detector and the source activity was determined to facilitate the calibration of the monitor. A calculation of the dose rate given off by this source can be found in Appendix A.

^{137}Cs decays to ^{137}Ba through the emission of either a 0.514 or 1.176 MeV internal conversion electron. The decay leaves the ^{137}Ba nucleus in an excited state that results in the emission of a 662 keV gamma-ray 85% of the time [Hag02]. Atomic transitions within the ^{137}Ba result in the emission of 32 keV X-rays. The nuclear level diagram for the decay process is shown in Fig. 46.

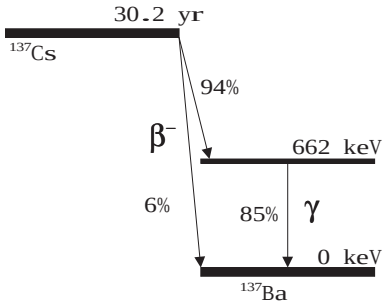

Figure 46: Nuclear energy level diagram for ^{137}Cs.

The emission spectrum of the source was obtained using a PC-based acquisition system called Maestro. An acquisition card, installed in one of the PC's peripheral component interconnect (PCI) slots, digitized the output of a 4 inch diameter, 5 inch long, Bicron 4M5/5 NaI cylindrical detector after it was amplified by an Ortec 571 nuclear instrumentation module(NIM). The spectrum is displayed in Fig. 47 which clearly shows the 662 keV photo peak at around channel 1200. The other features in the spectrum are the Compton edge around channel 800, the backscattering peak around channel 400 and the sharp X-ray peak near channel 400.

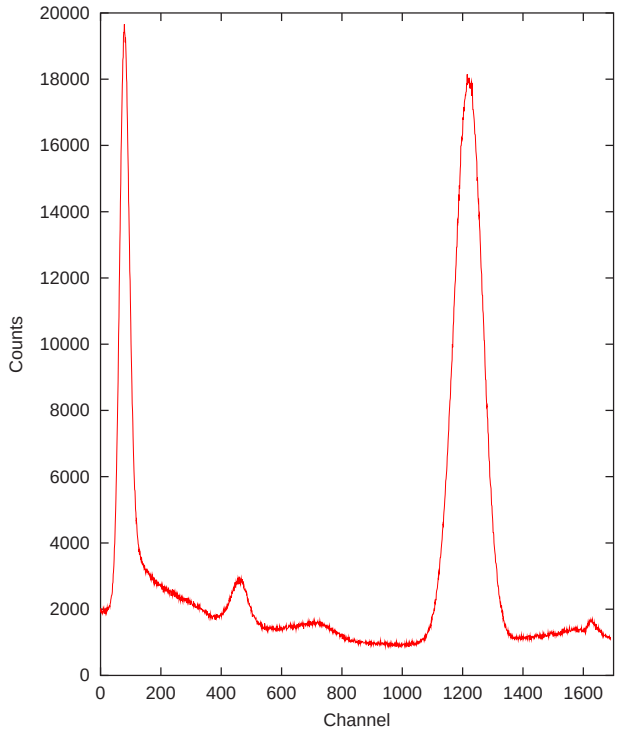

Figure 47: ^{137}Cs emission spectrum.

The source was contained inside a lead brick that was 17.6 cm in height, 6.4 cm wide and 10 cm deep (see Fig. 48). A small collimator, 0.5 mm in diameter, as well as a 2.5 mm diameter access hole provided outrun avenues for the gamma-rays. To maximize the intensity of radiation incident on the scintillator the larger access hole was used as the primary outrun route. The internal features of the source container could not be measured and no documentation could be found that described the container's interior.

Measurements of the gamma-ray flux from the source were made using the Bicron 4M5/5 NaI detector operating with a 1250 V bias provided by a Hamner Model N401 power supply. The output of the detector was amplified and then fed into a discriminator that emits a NIM logic signal every time it receives a detector signal larger than a preset threshold value. These logic signals were then patched into a ratemeter. Threshold values were monitored using an oscilloscope. The experimental configuration can be seen in Fig. 49.

To get a good measurement of the source intensity the detectors dead time had to be kept low. This was achieved by separating the source and the detector and re-collimating the gamma-rays. To ensure that the dead time of the detector was not going to play a factor, the count rates for the ^{137}Cs source and a ^{22}Na source were measured separately, and their sum was compared to the count rate obtained for both sources when measured together. If there was any dead time in the system, the combined rate would be lower then the sum of the individual rates.

With the detector threshold set at 240 keV, the ^{137}Cs rate was measured to be 8.5×10^4/s and

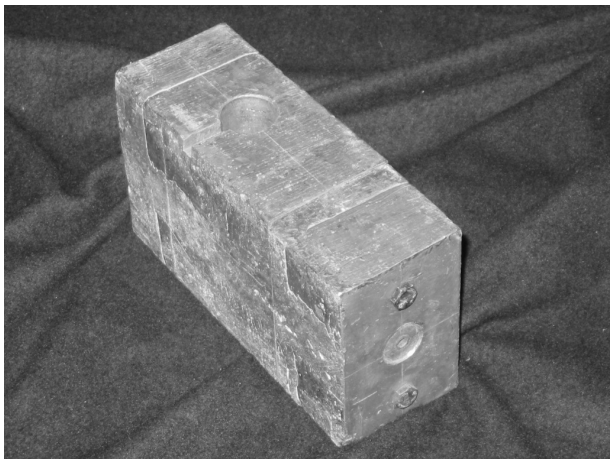

Figure 48: The lead source container.

the ^{22}Na rate was 1.2×10^4/s. The rate measured for both sources combined was 9.5×10^4/s. Subtracting the combined rate from the sum of the individual rates, and dividing by the combined rate, gave the dead time of the system:

$$\frac{(8.5 \times 10^4/s + 1.2 \times 10^4/s) - 9.5 \times 10^4/s}{9.5 \times 10^4/s} = 2.1 \pm 0.1\%. \quad (88)$$

Adjusting the measured ^{137}Cs count rate for the dead time produced a rate of $(8.7 \pm 0.6) \times 10^4$/s. This is the rate that was used to perform the beam profile monitor calibration.

4.4.2 Images

Images of the source irradiated scintillator were acquired over a period of several months over which time adjustments were made to the experimental configuration in order to improve the quality of the data. The first images obtained showed that the concept had merit but there were unexplained features in the data. Over time the problems were isolated and some small changes to the apparatus were made that had the desired effect on the data.

The configuration used for the image acquisition at the onset of testing consisted of the light tight box, 6 mm thick piece of BC 400 scintillator, 3μm thick aluminum converter, lens system, CCD camera, laptop computer and the source. Initially, the source was positioned as close to the scintillator as possible as to provide the maximum intensity of gamma-rays possible. Using this configuration, the image in Fig. 50 (a) was obtained.

The obvious features in the image were at once both promising and disturbing. The clear circular shape indicated that the system was able to record the source profile. Noise in the data drowned out the peak in the 2D histogram, but that would likely be fixed with data analysis. What was of real concern was the slight increase in intensity on the far right side and top left corner of the image. These abnormalities were, at first, unexplainable.

Over time, two modifications were made to the apparatus that removed the increase in

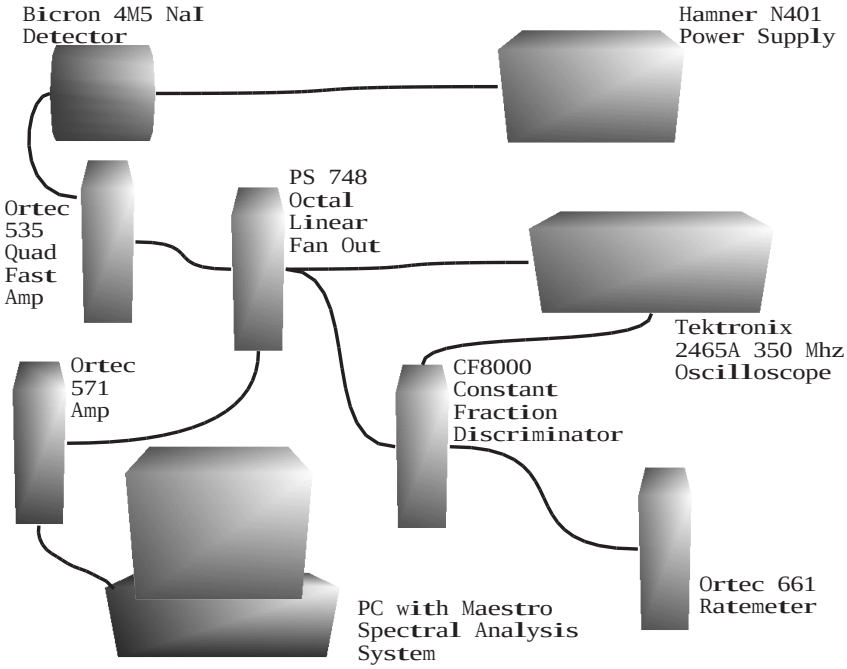

Figure 49: Experimental configuration used to measure source intensity.

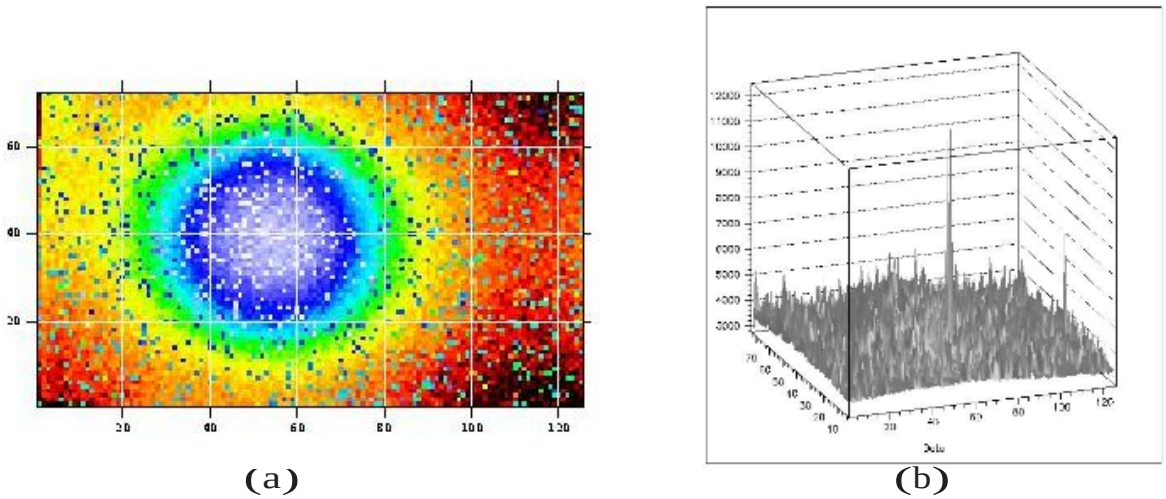

Figure 50: (a)One of the first images obtained of the source irradiated scintillator. (b) 2D histogram of image data.

intensity on the right of the image. First, a mask was placed around the lens closest to the object. This prevented any illumination from reflecting off the sides of the light tight enclosure and onto the CCD. Secondly, black tape was placed over the back and around the edges of the scintillator to prevent any light from reflecting off the aluminum converter. With these modifications the image in Fig. 51 was produced.

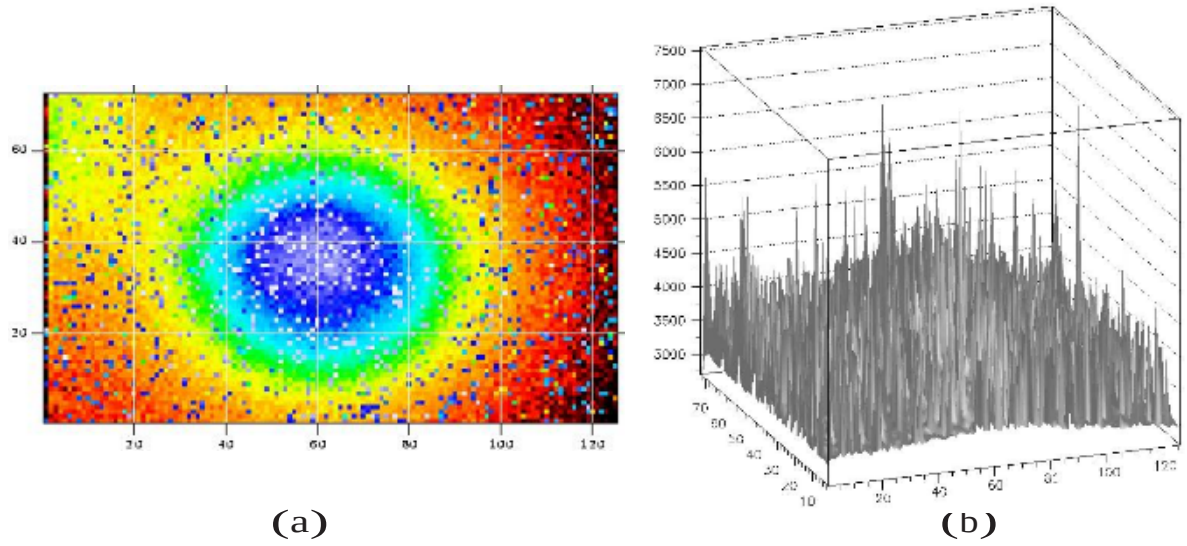

Figure 51: (a) Image produced with lens mask in place and scintillator back and edges taped. (b) 2D histogram of data.

The changes to the apparatus proved to be effective at improving the image quality. Further improvements were achieved through data processing, as described in the following section.

4.4.3 Data Processing

Each image, once acquired, had to be processed in order to reduce the noise introduced by the CCD and improve visualization. This was done through dark frame subtraction and bad pixel removal. To automate the processing, custom software was written. Using this software the quality of the images was dramatically improved.

The Capture program, used to acquire the data, outputs the data in FITS format. As mentioned in Sec. 3.2.3, FITS is the standard astronomical data format and can be used to store multidimensional scientific data sets. To read and write FITS files a library of C subroutines called CFITSIO was used. This library facilitated the development of the data processing program which was called Fixdata.

Upon execution, Fixdata performs a dark frame subtraction using an image and a dark frame passed to the program as command line arguments. This removes the contribution the dark current makes in the image. The effect of the dark frame subtraction on the image

in Fig. 51 is shown in Fig. 52 along with the dark frame used.

The result of the dark frame subtraction is an incredible decrease in noise as can be seen by comparing Fig. 51(b) and Fig. 52(d). Most of the speckles or spikes have been cleared up leaving a much more pronounced shape in the histogram. However, some of the spikes were not removed and frequently a dark frame has a spike at a location where there is no spike in the image causing a negative spike in the dark frame subtracted image.

Once the dark frame is removed Fixdata performs errant or bad pixel removal. In this step of the processing, pixel values are compared to the average value of the neighboring pixels and removed if they are not in agreement. The user specifies the number of standard deviations from the average value that is acceptable by passing a double precision number as a command line argument.

The process used to remove the bad pixels uses two passes through the data to ensure that no valid pixel data is compromised. In the first pass, an array, with dimensions equal to those of the image, is filled with a 1 or a 0 indicating whether or not the value of each pixel agrees with the average value of the pixels that surround it, within the user specified number of standard deviations. Then, in the second pass, the array created in the first pass is referenced so that only pixels that show agreement are used to generate surrounding pixel averages. This average value is compared with its corresponding pixel value and if it is not in agreement, again, within the user specified number of standard deviations, the pixel is considered bad. Thus, the possibility of removing valid pixel data, because the average of the surrounding pixels is based on one or more bad pixels, is greatly reduced.

When a bad pixel is found its value is replaced by the average value of the surrounding pixels as calculated in the second pass. However, that pixel cannot be included in any further calculations because its value is interpolated rather than measured. To monitor which pixels have been adjusted, Fixdata outputs a file that includes the location, original value and interpolated value of all bad pixels. The entire bad pixel removal process is summarized as a flowchart in Fig. 53.

Figure 54 shows the result of the image processing. 329 pixels were removed by the processing using 3 standard deviations as the acceptance parameter. The image contains a total of 4855989 counts over 9000 pixels with a maximum of around 1600 counts per pixel and a minimum of around 150 counts per pixel.

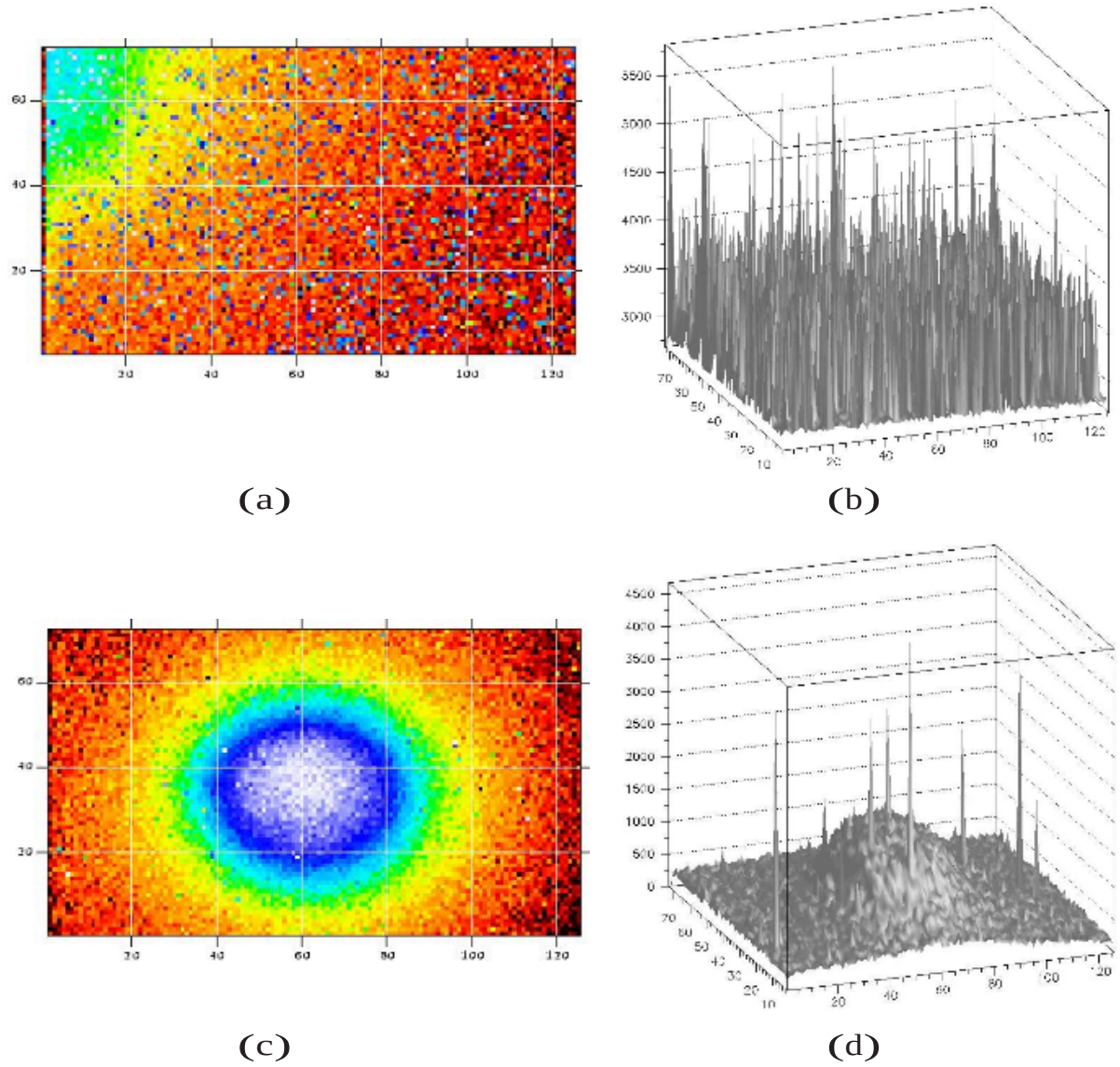

Figure 52: (a) Dark frame, (b) 2D histogram of dark frame data, (c) dark frame subtracted image and (d) 2D histogram of dark frame subtracted image data.

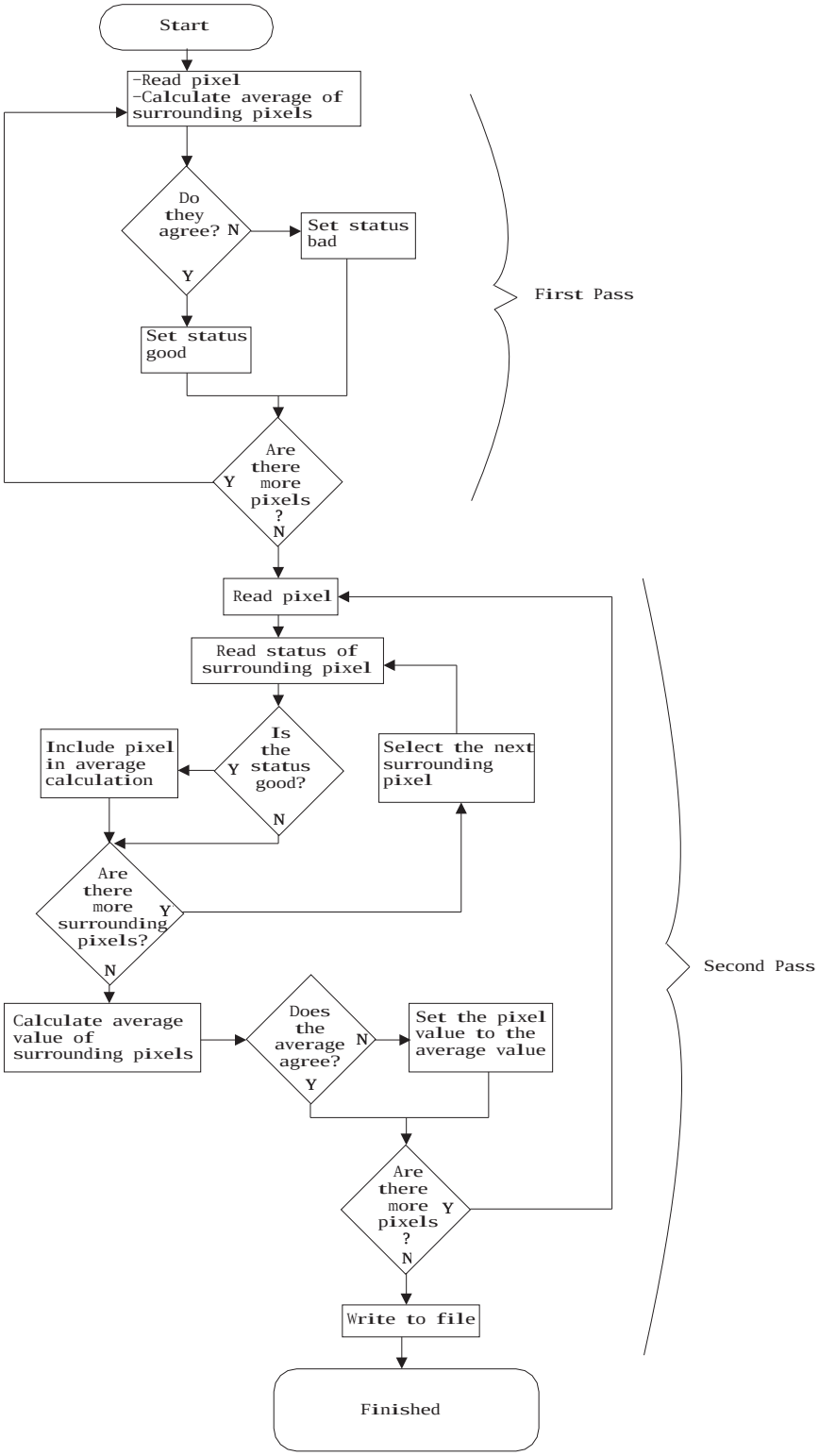

Figure 53: Flow chart of the image processing algorithm used to remove bad pixels.

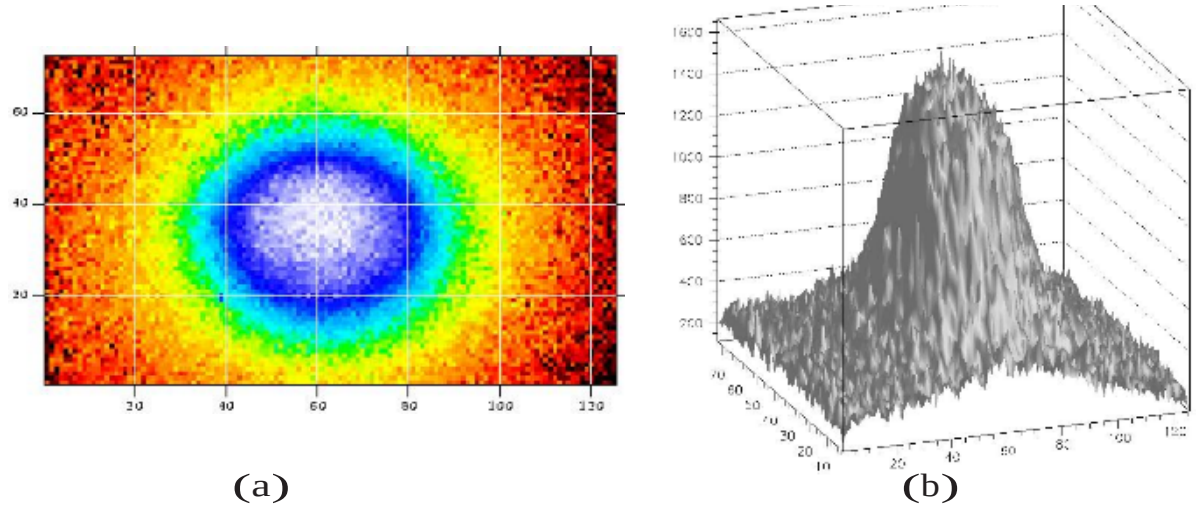

Figure 54: (a)Image of source illuminated scintillator with dark frame subtracted and bad pixels removed. (b) 2D histogram of image data.

4.4.4 Calibration

Source tests proved that the monitor provides an output, in the form of an image, that contains a number of counts that is proportional to the power absorbed by the scintillator, $P_{absorbed}$, and the exposure time, t_{INT}. The purpose of the calibration was to relate these quantities through the system responsivity, R_{SYS}. This was performed using data from the images taken of the ^{137}Cs source and GEANT energy deposition simulations.

To determine the power absorbed in the scintillator by the gamma-rays emitted from the source, the gamma-ray flux, Γ, needed to be calculated from the count rate measured in Sec. 4.4.1. This was done by employing a GEANT simulation of the experimental configuration used in the count rate measurement, as seen in Fig. 55. The simulation incorporated the detector threshold setting of 240 keV so that every time a gamma-ray deposited more than this energy in the NaI crystal, a count was registered. The measured count rate was 8.7×10^4/s and the number of gamma-rays detected in the simulation was 5.19×10^5 out of 10^8 generated. To speed up the simulation only 5% of the solid angle of 4π steradians was used. Then the flux of the 662 keV gamma-rays needed to simulate the source was calculated:

$$\Gamma = 10^8 \times \frac{8.7 \times 10^4/s}{5.19 \times 10^5} \frac{1}{0.05} = (3.4 \pm 0.2) \times 10^8/s. \tag{89}$$

With the activity of the source established, another simulation, this time of the configuration used to obtain the images, was generated to find $P_{absorbed}$. The simulation recorded the power absorbed in a 1 cm radius circular region at the center of the scintillator. The central region was investigated, rather than the entire scintillator, because of the lack of information on the interior geometry of the source container. Simulated power absorption

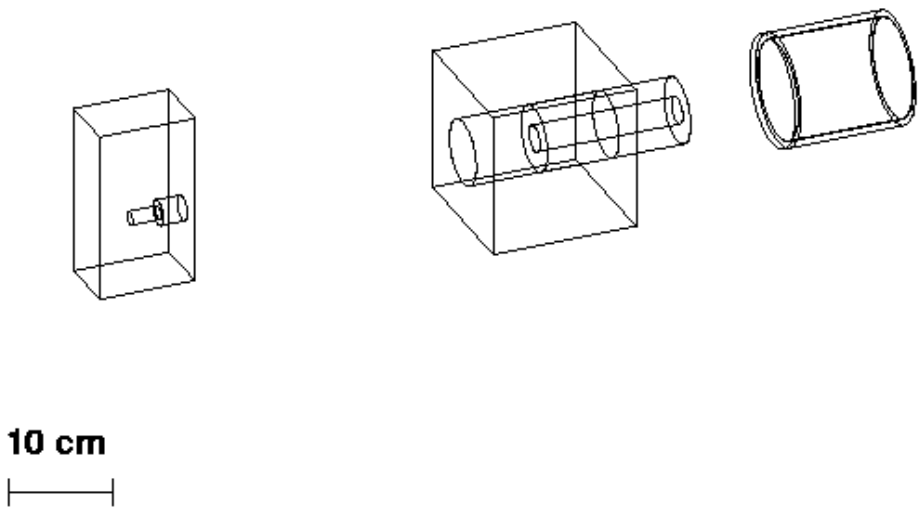

Figure 55: The configuration of the GEANT simulation used for source intensity measurements.

values for the entire scintillator were highly dependent on the source container geometry making them quite ambiguous. Values obtained for the power absorption in the central region were not dependent on the container geometry because the source had a 'clear view' of this portion of the scintillator. The value of $P_{absorbed}$ for the central region was 6.97 ± 0.46 GeV/s.

The scintillation that occurs due to the power absorbed in the central region of the scintillator is partially projected onto the center of the CCD sensor. The optical system magnifies this region by 0.0756 times, as was determined in Sec. 4.3, so that the corresponding image on the CCD is a 756 μm radius circle. The sensors horizontal and vertical bin densities, d_H and d_V, were calculated from the width, W_{CCD}, and height, H_{CCD} of the sensor and the number of bins in the rows, n_{row}, and columns, n_{col}. The bin densities for 4x4 binning were found to be

$$d_H = \frac{W_{CCD}}{n_{row}} = \frac{6.00mm}{125\ bins} = 48\frac{\mu m}{bin} \tag{90}$$

and

$$d_V = \frac{H_{CCD}}{n_{col}} = \frac{4.96mm}{72\ bins} = 69\frac{\mu m}{bin}. \tag{91}$$

Dividing the radius of the image by each bin density gives

$$H = \frac{1}{2}\frac{756\mu m}{48\frac{\mu m}{m}} = 7.88\ bins, \tag{92}$$

and

$$V = \frac{1}{2}\frac{756\mu m}{69\frac{\mu m}{m}} = 5.48\ bins, \tag{93}$$

where H and V represent the parameters of an ellipse that describes the shape of the illumination, from the central 1 cm region of the scintillator, in units of bins. An image analysis program was written to compute the number of counts that were contained within the ellipse described by

$$\frac{x^2}{H^2} + \frac{y^2}{V^2} = 1, \tag{94}$$

and the error associated with this number of counts. This procedure was performed on a 15 minute source exposure and a 15 minute dark exposure, producing a source count, N_{Source}, of 2392400 ± 1239 counts and a dark count, N_{Dark}, of 1605008 ± 861 counts. The details of the error analysis can be found in Appendix B. Both exposures were taken with the camera set to 4x4 binning. N_{Dark} was subtracted from N_{Source} to give the number of counts incurred as a result of the source:

$$N_C = N_{Source} - N_{Dark} = 787392 \pm 1509. \tag{95}$$

With the power absorbed and the resulting number of counts determined, the system responsivity, R_{SYS}, was found using Eq. 67:

$$\begin{aligned} R_{SYS} &= \frac{N_C}{P_{absorbed}\, t_{INT}} \\ &= \frac{787392}{6.97 GeV/s\ 900s} = 126 \pm 8\ Counts/GeV. \end{aligned} \tag{96}$$

This value, which was found using a combination of measured parameters and simulation results, brought the project into focus. It provided a means by which the camera response could be theoretically modeled for a given gamma-ray beam energy and flux, allowing for an evaluation of the monitor's overall performance.

5 Results

5.1 Required Exposure Times

The monitor's projected performance was investigated by examining the theoretical exposure time needed to obtain statistically reliable profile information. This was done by combining the results from the power absorption simulations from Sec. 3.2.2 and the system responsivity that was found at the end of the previous section.

Examining the exposure times required to accumulate good statistics was an excellent way to probe the overall performance of the monitor. Exposure times were dependent on the beam flux and energy, the system responsivity and the camera noise. Thus, by determining the length of exposure required to produce a result that was reasonably precise, all of the key portions of the project had to be incorporated. Also, the methods used to produce the gamma-rays at HIGS rely on the periodic injection of electrons from a linac into a storage ring, meaning there is a periodic degradation of the beam flux. This means that the exposure time must be short compared to the injection period for the results to be accurate. Finally, the exposure times are a parameter that could easily be tested once in-beam profiling becomes possible.

To calculate the theoretical times required, consider a gamma-ray beam with a flux of Γ, each with an energy $h\nu$, spread evenly over a beam spot of diameter d. $P_{absorbed}$ can be found using GEANT, for various scintillator and converter types and thicknesses, as in Sec. 3.2.2. The scintillation light is imaged onto the CCD by the optical system with a magnification of M, as measured in Sec. 4.3, generating a circular image of diameter Md. The image would cover a number of bins, J, given by

$$J = K\frac{\pi(\frac{d}{2}M)^2}{A_{CCD}}, \tag{97}$$

where K is the number of bins in the sensor and A_{CCD} is the area of the sensor.

Using J, the responsivity per bin, r_{sys}, dark current per bin, i_{dark}, and noise floor per bin, n_{floor}, can be found in terms of electrons using Eq. 69, Eq. 82 and Eq. 83. Then, the number of electrons accumulated in an illuminated bin, n_I, for an exposure of length t_{INT} would expressed as

$$n_I = r_{sys}P_{absorbed}t_{INT} + i_{dark}t_{INT} + n_{floor}, \tag{98}$$

and the corresponding dark frame would generate n_D electrons given by

$$n_D = i_{dark}t_{INT} + n_{floor}. \tag{99}$$

Subtracting n_D from n_I gives n_p, the number of electrons that were generated as a result of the illumination:

$$n_p = r_{sys}P_{absorbed}t_{INT}. \tag{100}$$

The error in n_p is given by

$$\delta n_p^2 = \delta n_I^2 + \delta n_D^2, \tag{101}$$

where δn_I and δn_D are determined by the noise in the system and are described as

$$\delta n_I^2 = n_p + i_{dark} t_{INT} + n_{floor} + (U_{PRNU} n_p)^2 + (U_{FPN} i_{dark} t_{INT})^2, \tag{102}$$

and

$$\delta n_D^2 = i_{dark} t_{INT} + n_{floor} + (U_{FPN} i_{dark} t_{INT})^2. \tag{103}$$

Substituting the expression for n_p into the above equations, and taking the sum gives

$$\delta n_p^2 = r_{sys} P t_{INT} + 2 i_{dark} t_{INT} + 2 n_{floor} + (U_{PRNU} r_{sys} P t_{INT})^2 + (U_{FPN} i_{dark} t_{INT})^2 \tag{104}$$

for the error in the number of photoelectrons generated. Note that $P_{absorbed}$ has been replaced with P to shorten the length of the equations.

If it is required that the error in the number of photoelectrons, in any given bin, is a fraction, ϵ, of the total number of photoelectrons in that bin, then

$$\epsilon n_p = \delta n_p. \tag{105}$$

Substitution results in

$$\begin{aligned} (\epsilon r_{sys} P t_{INT})^2 = \\ r_{sys} P t_{INT} + 2 i_{dark} t_{INT} + 2 n_{floor} + (U_{PRNU} r_{sys} P t_{INT})^2 + (U_{FPN} i_{dark} t_{INT})^2. \end{aligned} \tag{106}$$

Gathering the like powers of t_{INT} in Eq. 106 generates a quadratic equation,

$$\begin{aligned} ((U_{PRNU} r_{sys} P)^2 + 2(U_{FPN} i_{dark})^2 - (\epsilon r_{sys} P)^2) t_{INT}^2 \\ + (r_{sys} P + 2 i_{dark}) t_{INT} + 2 n_{floor} = 0, \end{aligned} \tag{107}$$

which can be solved for t_{INT}:

$$\begin{aligned} t_{INT} &= \frac{-(r_{sys} P + 2 i_{dark})}{2((U_{PRNU} r_{sys} P)^2 + 2(U_{FPN} i_{dark})^2 - (\epsilon r_{sys} P)^2)} \\ &\pm \frac{\sqrt{(r_{sys} P + 2 i_{dark})^2 - 4((U_{PRNU} r_{sys} P)^2 + 2(U_{FPN} i_{dark})^2 - (\epsilon r_{sys} P)^2) 2 n_{floor}}}{2((U_{PRNU} r_{sys} P)^2 + 2(U_{FPN} i_{dark})^2 - (\epsilon r_{sys} P)^2)}. \end{aligned} \tag{108}$$

From this equation it is seen that t_{INT} depends on the required error, ϵ, the power absorbed by the scintillator, P, the system responsivity per bin, r_{sys}, and the CCD noise parameters, U_{PRNU}, U_{FPN}, i_{dark} and n_{floor}. In turn, P is a function of the scintillator type and thickness, converter type and thickness, beam flux and gamma-ray energy, and r_{sys} varies with the number of bins, J, which is determined by the beam spot size as in Eq. 97.

The quadratic form of Eq. 107 implies that there are certain conditions for which no real solutions exist for t_{INT}, specifically when the portion under the square root is negative. Plotting t_{INT} as a function of the required error, ϵ, for three different $P_{absorbed}$ values shows that there is a minimum achievable error. These plots are shown in Fig. 56, where it is seen that as the error approaches about 1%, the required exposure time goes toward infinity.

The relationship between the exposure time required for a given error value and the beam energy was examined using the GEANT simulation results from Sec. 3.2.2. Using the $P_{absorbed}$ values from Fig. 26, a plot of the projected t_{INT} versus beam energy was made and is shown in Fig. 57. This plot also shows the effect of using different converter materials on the required t_{INT}.

Figures 58 and 59 show the effects of different thickness of scintillators and converters for beam energies of 2, 10 and 100 MeV.

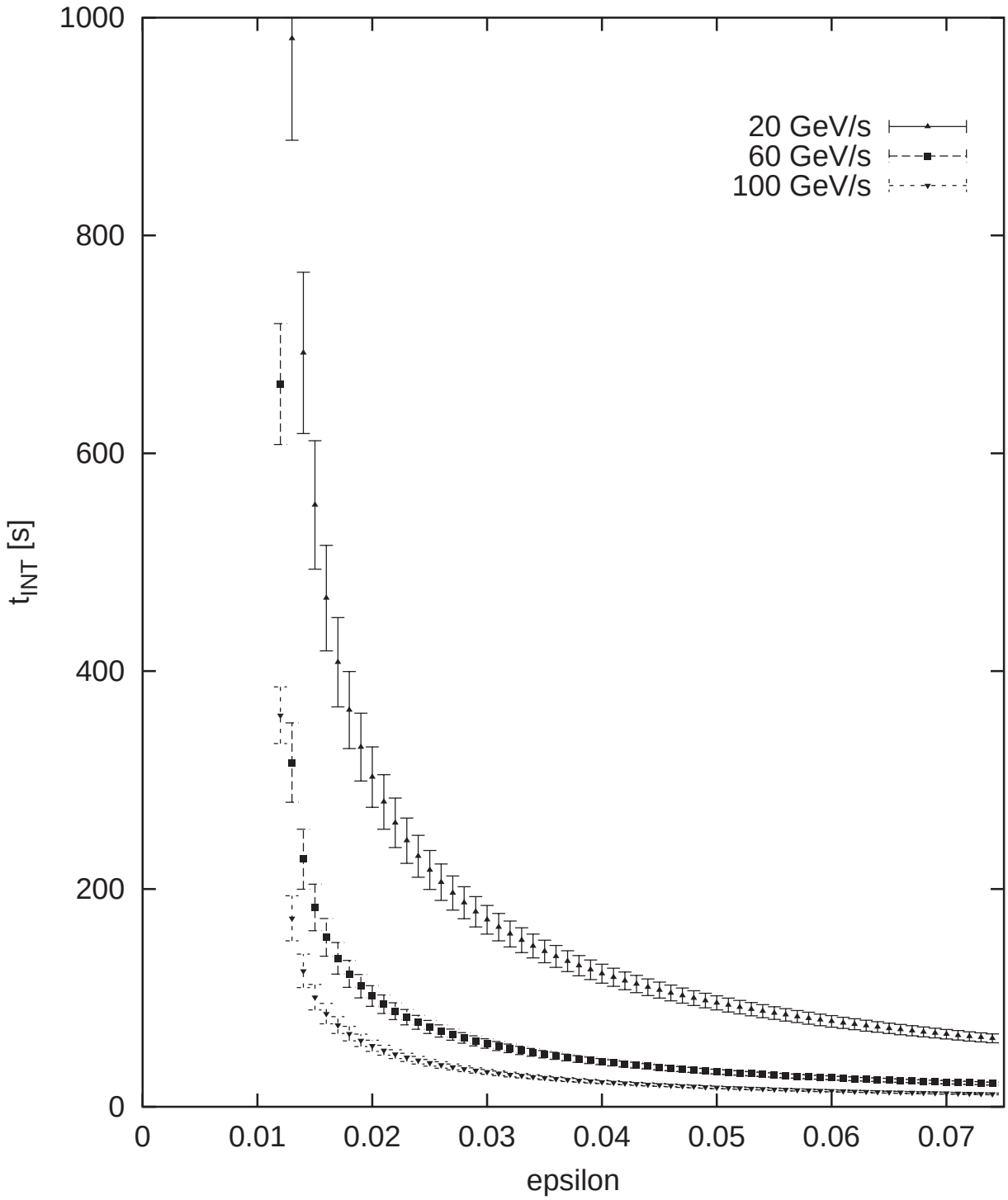

Figure 56: The time required (y axis) to achieve a fraction of error in counts per 4x4 bin (x axis) for $P_{absorbed}$ values of 20, 60 and 100 GeV/s, and a 2.5 cm diameter beam spot.

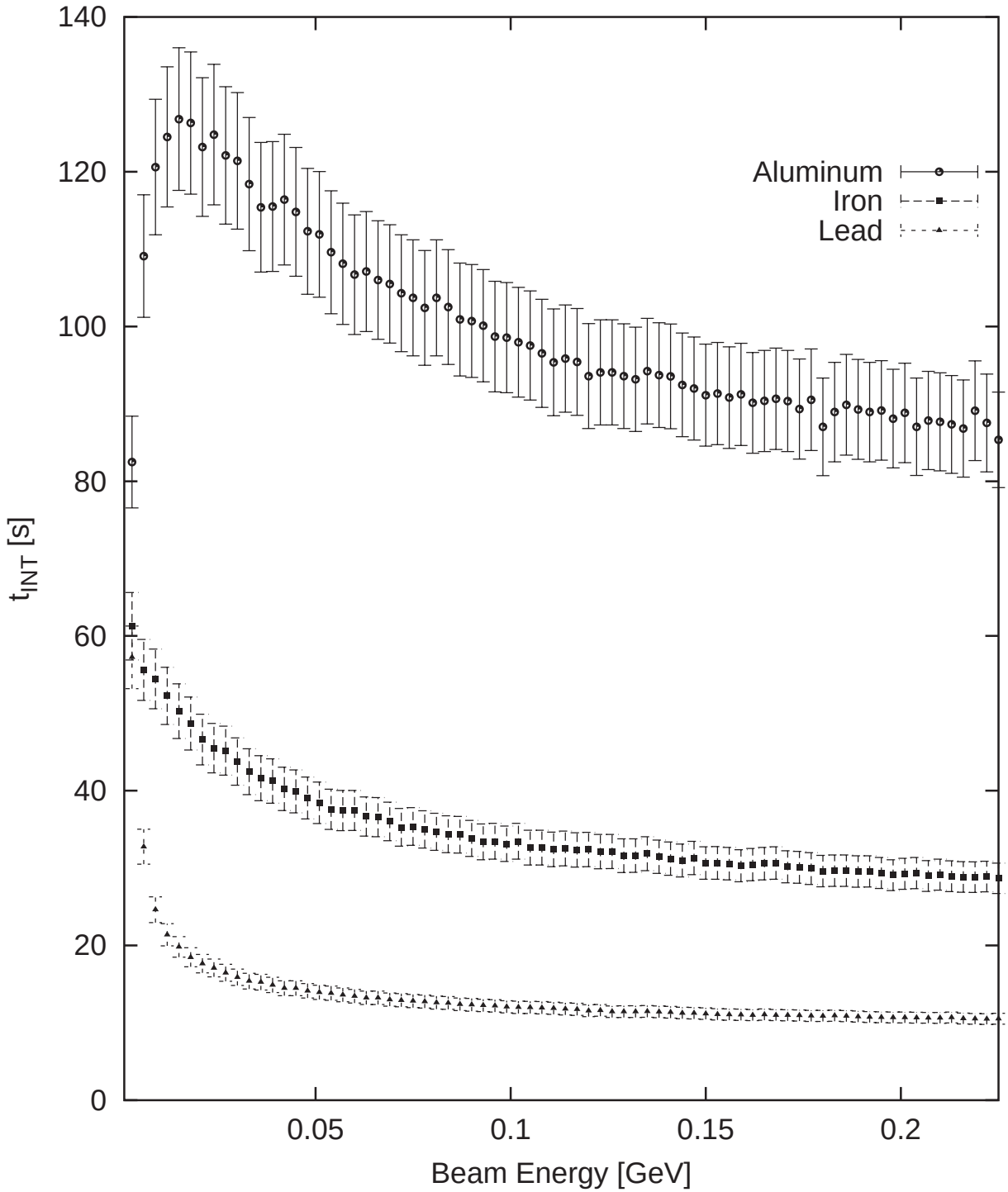

Figure 57: The exposure time versus the beam energy, to achieve a 5% error in counts per 4x4 bin when using 6 mm of plastic scintillator and 0.6 mm thick iron, aluminum and lead converters. The beam flux used was 10^6 γ/s.

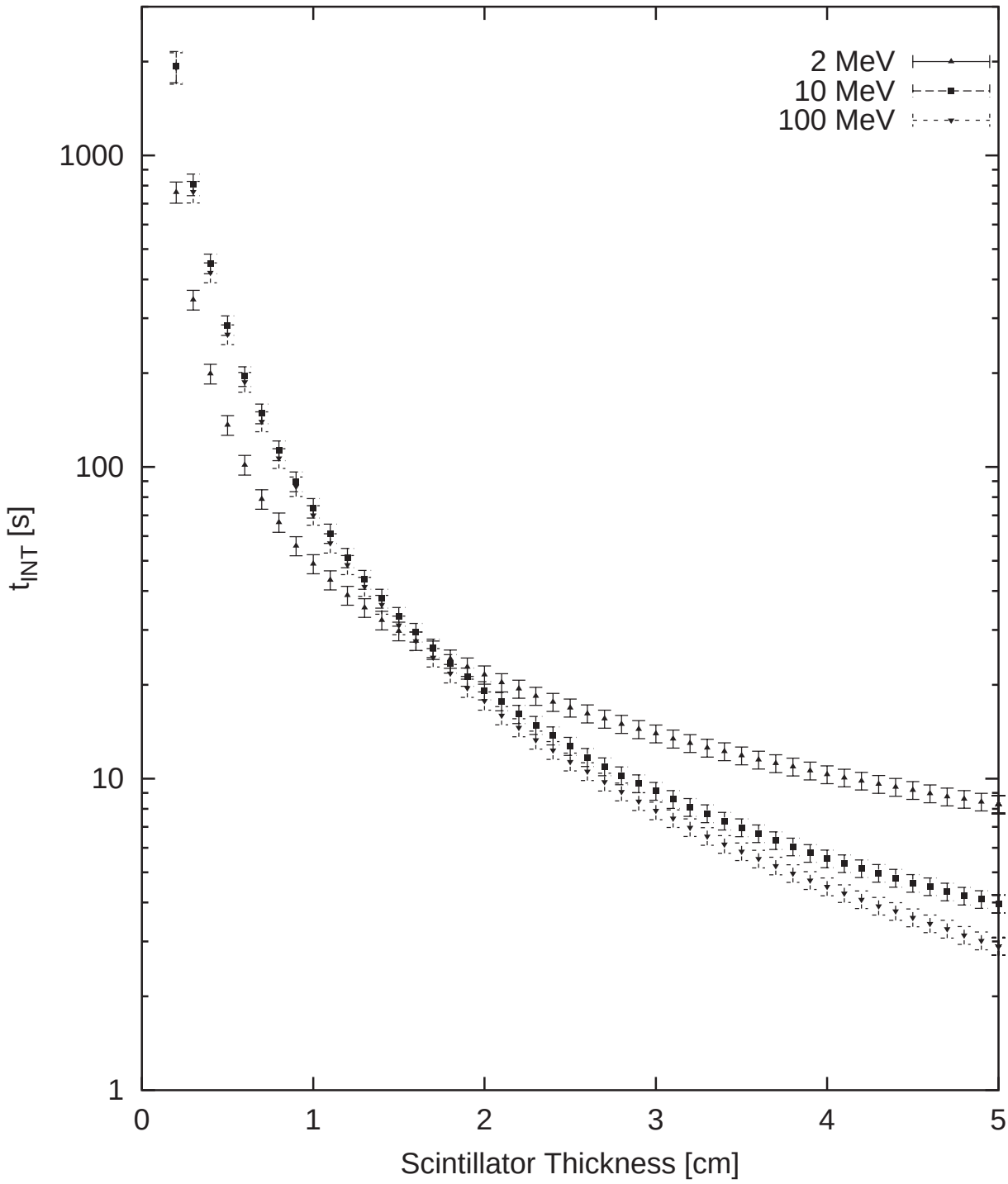

Figure 58: The time required to obtain results with 5% error in counts per 4x4 bin versus the scintillator thickness for beam energies of 2, 10, and 100 MeV for a beam spot 2.5 cm in diameter when no converter is used. The times are shown on a log scale.

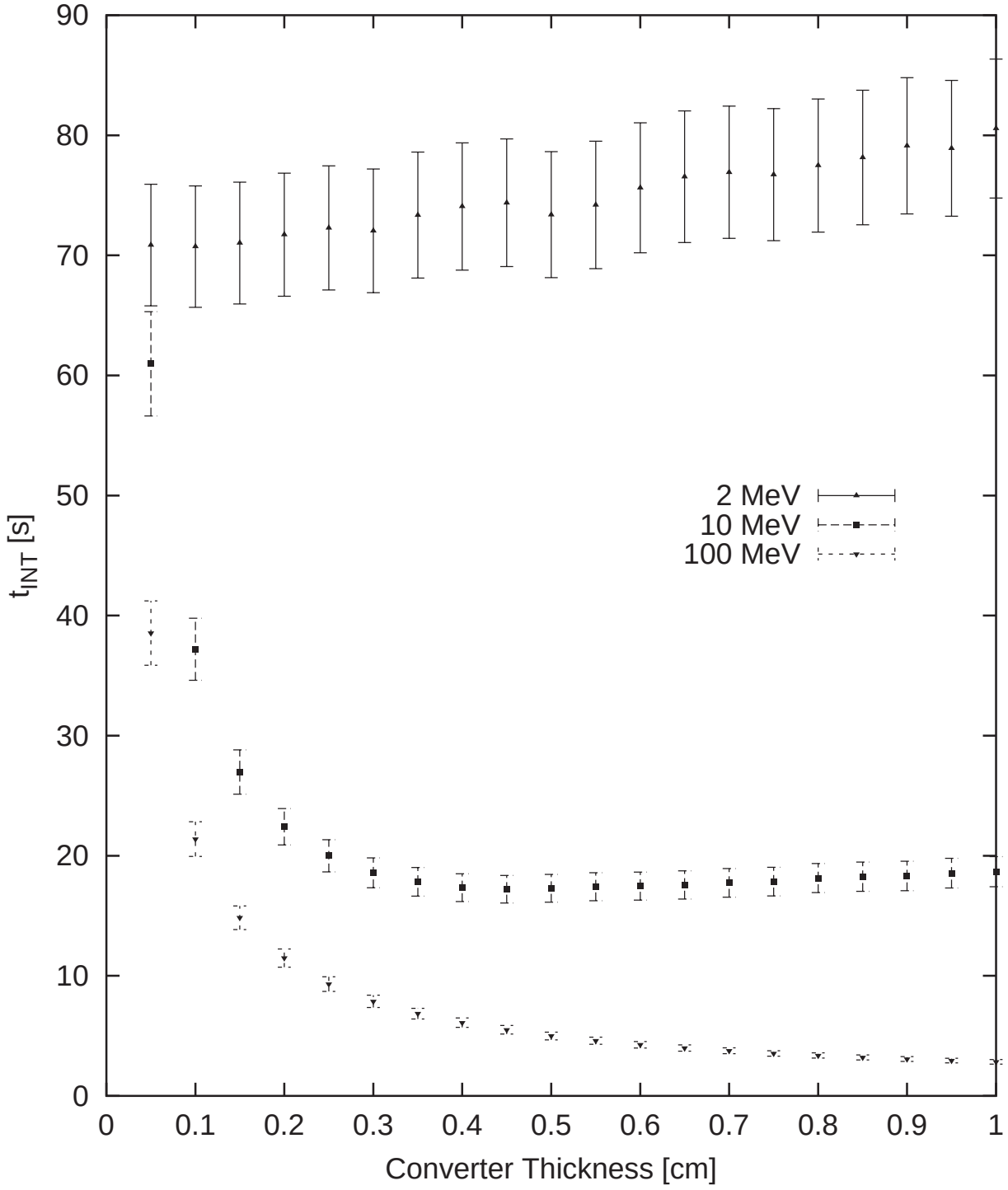

Figure 59: The effects of varying the converter thickness on the time required to obtain results with 5% error in counts per 4x4 bin. The beam flux used was $10^6\gamma/s$ in a 2.5 cm diameter beam spot. Values are shown for a 6 mm thick scintillator.

5.2 Summary and Conclusions

Through the application of the theory behind gamma-ray interactions, scintillation, optics and CCD technology, a gamma-ray beam profiling device was designed, prototyped and tested and was shown to be capable of measuring the profile of a ^{137}Cs source. Using the results of the source measurements, the responsivity of the system was found and used, in conjunction with the CCD noise analysis and GEANT simulations, to project the exposure times required to obtain beam profiles for different acceptable errors.

GEANT simulations were used to predict the energy absorption rates for different configurations of plastic scintillator and converter. The results of these simulations, which are based upon the theoretical photon cross sections for the photoelectric effect, Compton scattering and pair production, provided power absorption values that were used to find the system responsivity and predict the camera response to different beam and detector configurations.

A Meade Pictor 416XT astronomical CCD camera was employed, along with a ^{106}Ru source, to prove that the CCD-based profiling system had merit. Profiles obtained with this camera-source combination provided the verification needed to secure the resources needed to continue project development and a Starlight Express MX-5 CCD was chosen and purchased for use. Development of data acquisition and camera control software that could easily interface with the existing system at HIGS was completed. The remainder of the equipment needed, specifically the optical system and a light tight box, were designed and constructed.

A wide variety of testing was completed on the apparatus to ensure the design constraints could be satisfied. The light tight box was shown to be effective at providing an illumination free environment for profiling to be performed, with the CCD showing only a $3 \times 10^{-3}\%$ change in response to ambient room light when placed in the box. Camera noise characteristics were measured to allow for a calculation of the error component of the camera output. The PRNU was found to be 0.0168 ± 0.0002 and the FPN was 0.00943 ± 0.0005. A dark current of $9.000 \pm 0.004 \frac{e^-}{bin\ s}$ and a noise floor of $79174 \pm 3 \frac{e^-}{bin}$ were measured for 4x4 binning. By exposing the CCD to a constant radiant power, the camera responsivity was measured to be $(3.88 \pm 0.02) \times 10^8 \frac{e^-}{J}$. The camera behaviour over time was also examined and it was found that 100 seconds of 'warm up' time were required before the camera output became steady.

Limited testing on the optical system revealed that due to an angular displacement of the scintillator normal to the optical axis, there was a gradient to the resolution. A vertical resolution of $0.227 \pm 0.002 \frac{mm}{well}$ and a horizontal resolution of $0.177 \pm 0.002 \frac{mm}{well}$ were seen at the center of the image. The magnification of the lens combination used was found to be 0.0756 ± 0.0001.

Testing the beam profiler with a ^{137}Cs gamma-ray source provided a means by which the systems responsivity could be determined and allowed for the prediction of required exposure times. Multiple source profiles were taken over a period of several months, in which time many small, but significant, improvements were made to the apparatus and software was

developed to perform data analysis and presentation. A source count rate measurement and two GEANT simulations, one of the count rate measurement configuration and one of the beam profiling configuration, were used to correlate the number of counts recorded in the central 1 cm radius of the beam profile to the amount of power deposited in the corresponding region of the scintillator.

The system responsivity was calculated to be 126 ± 8 counts per GeV of energy absorbed by the scintillator for 4x4 binning. This value was found using a simulation-measurement analysis which used the measured count rate to determine the required source simulation intensity. Essentially, this method involved simulating the source count rate measurement and finding the required number of simulated gamma-rays to reproduce the measured rate, then using this value in a simulation of the profiling configuration, to generate the power absorption in the scintillator. In 5% of the solid angle of 4π steradians, $(3.4 \pm 0.2) \times 10^8$ gamma-rays per second needed to be simulated to reproduce the count rate measurement. This flux density resulted in a power absorption of 6.97 ± 0.46 GeV/s in a region of the scintillator that generated 787392 counts in the camera in a 900 second exposure. Using these values the aforementioned responsivity was calculated.

Exposure times, as a function of the required error, were found by equating the required error to the noise in the system and solving for the necessary exposure time. The noise in the system is responsible for producing an error in the number of electrons accumulated in each bin. This noise is comprised of the shot noise, noise floor and pattern noise, added in quadrature. By determining how long an exposure has to be so that this noise component only represents a specified fraction of the total number of photoelectrons, the performance capabilities of the camera were identified in terms of the required duration of exposure. A typical exposure time, found for the case where a 6 mm scintillator, coupled to a 0.6 mm iron converter is placed in a 6 MeV gamma-ray beam with a flux of $10^6\gamma$/s and a beam spot diameter of 2.5 cm, was 55 ± 4 seconds, which was considered acceptable.

The cumulative results of this project amounted to a set of plots that indicated the exposure times required to obtain a given error, in the number of counts per bin, for different configurations of scintillators, converters and gamma-ray energies. These plots are given, in part, to facilitate the in-beam testing of the monitor. Through the use of the relationships displayed in the results section, suitable apparatus and beam configurations can be selected for testing and the effect of changing any one of the parameters can be predicted. These plots also show that the projected performance capabilities of a CCD-based beam profiler satisfy the design requirements and the system should be tested at HIGS.

5.3 Recommended Enhancements

The results of this project indicated that precise and accurate beam profiles are obtainable given a certain length of exposure. That length was a function of several variables related to the scintillator characteristics, optical system and CCD specifications. This section outlines some of the key areas where future development would be the most effective at reducing the required exposure times. Some recommendations regarding the resolution of the system are also presented.

5.3.1 Alternative Scintillators

BC 400 was chosen as the scintillator for this project because it was readily available and easy to work with. There are, however, other scintillators that could be used to increase the power absorption of the system and thus reduce required exposure times.

In Sec. 2.2, the benefits of using an inorganic scintillator, due to its higher atomic number and thus higher photon cross section, were discussed. BGO is a non-hygroscopic crystal with a density of $7.3\frac{g}{cm^3}$ that emits scintillation with a spectral output peaked at 480 nm. The atomic number of bismuth is 83, which, along with its high density, gives BGO a high photon cross section, but its light output is only one third the light output of plastic [Leo94].

To quantify the performance enhancements resulting from the use of BGO, a plot of the time required to achieve 5% error using it is shown in Fig. 60.[7] The figure shows that using BGO dramatically reduces the required exposure times!

The primary drawbacks to using BGO are the costs associated with obtaining a crystal large enough to cover the entire beam spot and the additional beam degradation caused by the higher cross section. A crystal of suitable size would cost around $750. However, due to the dramatic decrease in exposure times BGO would be a better choice for the scintillator in the beam profile monitor.

5.3.2 Optical System

The optical system provides the means by which the photons of visible wavelength are transported to the CCD from the scintillator. From Eq. 63 it is seen that the power reaching the CCD is determined from the power absorbed, the scintillation efficiency and two parameters of the optical system; the effective pupil diameter and the distance from the scintillator to the lens system. Therefore, the system responsivity is also dependent on these optical system parameters.

The design process used to construct the optical system used in this project did not involve optimization of the effective pupil diameter and the scintillator lens separation. Rather, a suitable system, based on four available lenses, was constructed. Future development should

[7] To calculate t_{INT} for BGO, the measured system responsivity from Sec. 4.4.4 was multiplied by the relative light output of BGO with respect to plastic scintillator: 1/3.

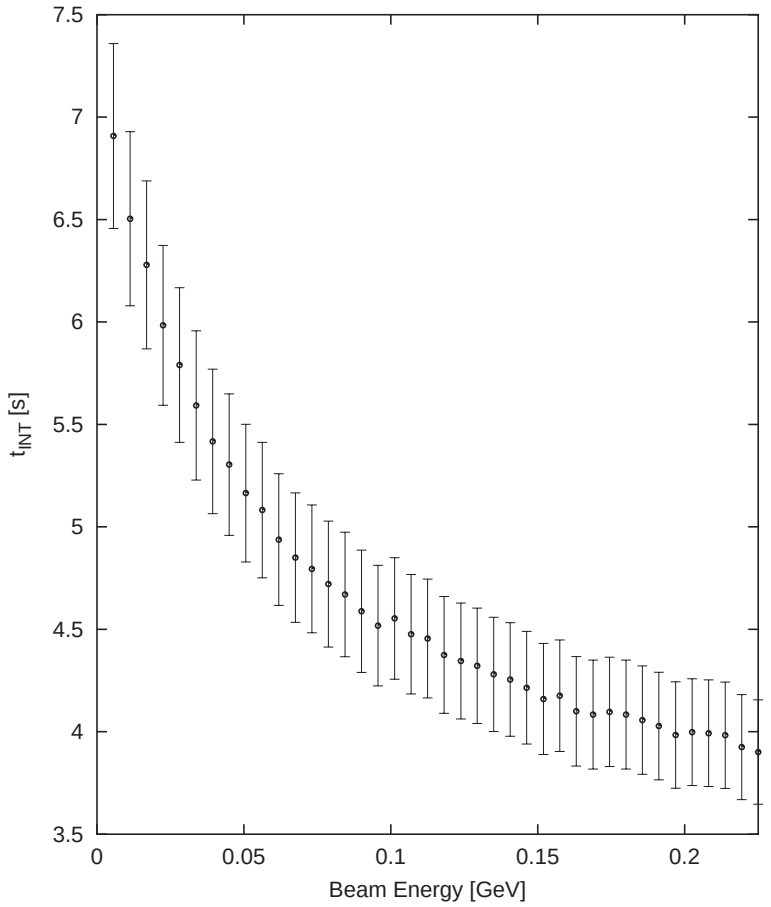

Figure 60: A plot of the time required to obtain results with 5% error versus the beam energy for a beam spot 2.5 cm in diameter, containing 10^6 γ/s, using 2 mm thick BGO.

involve a less constrained approach to the lens system design, allowing for the introduction of more refractive surfaces. Also, the use of anti-reflective coatings on all lens surfaces would improve the light transfer efficiency of the optical system and serve to further increase the responsivity of the system.

5.3.3 CCD

The Starlight Express MX5 CCD camera was a good choice for this project. It had a low dark current and noise floor, and was able to acquire images of sufficient resolution and could be interfaced to the Linux-based data acquisition system with relative ease. However, one can not ignore the potential benefits that could arise with the use of a scientific class CCD camera or an intensified CCD.

The main difference between the MX5 and the scientific class of cameras was the size of the sensor. Table 2 shows the number of pixels and the size of each pixel for each of the different CCDs. The three scientific CCDs have fairly large sensors giving them the better responsivities and the higher price tags. And, despite the increase in sensor area, they still

maintain fairly low dark currents.

An intensified CCD could also be used to dramatically increase responsivity. An intensified CCD consists of a regular CCD with microchannel plate (MCP) connected. Attaching a MCP is like attaching a photomultiplier tube to each pixel on the CCD. In a MCP tiny cylinders, each coated with a photosensitive material, are placed in a strong electric field. A photon entering one of the cylinders creates an avalanche of electrons which are then accumulated in a CCD pixel. Although a very efficient device, they are extremely expensive.

Because of the high costs associated with even slight improvements in CCD quality, upgrading the CCD should not be performed unless there is no other option. Given the results of this project, there would likely be no reason to replace the MX5 unless more stringent design requirements are proposed.

5.3.4 Resolution

Additional work needs to be done to investigate the resolution of the system. The resolutions referred to in Sec. 4.3 only take into consideration the optical system and the CCD camera resolutions. They did not account for dispersion of the incident gamma-ray energy which would negatively impact the resolution.

To equate the spacial resolution of the system to the resolution measured from the optical test pattern would not be prudent. The effects of electromagnetic showers and multiple scattering in the converter and scintillator would first have to be analyzed. Only by confirming that the degradation of the resolution due to these effects is small in comparison to the optical and CCD resolution could one make any conclusions regarding the system resolution.

References

[Ahm02] M.W. Ahmed. A multi-wire cathode-strip readout (mwpc-csr) system to monitor the profile of the higs gamma-ray beam. *Triangle Universities Nuclear Laboratory Progress Report - XLI*, 134, 2002.

[Bic00] Inc Bicron, Saint Gobain Industrial Ceramics. http://www.bicron.com, 2000.

[Bir64] J. B. Birks. *The Theory and Practice of Scintillation Counting*. The Macmillan Company, 1964.

[Bro64] W. Brouwer. *Matrix Methods in Optical Instrument Design*. W. A. Benjamin, Inc., 1964.

[Car94] T. Scott Caraman. *Production of Gamma-Rays for Nuclear Physics Using the Duke Free-Electron-Laser Facility*. Triangle Universities Nuclear Laboratory, 1994.

[Cen03] High Energy Astrophysical Science Archive Research Center. *Ftools: A General Package of Software to Manipulate FITS Files*. http://heasarc.gsfc.nasa.gov/docs/software/ftools, 2003.

[CER03] CERN. http://public.web.cern.ch/public/index.html, 2003.

[Cor01] Hamamatsu Corporation. *Hamamatsu Product Information*. Hamamatsu Corporation, http://usa.hamamatsu.com, 2001.

[Cor03] Optenso Corporation. *Optical Engineering Software*. http://www.optenso.de, 2003.

[Fac97] NASA/GSFC Astrophysics Data Facility. *A User's Guide for the Flexible Image Transport System (FITS)*, 1997.

[Fir99] R. B. Firestone. *A Guide to the Table of Isotopes*. Wiley, 1999.

[Gro00] D. E. Groom. *European Physical Journal*, C15, 2000.

[Hag02] K. Hagiwara. *Physical Review D*, **66**(010001), 2002.

[Hol98] Gerald C. Holst. *CCD Arrays, Cameras and Displays*. JCD Publishing and SPIE Optical Engineering Press, 1998.

[Kle70] Les V. Klein. *Optics*. John Wiley and Sons, Inc., 1970.

[Kno00] Glenn F. Knoll. *Radiation Detection and Measurement, 3rd Ed.* John Wiley and Sons, Inc., 2000.

[Leo94] W. R. Leo. *Techniques for Nuclear and Particle Physics Experiments*. Springer-Verlag, 1994.

[mea03] Meade Instruments Corporation, www.meade.com, 2003.

[Sch03] David Schmenk. *Linux CCD Astronomical Imaging.* http://home.earthlink.net/~dschmenk/, 2003.

[var03] VariCAD Ltd., www.varicad.com, 2003.

[Wis01] Jeff Wishart. *Transition Radiation Monitors at the Canadian Light Source.* MSc. Thesis, Department of Physics and Engineering Physics, University of Saskatchewan, 2001.

A Dose Rate from ^{137}Cs Source

A calculation of the rate at which radiation, given off by the ^{137}Cs source (see Sec. 4.4), was absorbed by living tissue was performed to ensure personnel safety.

The source activity, measured in 1972, was 50 mCi. Using the radioactive decay law, $N(t) = N(0)exp(-\lambda t)$, the activity in 2003 was found:

$$\begin{aligned} N(31yrs) &= 50\ mCi\ exp(-\frac{ln\ 2}{30.2yrs}31yrs) \\ &= 24.5\ mCi. \end{aligned} \tag{A.1}$$

Note that $1Ci$ is equal to 3.7×10^{10} disintegrations per second. The exposure rate, $D_{exposure}$, was found from this activity through

$$D_{exposure} = \frac{\Gamma\ N(31yrs)}{d^2}, \tag{A.2}$$

where d is the distance to the source and Γ is the exposure rate constant measured in units of $\frac{R\ cm^2}{hr\ mCi}$. Here, R, represents Roentgens, or the quantity of x-rays required to produce an ionization of 1 esu/cm^3 in air at standard temperature and pressure. For a ^{137}Cs source the exposure rate constant is $3.3\frac{R\ cm^2}{hr\ mCi}$ [Leo94]. Assuming the distance to the source was kept larger than arms length, or around 75 cm, the maximum exposure rate was

$$D_{exposure} = \frac{3.3R - cm^2/hr - mCi\ 24.5mCi}{75cm^2} = 14.4mR/hr. \tag{A.3}$$

The absorbed dose was calculated from the exposure rate by assuming that living tissue absorbs around 9.3 mGy (note 1 Gy = 1 Joule/kg) for 1 R of γ radiation [Leo94]:

$$D_{dose} = 9.3\frac{mGy}{R}\ 14.4 \times 10^{-3}\frac{R}{hr} = 0.134\frac{mGy}{hr}. \tag{A.4}$$

Because the radiation weighting factor for gamma-rays is 1, the equivalent dose is equal to the absorbed dose, but given in units of Sieverts (Sv) per hour:

$$D_{equivalent} = 0.134\frac{mSv}{hr}. \tag{A.5}$$

The International Commission on Radiological Protection recommends a maximum of 50 mSv per year for individuals exposed through their occupation. To reach this level of exposure would require 373 hours of close proximity to the source.

An estimate of the amount of time spent near the source in the duration of the testing phase of this project was 20 hours. Care was taken to place as much shielding as possible around the source and at all times the source remained within its lead container. Therefore, it is likely that the absorbed dose was insignificant in comparison to the yearly maximum allowable level of 50 mSv.

B Error Analysis

B.1 Simulation Errors

The size of the error bars on the $P_{absorbed}$ values, obtained using GEANT, were calculated within the simulation. Each $P_{absorbed}$ value was found by summing the energy weighted columns in the energy deposition histogram and dividing by the one second time interval:

$$P_{absorbed} = \frac{1}{s}\sum_{i=1}^{N} E_i C_i. \tag{B.1}$$

Here, N is the number of columns in the power deposition histogram, E_i is the energy represented by the ith column and C_i is the number of counts in column i. The error is then given by

$$\delta P_{absorbed} = \frac{1}{s}\left(\sum_{i=1}^{N}(\sigma_E)^2\left(\frac{\partial}{\partial E}P_{absorbed}\right)^2 + \sum_{i=1}^{N}(\sigma_{C_i})^2\left(\frac{\partial}{\partial C}P_{absorbed}\right)^2\right)^{\frac{1}{2}}, \tag{B.2}$$

where σ_E is just the histogram bin width, ΔE, and σ_{C_i} is square root of the number of counts in column i. Substitution of these variables leads to

$$\delta P_{absorbed} = \frac{1}{s}\left(\sum_{i=1}^{N}\Delta E^2 C_i^2 + \sum_{i=1}^{N} C_i E_i^2\right)^{\frac{1}{2}}. \tag{B.3}$$

If there are a sufficient number of bins in the histogram ΔE becomes very small and the first sum can be neglected, leaving

$$\delta P_{absorbed} = \frac{1}{s}\left(\sum_{i=1}^{N} C_i E_i^2\right)^{\frac{1}{2}}. \tag{B.4}$$

B.2 System Responsivity Error, δR_{SYS}

The calculation of R_{SYS} relies on gamma-ray flux information from Eq. 89. A flux, Γ, of 3.4×10^8/s was found using the following values:

$$\begin{gathered}\text{Measured Count Rate} : (8.7 \pm 0.6) \times 10^4/\text{s},\\ \text{Simulated Counts} : (5.19 \pm 0.07) \times 10^5/\text{s},\\ \text{Simulated Gamma} - \text{Rays} : 10^8,\\ \text{Fraction of } 4\pi\text{steradians} : 0.05.\end{gathered}$$

The error in Γ was then found to be

$$\begin{aligned}\delta\Gamma &= 10^8\sqrt{\left(\frac{0.6\times10^4/s}{5.19\times10^5}\frac{1}{0.05}\right)^2 + \left(\frac{8.7\times10^4/s}{(5.19\times10^5)^2}\frac{0.07\times10^5}{0.05}\right)^2}\\ &= 0.2\times10^8/s.\end{aligned} \tag{B.5}$$

This error has to be propagated into the error in the value obtained for $P_{absorbed}$.

A value of 6.97 GeV/s for $P_{absorbed}$ was obtained from a GEANT simulation, so it contains a simulation error component of 0.05 GeV/s, as described in Sec. B.1. Additional error, caused by the uncertainty in Γ, can be found by looking at the ratio of the flux error to the flux. $P_{absorbed}$ values are linearly related to the number of gamma-rays generated in the simulation, so the error introduced by $\delta\Gamma$ is

$$\begin{aligned} \delta P_{absorbed} &= \frac{\delta\Gamma}{\Gamma} P_{absorbed} \\ &= \frac{0.2 \times 10^8}{3.4 \times 10^8} 6.97\ GeV/s = 0.41\ GeV/s. \end{aligned} \tag{B.6}$$

$\delta P_{absorbed}$ was the sum of the two errors:

$$\delta P_{absorbed} = 0.05\ GeV/s + 0.41\ GeV/s = 0.46\ GeV/s. \tag{B.7}$$

The error in R_{SYS} was also dependent on the error in the number of counts, δN_C. N_C was found in Eq. 26 to be the number of counts in the central region of the source image minus the number of counts in the central region of the dark image. Therefore, the error in N_C is

$$\delta N_C = \sqrt{\delta N_{Source}^2 + \delta N_{Dark}^2}, \tag{B.8}$$

where δN_{Source} and δN_{Dark} are determined by the noise in the system.

In Sec. 2.3.4, the noise in any one 4x4 bin, n_i, in units of electrons, was determined to be

$$n_i = \sqrt{n_{shot}^2 + n_{floor}^2 + n_{pattern}^2}, \tag{B.9}$$

where n_{shot}, n_{floor} and $n_{pattern}$ are as defined in Eq. 35, Eq. 43 and Eq. 47, and the subscript i indicates the ith bin. Values for the shot noise and pattern noise were easily obtained using the measured values of the dark current and the PRNU. The noise due to the uncertainty in the noise floor, however, could not be calculated as described in the theory because the specifics of the circuitry used, particularly the amplifier gains and associated capacitances, were not known. Instead, an approximation, based on the noise floor measurement made in Sec. 4.2.2, was used. The noise floor was measured to be 2.4323×10^7 counts over 9000 bins. Converting this to electrons per bin gave 7.91×10^4. Approximating the noise in this quantity by its square root gave a n_{floor} of 281 e^- per 4x4 bin.

n_i was calculated for each bin in the center region of the image and the error in the total number of electrons accumulated, δn, was found using

$$\delta n = \sqrt{\sum_i^J n_i^2}. \tag{B.10}$$

The error was then converted back to units of counts giving

$$\delta N_{Source} = 1239,$$

and

$$\delta N_{Dark} = 861,$$

which add in quadrature to give the error in the number of counts in the background subtracted image:

$$\delta N_C = \sqrt{1239^2 + 861^2} = 1509. \tag{B.11}$$

The errors in $P_{absorbed}$ and N_C propagate through to δR_{SYS} giving

$$\delta R_{SYS} = \sqrt{\left(\frac{\delta N_C}{P_{absorbed}\, t_{INT}}\right)^2 + \left(\frac{N_C\, \delta P_{absorbed}}{P_{absorbed}^2\, t_{INT}}\right)^2}. \tag{B.12}$$

Substituting the appropriate values yields the error in the system responsivity:

$$\delta R_{SYS} = \sqrt{\left(\frac{1509}{6.97\ GeV/s\ 900\ s}\right)^2 + \left(\frac{787392\ 0.46\ GeV/s}{(6.97\ GeV/s)^2\ 900\ s}\right)^2} = 8 \text{ Counts/GeV}. \tag{B.13}$$

B.3 Required Time Error, δt_{INT}

Calculating the error in t_{INT} required performing an error propagation analysis on Eq. 108. δt_{INT}^2 is given by

$$\begin{aligned}\delta t_{INT}^2 = &\left(\frac{\partial t_{INT}}{\partial r_{sys}}\delta r_{sys}\right)^2 + \left(\frac{\partial t_{INT}}{\partial P_{absorbed}}\delta P_{absorbed}\right)^2 + \left(\frac{\partial t_{INT}}{\partial i_{dark}}\delta i_{dark}\right)^2 + \\ &\left(\frac{\partial t_{INT}}{\partial U_{PRNU}}\delta U_{PRNU}\right)^2 + \left(\frac{\partial t_{INT}}{\partial U_{FPN}}\delta U_{FPN}\right)^2 + \left(\frac{\partial t_{INT}}{\partial n_{floor}}\delta n_{floor}\right)^2.\end{aligned} \tag{B.14}$$

This equation was used to determine the size of the error bars in Fig. 56, 57, 58, 59 and 60.

C CCD Specifications

Starlight Express MX5 camera specification:

- CCD type: Sony ICX055BL SuperHAD CCD with ultra low dark current and vertical anti-blooming.
- CCD pixel data: Pixel size: 9.8 x 6.3 μm^2, Image format: 500 x 582 pixels.
- CCD size: Imaging area: 4.9 mm (horizontal) x 3.6 mm (vertical).
- Spectral response: Peak response at 520nm (green), 50% at 400nm (violet) and 670nm (near infra-red).
- Readout noise: Approx. 15 electrons RMS.
- Full-well capacity: Approx. 120,000 e-.
- Dark current: Dark frame saturation time greater than 150 hours. Less than 0.1 electrons/ pixel/ second.
- Computer interface: 8 bit unidirectional parallel port with bi-directional status lines (Standard Centronics interface). 25 pin 'D' style plug for LPT1, 2 or 3, via a 5 metre x 6mm diameter cable.
- Image download time: Typically 20 seconds with a 66 MHz 486 PC, 8 seconds when using a port accelerator module.
- Power requirements: 115VAC / 240VAC @ 12VA, or 12VDC @ 700 milliamps max.
- Cooling system: Regulated constant-current cooling supply built-in. Single-stage thermoelectric cooler to give a CCD temperature of approximately -30C below ambient.
- Size: 50 x 100mm black anodized aluminum barrel with M42 thread at CCD window end and 15 way 'D' style input plug at rear. Versions with a 'CS' thread adapter for TV camera lenses are also available.
- Weight: 200g.

The following pages are taken from the Sony ICX055BL manual and are provided as a convenient reference.

SONY

ICX055BL

Diagonal 6mm (Type 1/3) CCD Image Sensor for CCIR B/W Video Cameras

Description

The ICX055BL is an interline CCD solid-state image sensor suitable for CCIR B/W video cameras. Compared with the current product ICX055AL, sensitivity is improved drastically through the adoption of Super HAD CCD technology.

This chip features a field period readout system, and an electronic shutter with variable charge-storage time.

16 pin DIP (Plastic)

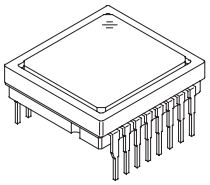

Features

- High sensitivity (+4dB at F8, +2dB at F1.2 compared with ICX055AL)
- High saturation signal (+1dB compared with ICX055AL)
- Low smear and low dark current
- Excellent antiblooming characteristics
- Continuous variable-speed shutter
- Horizontal register: 5V drive
- Reset gate: 5V drive

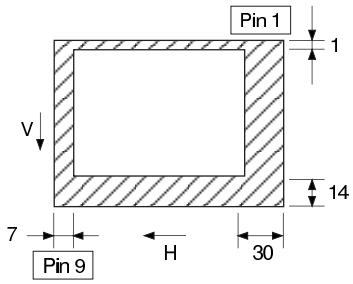

Optical black position
(Top View)

Device Structure

- Interline CCD image sensor
- Image size: Diagonal 6mm(Type 1/3)
- Number of effective pixels: 500 (H) × 582 (V) approx. 290K pixels
- Number of total pixels: 537 (H) × 597 (V) approx. 320K pixels
- Chip size: 6.00mm (H) × 4.96mm (V)
- Unit cell size: 9.8µm (H) × 6.3µm (V)
- Optical black: Horizontal (H) direction: Front 7 pixels, Rear 30 pixels
  Vertical (V) direction: Front 14 pixels, Rear 1 pixel
- Number of dummy bits: Horizontal 16
  Vertical 1 (even field only)
- Substrate material: Silicon

Super **HAD CCD** ®

*Super HAD CCD is a registered trademark of Sony Corporation. Super HAD CCD is a CCD that drastically improves sensitivity by introducing newly developed semiconductor technology by Sony Corporation into Sony's high-performance HAD (Hole-Accumulation Diode) sensor.

E98225A99

Block Diagram and Pin Configuration

(Top View)

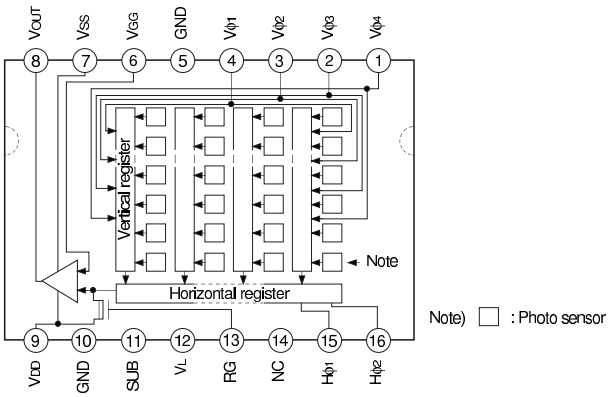

Pin Description

Pin No.	Symbol	Description	Pin No.	Symbol	Description
1	$V\phi_4$	Vertical register transfer clock	9	V_{DD}	Output amplifier drain supply
2	$V\phi_3$	Vertical register transfer clock	10	GND	GND
3	$V\phi_2$	Vertical register transfer clock	11	SUB	Substrate (Overflow drain)
4	$V\phi_1$	Vertical register transfer clock	12	V_L	Protective transistor bias
5	GND	GND	13	RG	Reset gate clock
6	V_{GG}	Output amplifier gate bias	14	NC	
7	V_{SS}	Output amplifier source	15	$H\phi_1$	Horizontal register transfer clock
8	V_{OUT}	Signal output	16	$H\phi_2$	Horizontal register transfer clock

Absolute Maximum Ratings

Item		Ratings	Unit	Remarks
Substrate voltage SUB – GND		–0.3 to +55	V	
Supply voltage	V_{DD}, V_{OUT}, V_{SS} – GND	–0.3 to +18	V	
	V_{DD}, V_{OUT}, V_{SS} – SUB	–55 to +10	V	
Vertical clock input voltage	$V\phi_1$, $V\phi_2$, $V\phi_3$, $V\phi_4$ – GND	–15 to +20	V	
	$V\phi_1$, $V\phi_2$, $V\phi_3$, $V\phi_4$ – SUB	to +10	V	
Voltage difference between vertical clock input pins		to +15	V	*1
Voltage difference between horizontal clock input pins		to +17	V	
$H\phi_1$, $H\phi_2$ – $V\phi_4$		–17 to +17	V	
$H\phi_1$, $H\phi_2$, RG, V_{GG} – GND		–10 to +15	V	
$H\phi_1$, $H\phi_2$, RG, V_{GG} – SUB		–55 to +10	V	
V_L – SUB		–65 to +0.3	V	
$V\phi_1$, $V\phi_2$, $V\phi_3$, $V\phi_4$, V_{DD}, V_{OUT} – V_L		–0.3 to +30	V	
RG – V_L		–0.3 to +24	V	
V_{GG}, Vss, $H\phi_1$, $H\phi_2$ – V_L		–0.3 to +20	V	
Storage temperature		–30 to +80	°C	
Operating temperature		–10 to +60	°C	

*1 +27V (Max.) when clock width<10µs, clock duty factor<0.1%.

Bias Conditions

Item	Symbol	Min.	Typ.	Max.	Unit	Remarks
Output amplifier drain voltage	V_{DD}	14.55	15.0	15.45	V	
Output amplifier gate voltage	V_{GG}	1.75	2.0	2.25	V	
Output amplifier source	V_{SS}	Grounded with 680Ω resistor				±5%
Substrate voltage adjustment range	V_{SUB}	9.0		18.5	V	*1
Fluctuation range after substrate voltage adjustment	ΔV_{SUB}	–3		+3	%	
Reset gate clock voltage adjustment range	V_{RGL}	1.0		4.0	V	*1
Fluctuation range after reset gate clock voltage adjustment	ΔV_{RGL}	–3		+3	%	
Protective transistor bias	V_L	*2				

DC Characteristics

Item	Symbol	Min.	Typ.	Max.	Unit	Remarks
Output amplifier drain current	I_{DD}		3		mA	
Input current	I_{IN1}			1	μA	*3
Input current	I_{IN2}			10	μA	*4

*1 Indications of substrate voltage (V_{SUB}) · reset gate clock voltage (V_{RGL}) setting value.
The setting values of substrate voltage and reset gate clock voltage are indicated on the back of the image sensor by a special code. Adjust substrate voltage (V_{SUB}) and reset gate clock voltage (V_{RGL}) to the indicated voltage. Fluctuation range after adjustment is ±3%.

V_{SUB} code one character indication □ □
V_{RGL} code one character indication ↑ ↑
V_{RGL} code V_{SUB} code

Code and optimal setting correspond to each other as follows.

V_{RGL} code	1	2	3	4	5	6	7
Optimal setting	1.0	1.5	2.0	2.5	3.0	3.5	4.0

V_{SUB} code	E	f	G	h	J	K	L	m	N	P	Q	R	S	T	U	V	W	X	Y	Z
Optimal setting	9.0	9.5	10.0	10.5	11.0	11.5	12.0	12.5	13.0	13.5	14.0	14.5	15.0	15.5	16.0	16.5	17.0	17.5	18.0	18.5

<Example> "5L" → V_{RGL} = 3.0V
V_{SUB} = 12.0V

*2 V_L setting is the V_{VL} voltage of the vertical transfer clock waveform.

*3 1) Current to each pin when 18V is applied to V_{DD}, V_{OUT}, Vss and SUB pins, while pins that are not tested are grounded.
2) Current to each pin when 20V is applied sequentially to $V\phi_1$, $V\phi_2$, $V\phi_3$ and $V\phi_4$ pins, while pins that are not tested are grounded. However, 20V is applied to SUB pin.
3) Current to each pin when 15V is applied sequentially to RG, $H\phi_1$, $H\phi_2$ and V_{GG} pins, while pins that are not tested are grounded. However, 15V is applied to SUB pin.
4) Current to V_L pin when 30V is applied to $V\phi_1$, $V\phi_2$, $V\phi_3$, $V\phi_4$, V_{DD} and V_{OUT} pins or when, 24V is applied to RG pin or when, 20V is applied to V_{GG}, Vss, $H\phi_1$ and $H\phi_2$ pins, while V_L pin is grounded. However, GND and SUB pins are left open.

*4 Current to SUB pin when 55V is applied to SUB pin, while pins that are not tested are grounded.

Clock Voltage Conditions

Item	Symbol	Min.	Typ.	Max.	Unit	Waveform diagram	Remarks
Readout clock voltage	V_{VT}	14.55	15.0	15.45	V	1	
Vertical transfer clock voltage	V_{VH1}, V_{VH2}	–0.05	0	0.05	V	2	$V_{VH} = (V_{VH1} + V_{VH2})/2$
	V_{VH3}, V_{VH4}	–0.2	0	0.05	V	2	
	V_{VL1}, V_{VL2}, V_{VL3}, V_{VL4}	–9.0	–8.5	–8.0	V	2	$V_{VL} = (V_{VL3} + V_{VL4})/2$
	$V_{\phi V}$	7.8	8.5	9.05	V	2	$V_{\phi V} = V_{VHn} - V_{VLn}$ (n = 1 to 4)
	$\lvert V_{VH1} - V_{VH2} \rvert$			0.1	V	2	
	$V_{VH3} - V_{VH}$	–0.25		0.1	V	2	
	$V_{VH4} - V_{VH}$	–0.25		0.1	V	2	
	V_{VHH}			0.5	V	2	High-level coupling
	V_{VHL}			0.5	V	2	High-level coupling
	V_{VLH}			0.5	V	2	Low-level coupling
	V_{VLL}			0.5	V	2	Low-level coupling
Horizontal transfer clock voltage	$V_{\phi H}$	4.75	5.0	5.25	V	3	
	V_{HL}	–0.05	0	0.05	V	3	
Reset gate clock voltage	$V_{\phi RG}$	4.5	5.0	5.5	V	4	*1
	$V_{RGLH} - V_{RGLL}$			0.8	V	4	Low-level coupling
Substrate clock voltage	$V_{\phi SUB}$	22.5	23.5	24.5	V	5	

*1 The reset gate clock voltage need not be adjusted when reset gate clock is driven when the specifications are as given below. In this case, the reset gate clock voltage setting indicated on the back of the image sensor has not significance.

Item	Symbol	Min.	Typ.	Max.	Unit	Waveform diagram	Remarks
Reset gate clock voltage	V_{RGL}	–0.2	0	0.2	V	4	
	$V_{\phi RG}$	8.5	9.0	9.5	V	4	

Clock Equivalent Circuit Constant

Item	Symbol	Min.	Typ.	Max.	Unit	Remarks
Capacitance between vertical transfer clock and GND	$C\phi V1$, $C\phi V3$		1500		pF	
	$C\phi V2$, $C\phi V4$		820		pF	
Capacitance between vertical transfer clocks	$C\phi V12$, $C\phi V34$		470		pF	
	$C\phi V23$, $C\phi V41$		230		pF	
	$C\phi V13$		150		pF	
	$C\phi V24$		230		pF	
Capacitance between horizontal transfer clock and GND	$C\phi H1$, $C\phi H2$		47		pF	
Capacitance between horizontal transfer clocks	$C\phi HH$		47		pF	
Capacitance between reset gate clock and GND	$C\phi RG$		5		pF	
Capacitance between substrate clock and GND	$C\phi SUB$		320		pF	
Vertical transfer clock series resistor	R_1, R_3		51		Ω	
	R_2, R_4		100		Ω	
Vertical transfer clock ground resistor	R_{GND}		15		Ω	
Horizontal transfer clock series resistor	$R\phi H$		10		Ω	
Reset gate clock series resistor	$R\phi RG$		40		Ω	

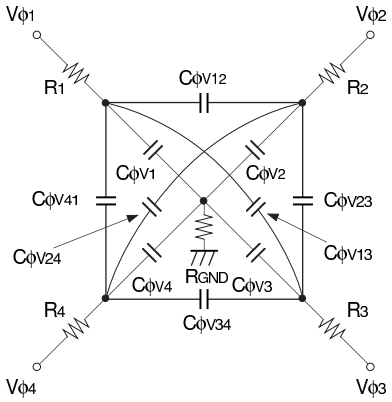

Vertical transfer clock equivalent circuit

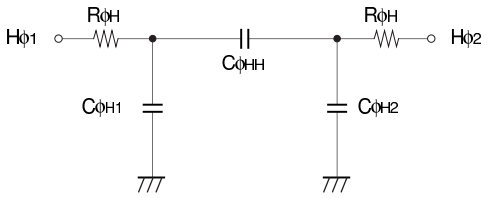

Horizontal transfer clock equivalent circuit

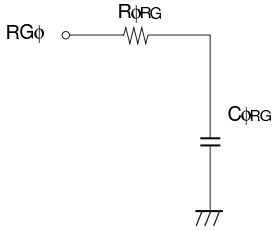

Reset gate clock equivalent circuit

Image Sensor Characteristics (Ta = 25℃)

Item	Symbol	Min.	Typ.	Max.	Unit	Measurement method	Remarks
Sensitivity	S	700	840		mV	1	
Saturation signal	Vsat	720			mV	2	Ta = 60℃
Smear	Sm		0.002	0.007	%	3	
Video signal shading	SH			20	%	4	Zone 0, I
				25	%	4	Zone 0 to II'
Dark signal	Vdt			2	mV	5	Ta = 60℃
Dark signal shading	ΔVdt			1	mV	6	Ta = 60℃
Flicker	F			2	%	7	
Lag	Lag			0.5	%	8	

Zone Definition of Video Signal Shading

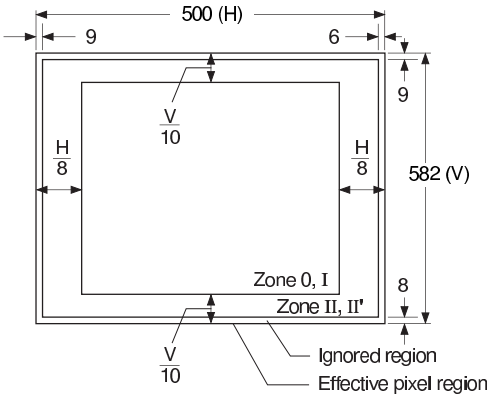

Image Sensor Characteristics Measurement Method

◎ Measurement conditions

1) In the following measurements, the substrate voltage and the reset gate clock voltage are set to the values indicated on the device, and the device drive conditions are at the typical values of the bias and clock voltage conditions.

2) In the following measurements, spot blemishes are excluded and, unless otherwise specified, the optical black (OB) level is used as the reference for the signal output, and the value measured at point [*A] in the drive circuit example is used.

◎ Definition of standard imaging conditions

1) Standard imaging condition I:
Use a pattern box (luminance 706cd/m^2, color temperature of 3200K halogen source) as a subject. (Pattern for evaluation is not applicable.) Use a testing standard lens with CM500S (t = 1.0mm) as an IR cut filter and image at F8. The luminous intensity to the sensor receiving surface at this point is defined as the standard sensitivity testing luminous intensity.

2) Standard imaging condition II:
Image a light source (color temperature of 3200K) with a uniformity of brightness within 2% at all angles. Use a testing standard lens with CM500S (t = 1.0mm) as an IR cut filter. The luminous intensity is adjusted to the value indicated in each testing item by the lens diaphragm.

1. Sensitivity
Set to standard imaging condition I. After selecting the electronic shutter mode with a shutter speed of 1/250s, measure the signal output (Vs) at the center of the screen and substitute the value into the following formula.

$$S = Vs \times \frac{250}{50} \text{ [mV]}$$

2. Saturation signal
Set to standard imaging condition II. After adjusting the luminous intensity to 10 times the intensity with average value of the signal output, 200mV, measure the minimum value of the signal output.

3. Smear
Set to standard imaging condition II. With the lens diaphragm at F5.6 to F8, adjust the luminous intensity to 500 times the intensity with average value of the signal output, 200mV. When the readout clock is stopped and the charge drain is executed by the electronic shutter at the respective H blankings, measure the maximum value VSm [mV] of the signal output and substitute the value into the following formula.

$$Sm = \frac{VSm}{200} \times \frac{1}{500} \times \frac{1}{10} \times 100 \text{ [\%] (1/10V method conversion value)}$$

4. Video signal shading
Set to standard imaging condition II. With the lens diaphragm at F5.6 to F8, adjust the luminous intensity so that the average value of the signal output is 200mV. Then measure the maximum (Vmax [mV]) and minimum (Vmin [mV]) values of the signal output and substitute the values into the following formula.

$$SH = (Vmax - Vmin)/200 \times 100 \text{ [\%]}$$

5. Dark signal
Measure the average value of the signal output (Vdt [mV]) with the device ambient temperature 60°C and the device in the light-obstructed state, using the horizontal idle transfer level as a reference.

6. Dark signal shading
After measuring 5, measure the maximum (Vdmax [mV]) and minimum (Vdmin [mV]) values of the dark signal output and substitute the values into the following formula.

$\Delta Vdt = Vdmax - Vdmin$ [mV]

7. Flicker
Set to standard imaging condition II. Adjust the luminous intensity so that the average value of the signal output is 200mV, and then measure the difference in the signal level between fields (ΔVf [mV]). Then substitute the value into the following formula.

$F = (\Delta Vf/200) \times 100$ [%]

8. Lag
Adjust the signal output value generated by strobe light to 200mV. After setting the strobe light so that it strobes with the following timing, measure the residual signal (Vlag). Substitute the value into the following formula.

$Lag = (Vlag/200) \times 100$ [%]

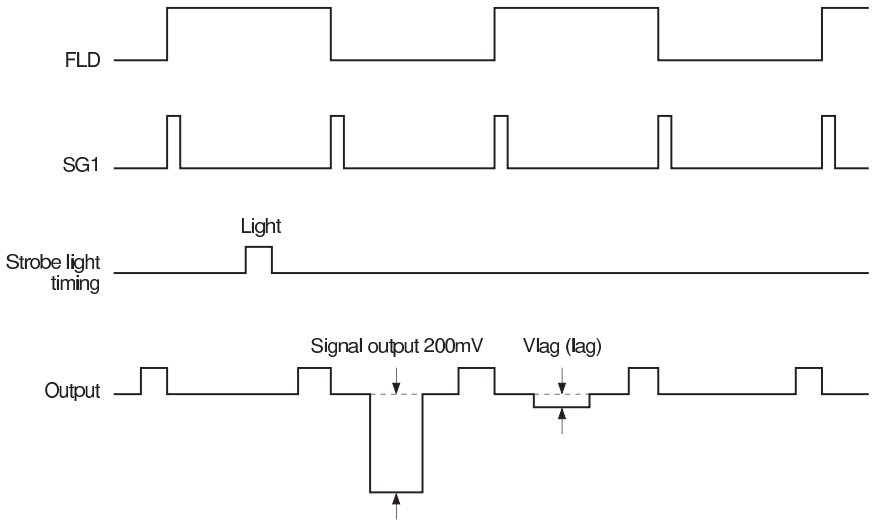

Drive Circuit

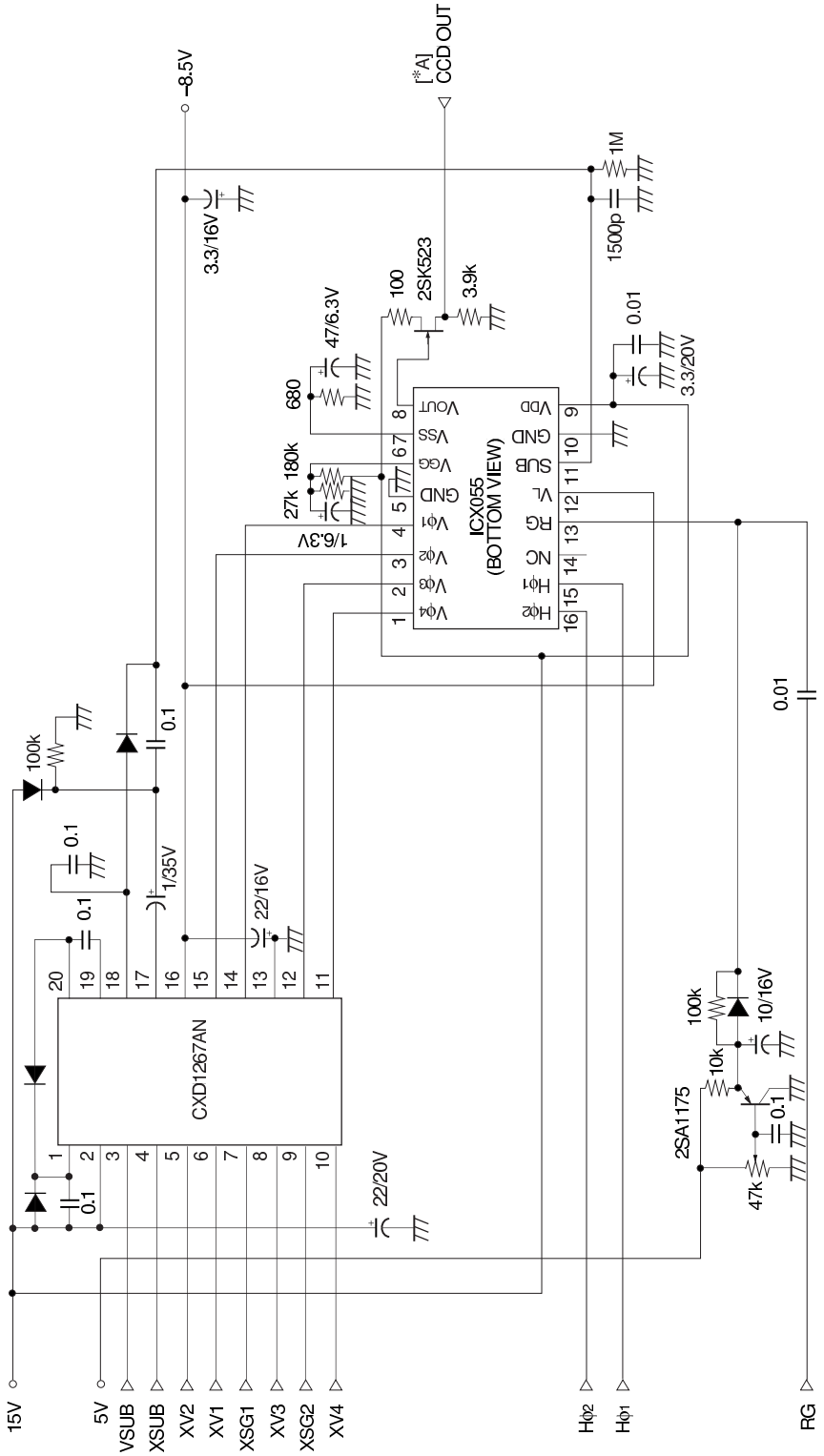

Spectral Sensitivity Characteristics

(Includes lens characteristics, excludes light source characteristics)

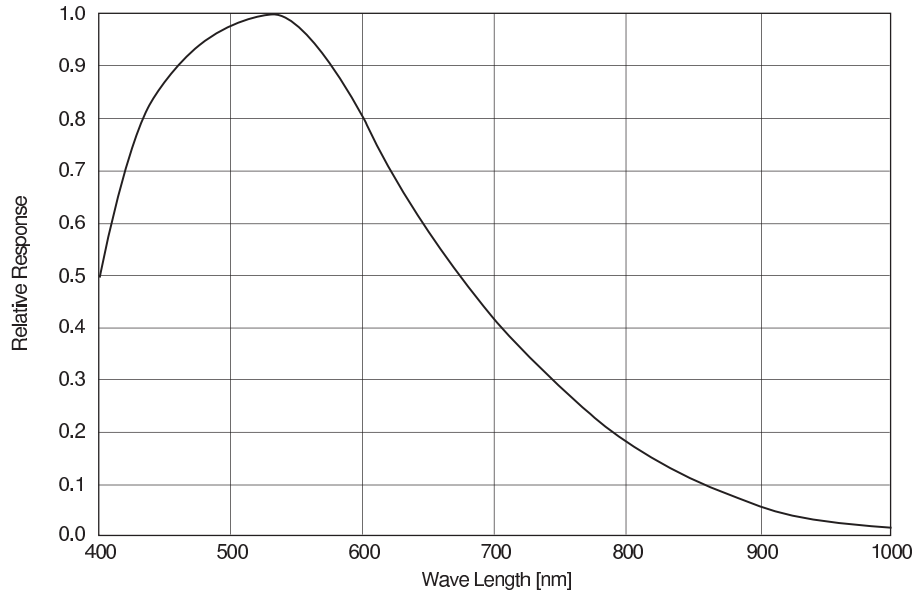

Sensor Readout Clock Timing Chart

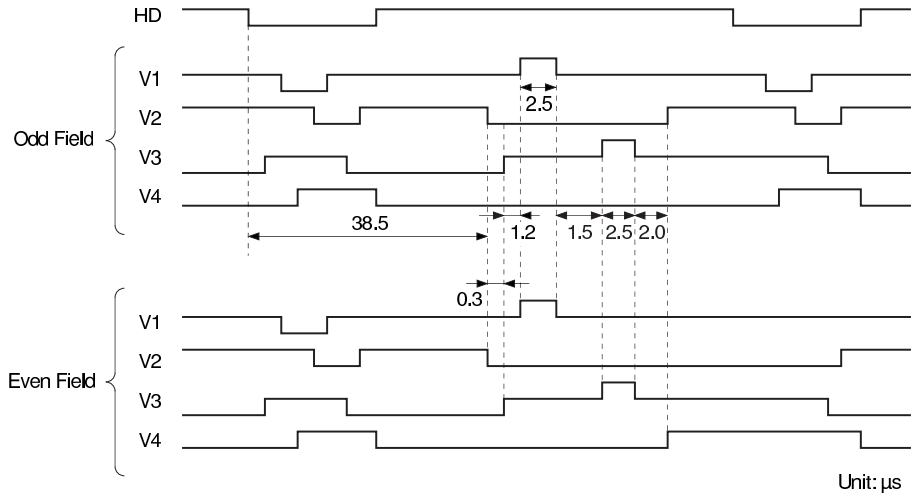

Package Outline Unit: mm

16pin DIP (450mil)

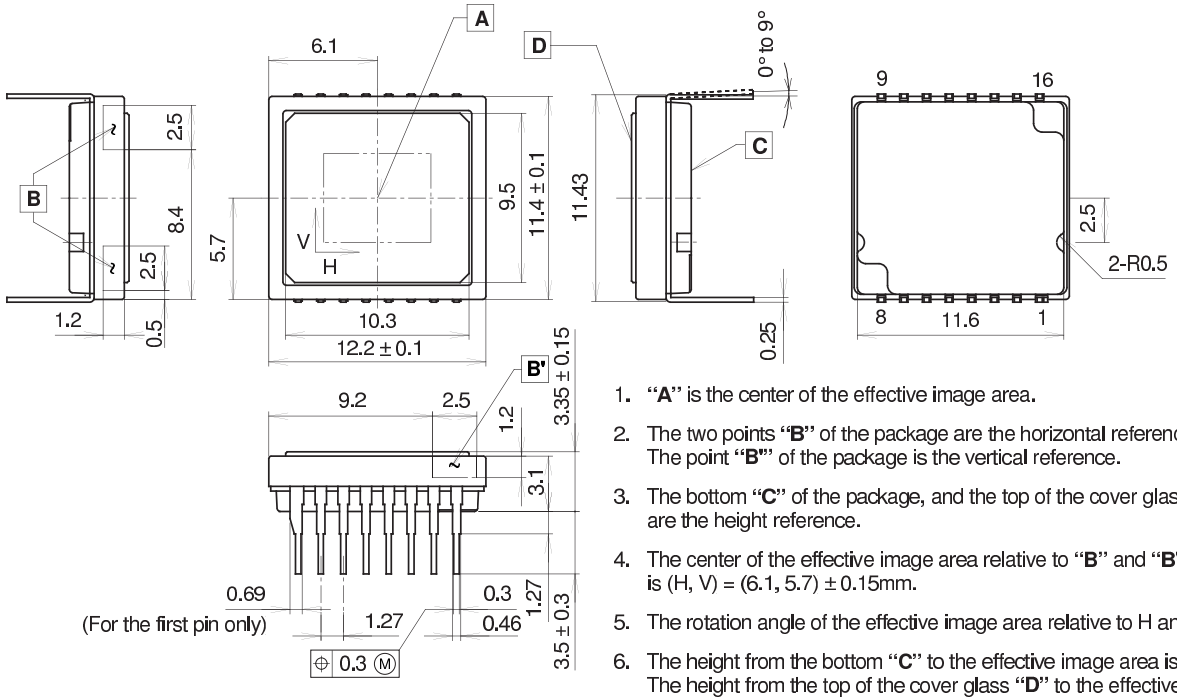

1. "**A**" is the center of the effective image area.
2. The two points "**B**" of the package are the horizontal reference. The point "**B'**" of the package is the vertical reference.
3. The bottom "**C**" of the package, and the top of the cover glass "**D**" are the height reference.
4. The center of the effective image area relative to "**B**" and "**B'**" is (H, V) = (6.1, 5.7) ± 0.15mm.
5. The rotation angle of the effective image area relative to H and V is ± 1°.
6. The height from the bottom "**C**" to the effective image area is 1.41 ± 0.10mm. The height from the top of the cover glass "**D**" to the effective image area is 1.94 ± 0.15mm.
7. The tilt of the effective image area relative to the bottom "**C**" is less than 50µm. The tilt of the effective image area relative to the top "**D**" of the cover glass is less than 50µm.
8. The thickness of the cover glass is 0.75mm, and the refractive index is 1.5.
9. The notches on the bottom of the package are used only for directional index, they must not be used for reference of fixing.

PACKAGE STRUCTURE

PACKAGE MATERIAL	Plastic
LEAD TREATMENT	GOLD PLATING
LEAD MATERIAL	42 ALLOY
PACKAGE WEIGHT	0.9g